Imaging measurements of soot particle size and soot volume fraction with laser-induced incandescence at Diesel engine conditions

Von der Fakultät für Ingenieurwissenschaften, Abteilung Maschinenbau und Verfahrenstechnik der Universität Duisburg-Essen
zur Erlangung des akademischen Grades

eines

Doktors der Ingenieurwissenschaften

Dr.-Ing.

genehmigte Dissertation

von

Emre Cenker

aus

Istanbul

Gutachter: Prof. Dr. Christof Schulz
Prof. Dr.-Ing. Stefan Will
Prof. Dr. Pascale Desgroux

Tag der mündlichen Prüfung: 13/10/2014

ÉCOLE CENTRALE DES ARTS ET MANUFACTURES « ÉCOLE CENTRALE PARIS »

THÈSE

présentée par

Emre Cenker

pour l'obtention du

GRADE DE DOCTEUR

Spécialité:	**Énergétique**
Laboratoire d'accueil:	**Le laboratoire d'Énergétique Moléculaire et Macroscopique, Combustion, (EM2C)**

SUJET:

Imaging measurements of soot particle size and soot volume fraction with laser-induced incandescence at Diesel engine conditions

soutenue le 13 Octobre 2014 devant un jury composé de :

Christof Schulz	**Professeur, University of Duisburg-Essen**	**Directeur de thèse**
Gilles Bruneaux	**Expert, IFPEN**	**Directeur de thèse**
Stefan Will	**Professeur, University of Erlangen-Nürnberg**	**Examinateur**
Pascale Desgroux	**Professeur, Université Lille1**	**Examinateur**
Christine Rousselle	**Professeur, Université d'Orléans**	**Examinateur**
Burak Atakan	**Professeur, University of Duisburg-Essen**	**Examinateur**

This thesis is submitted in fulfilment of the requirements for the degrees Doctor of Philosophy (École Centrale Paris) and Dr.-Ing. (University of Duisburg-Essen) in a joint dissertation program between University of Duisburg-Essen and École Centrale Paris.

Abstract

This work focuses on measurements of soot particle size and volume fraction at Diesel engine conditions. A combination of laser-induced incandescence (LII) imaging, line-of-sight laser extinction, soot pyrometry, and transmission electron microscopy (TEM) measurements of thermophoretically-sampled soot was used. Particle sizing strategies were developed with LII model for the analysis of particle-size poly-dispersity with time-resolved LII signal that is suitable for point-wise measurements at atmospheric pressure, and for spatially-resolved characterization with two-time-step LII imaging. Measurements were performed with these strategies in a flame at atmospheric pressure and in Diesel engine combustion to investigate their applicability. Additional measurements were performed for temperature and soot volume fraction.

A novel method, called two-exponential reverse fitting (TERF), is introduced to extract information about the size distribution. The method is based on mono-exponential fits to the LII signal decay at a delayed time. It approximates the particle-size distribution as a combination of one large and one small mono-disperse equivalent mean particle size and does not require a distribution assumption. It also provides a ratio of the contribution of both size classes. The systematic error caused by describing LII signals by mono-exponential decays was calculated as less than 2% for LII signals simulated for mono-disperse aggregated soot with heat-up temperatures for which evaporation is negligible. The method was applied to LII data acquired in a laminar non-premixed ethylene/air flame at various heights above the burner. The particle size of the large particle-size class evaluated with the method showed good consistency with TEM results, however the size of the small particle-size class and its relative contribution could not be compared due to insufficient information in the TEM results for small particles.

Simultaneous line-of-sight laser extinction measurements and LII imaging were performed to derive the soot volume fraction in a high-temperature high-pressure constant-volume pre-combustion vessel under the Engine Combustion Network's (ECN) "Spray A" conditions with parametric variations of gas temperature and composition. Extinction measurements were used to calibrate LII images for quantitative soot distribution measurements. OH-chemiluminescence imaging was used to determine the lift-off length, and used to interpret the soot measurements. Maximum soot volume fractions around 2–3 ppm were obtained at the nominal ambient temperature defined for Spray A (i.e. 900 K) that rise to 12 ppm at elevated temperature (1030 K). Variations of ambient temperature and oxygen concentration were carried out showing effects on soot formation and oxidation that are consistent with the literature.

The method for particle-size imaging is based on evaluating gated LII signals acquired with two cameras consecutively after the laser pulse and using LII modeling to deduce particle size from the ratio of local signals. A strategy was developed with a model-based analysis: the dependence of LII particle-size imaging on the assumed boundary conditions was identified such as bathgas temperature, pressure, particle heat-up temperature, thermal accommodation coefficients, and soot morphology. Various laser-fluence regimes and gas pressures were considered. Effects of laser attenuation were evaluated. A combination of one detection gate starting with the particle-heating and the other starting with 11 ns delay with twice as long gate width was found to provide the highest sensitivity for particle sizing at 60 bar. The optimum gate delays for different pressures were calculated. The effects of timing jitter for laser pulse and poly-dispersity were investigated. Systematic errors in pyrometry imaging at 60 bar was evaluated. Parallel to the model-based analysis, experiments were conducted in near Spray A conditions with parametric variations of injection pressure, gas temperature and composition. The results were compared to particle-size measurements from TEM of soot sampled at multiple axial distances from the injector. The discrepancies between the two measurement techniques are discussed to analyze uncertainties and related error sources of the two diagnostics methodologies. It is found that in such an environment where particles are small and pressure is high, LII signal decay times are such that LII suffers from a strong bias towards large particles.

Zusammenfasung

Diese Arbeit beschäftigt sich mit abbildenden laseroptischen Verfahren zur Messungen von Rußpartikelgröße und -volumenbruch bei dieselmotorischen Bedingungen. Eine Kombination von bildgebender laserinduzierter Inkandeszenz (LII), Laserextinktion und Zweifarben-Pyrometrie wird für in-situ Messungen eingesetzt. Vergleichend wird die Partikelgröße in thermophoretisch abgeschiedenem Ruß mit Transmissionselektronenmikroskopie (TEM) bestimmt. Der Messstrategie liegt ein LII-Modell zugrunde, das die zeitliche Variation des LII-Signals in Punktmessungen bzw. das Signalverhältnis bei abbildender Detektion mit zwei Zeitschritten nutzt. Messungen wurden in einer Flamme bei Atmosphärendruck und in einer Hochdruck-Einpritzkammer unter dieselmotorischen Bedingungen durchgeführt. Hierzu wurde ein neues Verfahren, das two-exponential reverse fitting (TERF) genannt wird, entwickelt und angewendet. Das Verfahren basiert auf einer monoexponentiellen Anpassungen des LII-Signalabfalls in einer gegenüber dem Laserpuls verzögerten Zeitspanne. Das Verfahren liefert Information zur Partikelgrößenverteilung als eine Kombination aus einer großen und einer kleinen monodispersen äquivalente Teilgröße ohne eine a-priori Annahme einer Größenverteilung zu erfordern. Ein Verhältnis des Beitrags der beiden Größenklassen wird ermittelt. Der systematische Fehler, der durch die monoexponenzielle Anpassung des LII-Signalverlaufs hervorgerufen wird, liegt bei weniger als 2% für monodisperse Ruß-Aggregate in einem Temperaturbereich, in dem Verdampfung vernachlässigt werden kann. Das Verfahren ist auf LII-Daten gestützt, die in einer nicht-vorgemischten Ethylen/Luft-Flamme, in verschiedenen Höhen über einem Brenner ermittelt wurden. Die ermittelte Partikelgröße der großen Partikelfraktion zeigt eine gute Übereinstimmung mit den TEM-Ergebnissen, allerdings kann die Größe der kleinen Partikelfraktion und ihr relativer Beitrag aufgrund unzureichender Informationen in den TEM-Ergebnisse für kleine Partikel nicht verglichen werden.

Laserextinktions-Messungen und LII-Bildgebung wurden gleichzeitig durchgeführt, um den Partikel-Volumenbruch in einer Hochdruckzelle unter den vom Engine Combustion Network (ECN) definierten "Spray A"-Bedingungen zu bestimmen. Absorptions-Messungen wurden verwendet, um die LII-Messungen zu kalibrieren. Bildgebende Messungen der OH-Chemilumineszenz wurden eingesetzt, um die Lift-off-Länge der Diesel-Sprayflamme zu bestimmen. Eine maximale Partikel-Volumenkonzentration von 2–3 ppm wurde bei der Nenn-Umgebungstemperatur für Spray A (900 K) gefunden. Bei erhöhter Temperatur (1030 K) wurden Werte bis 12 ppm beobachtet.

Das Verfahren zur bildgebenden Partikelgrößenmessung basiert auf der Auswertung von LII-Signalen, die mithilfe von zwei Kameras nach dem Laserpuls innerhalb bestimmter Zeitfenster detektiert werden. Das Verfahren wurde mit dem LII-Modell optimiert: Die Abhängigkeit von den angenommenen Randbedingungen (Gastemperatur, Druck, Aufheiztemperatur, Energie-Akkomodationskoeffizienten, Ruß-Morphologie, Laserabschwächung) wurde untersucht. Die optimale Kombination von Detektionsfenstern wurde für Anwendung bei 60 bar ermittelt.

Experimente im Dieselspray wurden mit parametrischen Variationen von Einspritzdruck, Gastemperatur und Gemischzusammensetzung durchgeführt. Die LII-Ergebnisse wurden mit TEM-Messungen verglichen. Die Diskrepanzen zwischen beiden Messtechniken werden diskutiert. Es wurde festgestellt, dass in einer Umgebung, in der Partikel klein sind und der Druck hoch ist, die sehr kurzen LII-Signalabfallzeiten dazu führen, dass große Partikel überbewertet werden.

Résumé

Le travail présenté dans ce manuscrit concerne les mesures de taille de particule et de fraction volumique de suies dans des conditions moteur Diesel. Les techniques utilisées sont la laser-induced incandescence (LII), la méthode d'extinction laser (LEM), la pyrométrie, et l'analyse d'images de microscopie électronique par transmission (TEM) d'échantillons prélevés in-situ. Des stratégies de mesure de tailles de particules sont développées en se basant sur l'utilisation d'un modèle LII et en analysant la poly-dispersion des tailles de particules, aussi bien à partir de signaux de LII résolu en temps (mesures ponctuelles) à pression atmosphérique, que d'informations résolues spatialement provenant d'images acquises a deux instants différents. Des mesures sont effectuées avec ces stratégies sur une flamme à pression atmosphérique et dans des conditions représentatives des conditions moteur Diesel pour évaluer leur applicabilité. Des mesures supplémentaires de température et de fraction volumique de suies sont aussi réalisés.

Une nouvelle méthode, appelée two-exponential reverse fitting (TERF) est introduite. Elle vise à extraire des informations sur la distribution de tailles de particules. Cette méthode est basée sur l'utilisation de fits mono-exponentiel du signal de décroissance de LII à différents intervalles de temps. La distribution de tailles de particules est approximée par la combinaison de deux distributions de tailles de particules mono-disperses: une petite et une large. Aucune hypothèse sur la forme de la distribution n'est nécessaire. La méthode permet aussi de fournir le ratio de la proportion respective des deux classes de particules. L'erreur systématique induite par la description mono-exponentielle de la décroissance du signal de LII a été calculée et est inférieure à 2% pour des décroissances de signal de LII d'aggregats mono-disperses avec des températures de chauffe pour lesquels la sublimation des suies est négligeable. La méthode a été appliquée à des données de LII obtenus sur une flamme laminaire atmosphérique éthylene/air à différentes hauteurs. Les résultats obtenus montrent un bon accord entre les tailles des grosses particules évaluées avec la méthode TERF et celle obtenue par analyse des images TEM. En revanche l'accord n'est pas obtenu pour les petites particules, ce qui est attribué à un manque d'information sur cette classe de particule dans l'analyse TEM.

Des champs de fraction volumique de suies sont ensuite obtenus dans une cellule haute pression haute température dans les conditions opératoires du réseau ECN (Engine Combustion Network) par technique combinée de LEM et LII simultanées. Les mesures sont réalisées dans les conditions du spray A et incluent des variations paramétriques (température et dilution). La distance de Lift Off de la flamme est déterminée en parallèle par visualisation directe de la chimiluminescence OH. Des niveaux de fraction volumique maximale de 2–3 ppm sont obtenus dans les conditions nominales du spray A (i.e. 900K), et peuvent atteindre 12 ppm à haute température (1030 K). L'effet des variations de température et de concentration d'oxygène sur la formation et l'oxydation des suies et cohérente avec les résultats issus de la littérature.

Une méthode d'imagerie de taille de particules est développée. Elle est basée sur l'acquisition de deux images de LII obtenues à deux instants différents après le pulse laser et l'analyse de ces images à l'aide de la simulation du signal LII pour déduire les tailles des particules à partir du rapport des images. Une stratégie basée sur une analyse par modèle LII est développée pour évaluer les incertitudes de mesure. La dépendance aux conditions limites de l'imagerie de taille de particule par LII est ainsi évaluée. Les conditions limites considérées sont: température ambiante, pression, température de chauffe des particules, coefficient d'accommodation thermique, morphologie des suies…. Plusieurs régimes d'énergie laser et de pression sont évalués. Une combinaison optimale de timing d'acquisition est trouvée. La première image est prise au pic du signal de LII et la second image est prise 11ns plus tard avec un temps d'intégration doublé. L'analyse montre que cette stratégie permet d'optimiser la sensibilité de la technique à 60 bar. L'effet du jitter en temps et de la poly dispersion sont aussi analysés et l'erreur systématique de la pyrométrie à 60 bar est évaluée.

A l'issu de cette analyse par modèle, la méthodologie de mesure ainsi développée est utilisée pour effectuer des mesures expérimentales conduites dans les conditions du Spray A avec des variations de pression d'injection, de température ambiante et de composition. Les résultats sont comparés à des mesures de tailles de particules effectuées par analyse TEM d'échantillons de suies prélevés à différentes distances du nez de l'injecteur. Les différences obtenues entre les deux techniques sont discutées pour analyser les incertitudes de mesure et les sources d'erreur associées. Il est montré que dans un environnement moteur ou la pression est très élevée et ou les particules sont très petites, la méthode d'imagerie de tailles de particules par LII souffre d'un biais significatif vers les grosses particules.

Contents

1 Introduction

Soot is an amorphous-shaped particle emitted into the air during fossil-fuel combustion, biofuel combustion, and biomass burning as a result of incomplete reaction. It consists of amorphous carbonaceous particles and smaller amounts of sulfur, metallic ashes and other chemicals [1]. Soot production can be useful in various real-life and industry applications: Soot in a flame gives the flame its typical luminous orange or yellow appearance which makes torches and candles practical lighting sources. It helps furnaces and boilers efficiently transfer energy to heating pipes by thermal radiation [2]. Carbon black is essential for products such as tires, paints, varnishes and ink [3]. Airborne soot is reported to accelerate plant growth at certain situations [4] and it acts as a protector in the soil from insects and slugs [5] (the overall negative impacts on cultivation is greater though).

In almost all energy production plants and transportation systems, however, soot is an undesired by-product of combustion processes: Soot particles significantly affect the performance and durability of many engineering systems such as gas turbines and Diesel engines [6]. Particulate matter, in the form of smoke, can drastically reduce visibility [7]. Epidemiological studies indicated that exposure to elevated levels of particulate matter exacerbates pulmonary diseases, including asthma, bronchitis, and viral infections [8,9]. The World Health Organization reported that there is sufficient evidence that exposure to outdoor airborne particulate matter causes lung cancer [10]. Soot particles heat the air by converting sunlight into infrared radiation and emitting that heat radiation to the air around them. Furthermore soot particles contribute to the melting of glaciers at high-altitudes and polar regions by darkening them [1]. Both mechanisms adversely affect the climate and make soot a major contributor to global warming. In order to restrain these negative effects, legislation reduces particle matter emissions in transportation sectors.

Direct-Injection (DI) systems (Diesel and gasoline) are becoming the dominant technology in internal combustion engines in the European market due to their better fuel economy [11]. Soot emission is significant in these engines, because regions of high fuel concentration are generated and can form soot during the combustion process. Aftertreatment of exhaust gases using particulate filters are currently implemented in modern vehicles but this technology adds cost to production and maintenance and lowers the fuel economy [12]. Meeting the stringent regulations more efficiently requires the understanding of formation, growth, aggregation, and oxidation of soot. A quantitative understanding of these processes enables the development of methodologies to limit pollutant emissions and to develop soot prediction models to be used in CFD (computational fluid dynamics) codes. Powerful

diagnostics tools are required that measure the properties of soot in various environments and especially during the combustion. Optical diagnostic techniques are widely used for characterizing combustion systems as they are non-intrusive and, therefore, do not influence the process under investigation. Laser diagnostics have added advantages such as higher temporal resolution or acquiring cross-sectional information of three-dimensional flame structures. In soot diagnostics, soot volume fraction f_v, primary particle size, and its distribution during the combustion are essential information for the investigation of soot formation and burn out.

Laser-induced incandescence (LII) emerged as a powerful *in situ* technique for measuring soot particle sizes. Soot particles are heated via absorption of light from a laser pulse to temperatures well above the flame temperature and the subsequent blackbody radiation is recorded during the heat-up and cooling phase. Small particles cool down faster than large ones due to their larger surface-to-volume ratio and therefore provide signal with different decay times [13]. Quantitative particle-size information can be obtained from a best-fit comparison of the temporal signal decay and simulations based on the particles' energy and mass balance equations [14,15]. Similarly particle-size information with high spatial resolution can be also deduced by comparison of the local ratio of temporally-different LII signals from images and the simulations [16–18]. For particle sizing another frequently used method is transmission electron microscopy (TEM) measurements of thermophoretically sampled soot. Although it does not allow *in situ* measurements to be made, TEM is the broadly accepted reference measurement technique for size and structure determination [2]. Line-of-sight laser extinction method is widely preferred in soot volume fraction measurements. By coupling this method with the planar LII technique, spatially-resolved quantitative information can also be obtained.

The principal aim of this study is to optimize two-dimensional particle sizing via LII imaging for Diesel engine conditions and to assess its applicability in comparison to results of sampling measurements. The particle-size measurements with LII imaging is complemented with particle-size distribution analysis in a flame at atmospheric pressure, and soot volume fraction measurements in a Diesel jet. From an experimental point of view the study is structured in a three-stage time frame:

At the initial stage the development of particle-size imaging techniques is performed in a laminar non-premixed ethylene/air flame (Santoro burner) at atmospheric pressure. The steady-state nature of this flame, its well-known temperature properties, and the atmospheric pressure enable an easy-to-do performance assessment of the technique and an enhanced understanding of the involved physical processes. Soot particle-size imaging with LII is carried out with a single camera, where LII signal-decay is determined for each pixel through time-gate-sweeping of the camera gate relative to the laser pulse. These preliminary imaging experiments provide a roadmap for the size-imaging experiments at

high pressure in the succeeding stages. In addition to particle-size imaging, time-resolved (TiRe) LII measurements are also performed at various flame locations with a conventional photomultiplier tube (PMT) setup. Soot in this flame has poly-disperse size distribution and small and large particles show a distinctly different behavior. With a high temporal resolution signal, the aim of the study is expanded to the investigation of soot poly-dispersity at atmospheric pressure. A novel strategy, called **t**wo-**e**xponential **r**everse **f**itting (TERF), is introduced for determining particle-size distribution information from TiRe-LII. The evaluation is based on a simplifying exponential approximation and does not require any particle-size distribution assumption. It provides one large and one small mono-disperse equivalent mean particle size and a ratio of the contribution of these size classes. Size-dispersion results are compared with TEM results.

At the second stage soot volume fraction measurements are performed for Diesel engine-relevant combustion conditions. To avoid the complications of experiments in a real engine and to better decouple the impacts of different variables on fuel sprays, the measurements are conducted in an engine-relevant high-temperature high-pressure constant-volume pre-combustion vessel. To relate this research to other similar works in the literature, the experiments are conducted for the "Spray A" conditions that have been investigated within the Engine Combustion Network (ECN) with a multitude of diagnostics and simulations [19,20]. The study addresses the measurement of local f_v in transient and quasi-stationary cases of Spray A. Line-of-sight laser extinction is used to quantitatively measure the soot concentration along a line in the spray. This information is coupled with LII imaging for the quantification of the f_v maps for cross-sections through the combustion zone. OH-chemiluminescence imaging is used to determine the lift-off length, and is used to interpret the soot measurements. Additional measurements with parametric variations of the standard conditions permit investigations of the effect of the various operating conditions on the lift-off length and the soot level. These measurements provide a basis for understanding the combustion boundary conditions, and also provide the basis for interpreting the soot measurement results. By quantifying the effects of laser attenuation and signal trapping [21] the suitability of Spray A to LII and extinction diagnostics is explored. Furthermore, among different conditions, the most suitable one is identified to be used for particle-size imaging with LII in the next step.

At the final stage, strategies developed for particle-size imaging are applied to Diesel engine-relevant combustion. In order to understand the effects of high pressure on the particle-size imaging with LII and to quantify the uncertainties, the signal-ratio method is investigated analytically and numerically. The measurement strategies are adapted to engine conditions upon the model-based analysis. Based on these simulations, a sensitivity analysis of the LII signal with respect to boundary conditions that

are assumed for data interpretation is also performed. Additional parametric variations in pressure, temperature, and gas composition are carried out. Measurements are performed with two cameras and the LIISim code [22] is used to assess all these information within the present work. At each condition two-color soot pyrometry is performed to measure particle and –thus- bathgas temperatures. The LII results are compared to particle-size and size-distribution measurements by TEM of thermophoretically-sampled soot at multiple axial distances from the nozzle. By varying the fuel injection pressure, ambient temperature and oxygen concentration, their effects on the evaluated soot particle size and its spatial distribution are analyzed.

2 Research focus

In the present work, LII is used as the main technique for the quantitative measurements of soot particle size and volume fraction as mentioned in section 1. Therefore, it is aimed to obtain accurate results by optimizing the experimental technique in a combined approach that includes detailed data analysis to interpret the significance of acquired signals. Although LII is thought to be a reliable technique, there are many issues with the measurement. These can be grouped into experimental apparatus, numerical model, and signal evaluation topics. Smallwood described most of these known issues for conventional LII in ref. [23].

Poly-disperse size distribution of the soot particles is one of these issues in particle sizing with LII. The primary particle diameter d_p is one of the key indicators for interpreting the effects of soot formation and burnout. However, describing a poly-disperse soot ensemble at a location with a sole d_p may not always be sufficient. Information about the size distribution is therefore important for a better understanding of soot processes. Different solution schemes and LII signal processing strategies have been developed [24–31] for the measurements of particle-size distributions. However, all the strategies are based on assumed certain particle-size distribution shapes. They also suffer from being mathematically ill-posed, and having long computation times. The new method presented in this work, TERF, is an alternative to conventional mono-disperse equivalent mean particle-size evaluation. It differentiates between signal contributions from small and large particles. It determines mono-disperse equivalent mean particle sizes for both size groups and evaluates the relative ratio of particle number densities for both groups. Compared to time-consuming poly-disperse fitting algorithms, the extracted information is limited. Nevertheless, the TERF method evaluation is much faster which makes it suitable for real-time analysis. In chapter 4, overviews and associated problems for each of poly-disperse solution schemes are given, and the aspects of how the TERF method can be useful are explained.

The development of soot particles from liquid or vapor phase hydrocarbons mainly involves the pyrolysis, nucleation, coalescence, surface growth, agglomeration and oxidation processes [32]. The soot formation and oxidation processes are constantly competing within the flame and their rates depend on the fuel structure, oxygen content and gas temperature [33]. Glassman [34] classified hydrocarbons with respect to their sooting propensities. The effects of ambient temperature and reactant composition on soot are studied extensively in ref. [35–43]. Some of these effects, however, have not been fully understood, especially for high pressure conditions.

The vast majority of publications regarding the development of LII have performed measurements in laboratory flames for atmospheric pressure. The laminar non-premixed flames in Santoro or Gülder configurations and the laminar rich premixed flame in the McKenna burner are most frequently used within the LII community [14]. Although these laminar flames provide a near-ideal environment for development of the LII technique, they do not evaluate the performance of the technique over the full range of possible applications [23]. In many practical combustion devices, soot formation occurs at elevated pressure in time-varying turbulent flames where pressure, temperature, and species concentrations have a significant effect on soot formation [44]. In this work, it is aimed to further develop/optimize the LII technique so that the measurements could also be performed for Diesel engine conditions. The soot processes in a reacting Diesel jet are interconnected with injection and air/fuel mixing processes. Therefore, a thorough understanding of soot formation and oxidation can be achieved by an integrated analysis of various jet combustion parameters.

The Engine Combustion Network (ECN) aims to improve the fundamental understanding of Diesel spray formation and combustion in engines, and to develop predictive models to optimize these engines. It brings experimental and computational research together for collaborative comparisons of measured and simulated results at standardized conditions (Spray A operating conditions and its parametric variants) [20]. Spray A represents a relatively low-temperature Diesel engine combustion condition relevant to engines that use a moderate rate of exhaust-gas recirculation (EGR) [45]. The fuel used in Spray A is a single-component fuel, n-dodecane, which is known as a good surrogate for Diesel, and it enables a complete knowledge of the physical and chemical properties of the fuel. The community has investigated hydraulic properties, spray development, and ignition processes in the target sprays. Datasets from these measurements are available for the further development of experiments and for the validation of model-based simulations and it expands constantly with various experiments performed by different labs from around the world [20]. Prior to this present work, however, soot volume fraction measurements were not performed for the exact Spray A conditions, and therefore parameters like the soot formation and oxidation locations, soot inception time and optical thickness were unknown. Shortly before the start of this work Kook et al. [38] performed soot volume fraction measurements at the identical Spray A operating conditions with a different surrogate jet fuel. Because of the effects of molecular structure of fuel on soot formation [34], the exact trends of soot formation and oxidation processes could not be predicted prior to pure n-dodecane experiments.

In chapter 5 soot volume fraction measurements are derived for Spray A conditions with parametric variations of gas temperature and composition by performing the well-established simultaneous line-of-sight laser extinction measurements and LII imaging. Measurements were performed in an engine-

relevant high-temperature high-pressure constant-volume pre-combustion vessel. The optical thickness is measured to assess the suitability of Spray A conditions to such diagnostics. The effects of ambient temperature and oxygen concentration variations on soot formation and oxidation processes are analyzed.

Recording signal traces with fast multipliers is well-established for particle-size measurements. However, this approach is limited to point-wise measurements. The spatial distribution of particle sizes can be revealed only with repeating the measurements at different locations – an approach not possible for rapidly fluctuating situations like those in internal combustion (IC) engines. Will et al. [16–18] developed a strategy for two-dimensional particle sizing where LII signals are acquired at two delay times after the laser pulse with gated intensified cameras and where the particle size is deduced from the local signal ratio. This technique provided particle-size distributions with high spatial resolution for laminar flames at atmospheric pressure [16–18,46]. The loss in temporal information, however, reduces accuracy and precision of the resulting particle-size measurements.

In chapter 6, the applicability of time-gated LII particle-size imaging is first numerically investigated for engine-relevant conditions. At high pressure, the lifetime of the LII signal is significantly reduced due to enhanced heat exchange of the particles with their environment. Because of this rapid cooling, the normalized LII signal decay profiles for particle classes of different size fall into a very narrow envelope, and curves measured under different conditions become similar to each other. The effects of such convergence of signal decay profiles on particle sizing was mostly unknown and they are analyzed in this work. For LII under high-pressure conditions, a known problem is that in poly-disperse soot samples a non-uniform heat-up temperature distribution is reached among the different particle-size groups [27,44]. At high pressure, conductive cooling during the nanosecond laser pulse is not negligible which leads to lower heat-up temperatures of the small particles compared to the larger ones. In this work, the resulting variations in heat-up temperature are determined for moderate and high laser fluences for 60 bar and the effect on particle sizing is evaluated. LII diagnostics can also be affected by attenuation of the pump-laser [21,47,48]. Laser attenuation causes spatial variations in heat-up temperatures along the laser path. The influence of this effect on particle-size measurements is also evaluated.

For imaging applications, various detector gating strategies are assessed to maximize the sensitivity of the particle-size evaluation. Various gate widths and delays are convoluted with the simulated time-dependent signals. By determining the variation of the ratio of both gated signals within the range of expected particle-sizes, the sensitivity of the gating strategies can be obtained. Previous studies [48] showed that the gating approach can be significantly affected by timing jitter which was up to ±2 ns.

Because of the short signal lifetime at high pressure, such jitter can cause severe changes in the gated signals and their ratio. Effects of such timing jitter are included in the evaluation. The loss in the temporal information compared to the evaluation of full signal traces prevents a detailed analysis of particle-size dispersion. The evaluated particle sizes more represent mono-disperse equivalent mean particle diameters and are inherently biased to the larger sizes. The magnitude of this bias is investigated for soot ensembles with lognormal particle-size distribution. Additionally, an accuracy and jitter analysis for two-color pyrometry imaging of heated particles at high pressure is achieved based on Planck's thermal radiation modeling.

Following the numerical analysis in chapter 6, soot particle sizing with two-time step LII imaging is performed under the Spray A conditions with additional parametric variations of injection pressure, gas temperature and composition. The results were compared to particle-size and size-dispersion measurements from transmission electron microscopy (TEM) of soot thermophoretically sampled at multiple axial distances from the injector. With this work, the applicability and reliability of time-gated LII particle-size imaging for engine-relevant conditions is investigated for the first time in soot research community.

3 Background

Several measurement techniques exist for soot investigations. For a quantitative analysis, the photophysical processes in these techniques should be well understood. In this chapter the optical diagnostics applied in this work for temperature, f_v, and particle-size measurements are reviewed.

3.1 Temperature measurement

Knowledge of flame temperature can provide valuable insight for the processes responsible in soot production. Furthermore the bathgas temperature and the heat-up temperature of soot must be known to solve particles' energy and mass balance equations that is necessary in particle sizing with LII. In flames, the gas-phase temperature can be obtained by various *in situ* laser-based techniques such as coherent anti-Stokes Raman scattering (CARS) [49], laser-induced fluorescence (LIF) [50,51] or laser-induced thermal grating spectroscopy (LITGS) [52]. Emission-based techniques, on the other hand, generally employ a simpler optical setup, require less optical access and also have much lower cost when compared with laser-based techniques. Multi-wavelength optical pyrometry [53–55] is a well-established emission-based technique and is used to determine the flame temperature in this work. The technique allows temporally- and under some conditions spatially-resolved measurements. Furthermore, unlike the laser-based methods, the soot pyrometry can be used to measure the heat-up temperature of soot particles at any instant after the laser pulse in an LII measurement.

Two-color soot pyrometry

Soot in a flame stands at high temperatures, and as a result emits blackbody-like radiation, also called incandescence signal. Depending on temperature, the absolute intensity of this emission and the shape of its spectrum can change. In pyrometry soot emission is typically sampled at two (or three) different wavelengths using spectral filters. The relative intensity of the detected radiation at the different channels can then be related to temperature using Planck's law.

The Planck's law describes that the intensity of radiation I_λ of a particle at wavelength λ depends on the particle temperature T and its monochromatic emissivity $\varepsilon(\lambda)$:

$$I_\lambda(\lambda, T) = \varepsilon(\lambda) \frac{2\pi hc^2}{\lambda^5 \left(e^{hc/k\lambda T}-1\right)} \quad (1)$$

where c is the speed of light, h is Planck's constant, and k is the Boltzmann constant. By acquiring the incandescence signal S at two different spectral wavelengths and ratioing them, the following equation can be written:

$$\frac{S_{\lambda_1}}{S_{\lambda_2}} = C_{\lambda_1\lambda_2}\left(\frac{\varepsilon_{\lambda_1}}{\varepsilon_{\lambda_2}}\right)\left[\frac{\left(e^{hc/k\lambda_1 T)}-1\right)}{\left(e^{hc/k\lambda_2 T)}-1\right)}\right] \quad (2)$$

where the system constant $C_{\lambda_1\lambda_2}$ is a function of the ratio of detection wavelengths, spectral bandwidths, the quantum efficiency of the detectors, and the combined lens and filter transmittance at the respective wavelength [46,54]. $C_{\lambda_1\lambda_2}$ can be determined using a blackbody source of known temperature for calibration. Alternatively, various light sources of known incident irradiance on a diffuser of known scattering efficiency and angular distribution can be used for such calibration [56]. Normally ε is a bulk property of a material and its concept does not precisely apply to soot; in the analysis of soot incandescence, it can be viewed as efficiency of radiation and absorption [46]. Within the Rayleigh regime, $\pi d_p/\lambda_{\mathrm{ex}} < 0.3$, (with the wavelength λ_{ex}), ε can be related to the soot absorption function, $E(m)$:

$$\varepsilon(\lambda) = \frac{4\pi d_p E(m)}{\lambda} \quad (3)$$

m is the soot refractive index and the values of wavelength dependent $E(m)$ obtained from different experimental conditions are presented in [14,57–63]. In the current work, $E(m)$ is calculated according to the linear expression proposed by Snelling et al. [60]:

$$E(m,\lambda) = 0.232 + 1.254 \cdot 10^{-4}\lambda \quad (4)$$

Eq. 2 is an implicit equation of temperature that can be solved iteratively for a measured signal ratio. A much practical lookup table approach can be also used to calculate the temperature in Eq. 2 for a given system constant and various signal ratios [64].

The selection of detection wavelengths in soot pyrometry is a problem of a multivariable optimization and different factors affecting the detection system performance and the accuracy should be taken into account. Liu et al. [65] showed how the detection wavelengths affect the sensitivity of soot temperature measurements. To achieve a better accuracy for soot temperature, it is desirable to use a shorter lower detection wavelength and a longer upper detection wavelength in the spectral range of about 400 nm to near infrared [65,66]. It is also recommended that the filter bandwidths are narrow compared with the spacing in-between.

One concern in soot pyrometry is the self-absorption of the incandescence signal on the detection path. As shown in the Eq. 3, the emissivity of soot, hence the absorption efficiency, is wavelength

dependent and therefore signals at different spectra are subjected to different attenuation. Depending on the local f_v the soot pyrometry measurements may show systematic deviation from the actual temperature. Schraml et al. [66] performed extinction measurements to correct the Planck spectra for wavelength-dependent absorption. For low or moderate f_v, the systematic error due to self-absorption is limited.

Although two-color pyrometry is a robust method to measure the LII heat-up temperature of soot particles, it has some additional drawbacks in measuring the bathgas temperature. First, the obtained temperature is the soot temperature and not the gas-phase temperature. However, it can be assumed that these temperatures are similar when particle and gas phase are in thermal equilibrium [55,67,68]. Second, this method is a line-of-sight technique and if the flame under investigation has temperature gradients along this line-of-sight direction, the measured temperature is strongly biased to the highest temperature layers [69]. When imaging of cylindrically symmetric flames, the lost spatial information through the projection can be recovered by performing a tomographic inversion and the data in pixel rows can be deconvoluted to radial profiles [70–72].

3.2 Soot volume fraction measurement

f_v is the relative volume occupied by the particles in respective gas sample and is an important parameter to understand the soot mechanisms. One well-established method to measure f_v is using LII coupled with the above mentioned multi-wavelength optical pyrometry after an absolute intensity calibration of the detectors (auto-compensating LII) [8,73]. In the present work, LII imaging coupled with line-of-sight extinction is used:

3.2.1 Laser extinction

The laser extinction method (LEM) is a non-intrusive line-of-sight technique based on the attenuation of light when a laser beam passes through a particle cloud, see Fig. 1. The attenuation of light is caused both by elastic scattering and absorption in the particles [21,74].

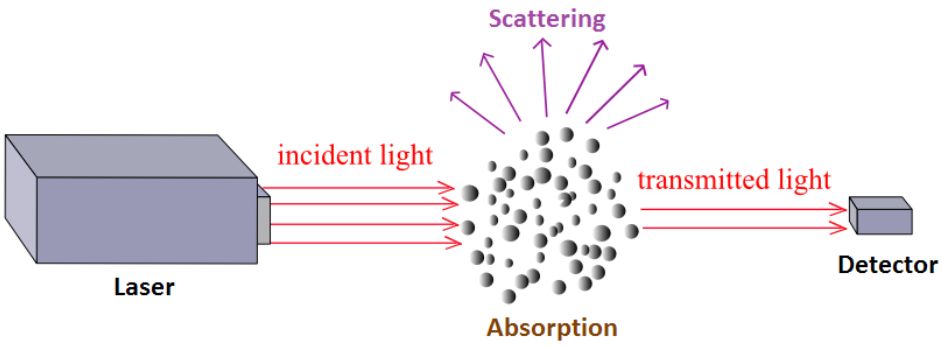

Fig. 1: Laser extinction method

The relation between the incident light intensity (I_o) and the light intensity after passing through the particle cloud (I) is given by Lambert-Beer's law, Eq. 5:

$$\frac{I}{I_o} = \exp(-KL_{LEM}) \quad (5)$$

where L [m] is the path length through the cloud and K [m^{-1}] is the mean extinction coefficient along this path length. Following small particle Mie theory [39] (soot morphology corresponds to the requirements of Mie's theory for small particles, i.e., spherical geometry) the path-length-averaged extinction coefficient can then be related to the soot volume fraction as given in Eq. 6:

$$K = \frac{k_e}{\lambda} f_v \quad (6)$$

where λ [m] is the laser wavelength and k_e is a non-dimensional optical coefficient that depends on the soot morphology and the particle size. This coefficient can be related to the soot absorption function at the detection wavelength [39]:

$$k_e = (1 + \alpha_{sa})\, 6\pi\, E(m) \quad (7)$$

Where α_{sa} is the scattering-to-absorption ratio and it corresponds to the ratio of the scattering and absorption cross-sections. As it was shown for $E(m)$ in section 3.1, the accuracy of this value is debated in the literature and a systematic error on this value must be taken into account [75]. Based on Rayleigh-Debye-Gans (RDG) theory, Manin et al. [76] showed that k_e depends on the soot primary particle diameter and aggregate size. and In this work, a value of $k_e = 7.8$ is used [59] and it is assumed to be uniform throughout the flame [77].

If the laser beam is replaced with a diffused light source [75,76], spatially resolved f_v measurements can also be achieved by line-of-sight extinction. The known issues in all types of extinction measurements that should be taken care of, are forward scattering of the incident light, collection of the flame luminosity, and beam steering of the incident light [35]. These problems and remedies to mitigate the related uncertainties will be explained more in detail in section 5.5.

3.2.2 f_v imaging with LII

As introduced in section 1, LII is an optical diagnostics technique that uses a pulsed laser to heat soot particles to temperatures significantly above the ambient temperature and uses photo-detectors to record the incandescence emitted from these heated particles. LII can be applied either in a pointwise or in an imaging manner, and for soot volume fraction measurements the latter is mostly preferred.

Incandescence is a blackbody-like radiation and strongly depends on the temperature of the soot particles. Therefore, the signal intensity per particle increases with the energy fluence (i.e., pulse energy per area) of the pulsed heating laser, because the temperature increases. This correlation is valid (but not linear) until soot sublimates at around 4000 K. Beyond this point, excess energy does not further increase the particle temperature or LII signal. In contrary, sublimation of particles leads to a decrease in the signal due to rapid evaporation of the radiating particles [14].

For soot ”concentration” measurements it is important that the LII signal is proportional to the amount of soot particles and their size. Assuming a homogenous temperature distribution of the laser-heated soot particles in a measurement volume the signal is proportional to the f_v. f_v is presented in terms of parts per million (ppm). TEM analysis [78–80] shows that soot particles consist of agglomerated nearly spherical primary particles. Within one measurement location it is often assumed that the size of the primary particles and the aggregates are nearly the same [81,82]. With this simplification, the relation between f_v and the LII signal (I_{LII}) turns into a linear form as given in Eq. 8:

$$f_{\mathrm{v}} = \alpha\, I_{\mathrm{LII}} \qquad (8)$$

where I_{LII} can be acquired by a camera and can be written in photon-counts units. The assumption of a homogenous temperature distribution among the heated soot particles is crucial for the accuracy of the volume-fraction measurement. Nevertheless, possible inhomogeneities in the spatial profile of the laser and inhomogeneous initial temperatures of particles prior to the laser pulse necessitate an additional effort to make this assumption valid. One simple way of providing uniform conditions is to bring the particles into the sublimation regime with excessive energy. Then, all particles are heated to the sublimation temperature. However, the laser profile has a key influence on the LII signal in the sublimation regime. As mentioned above, rapidly sublimating particles cause a decrease in the overall LII signal when all particles contributing to the signal are exposed to the same laser fluence (top-hat laser profile in direction of signal detection). An (approximately) stable LII signal intensity at increasing laser power can be maintained by a laser sheet with a Gaussian spatial profile. The reduced signal caused by the sublimating particles in the center line of the laser beam is compensated by the increasing temperature of particles exposed to wings of laser beam. The resulting “plateau zone” where the signal is insensitive to variations in laser fluence is often used in cases where beam attenuation and laser pulse-to-pulse energy variation needs to be compensated [82]. This fluence dependence of the LII signal as a function of the spatial profile of the laser beam was evaluated by Michelsen et al. [83] and is shown in Fig. 2.

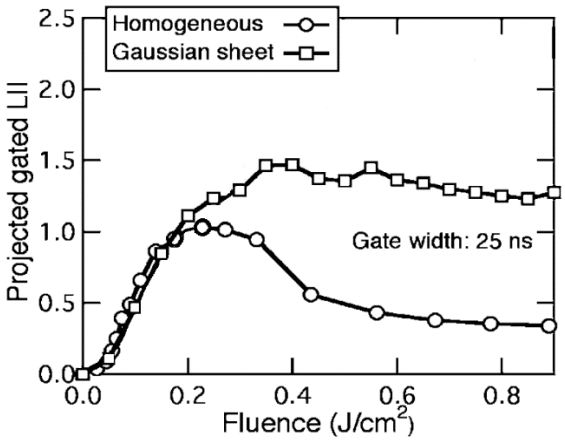

Fig. 2: Fluence dependence of LII signal as a function of laser beam spatial profile for top-hat (homogeneous) and 1D Gaussian (Gaussian sheet) profiles. The results for Gaussian profile was simulated by summing the fluence-dependence measurements from a top-hat profile weighted by a Gaussian distribution in one dimension (squares). Gated detection was simulated by integrating the time-resolved signal over the first 25 ns after start of particle heating [83].

The threshold for this signal saturation regime is given as ~0.3 J/cm^2 at 1064 nm [14]. Detailed descriptions of the effects of the spatial laser profile have been reported [14,55,83]. The f_v measurements with LII imaging carried out within this study use the high-fluence approach with a laser light sheet where the laser fluence distribution is approximately Gaussian in the direction of signal detection.

3.2.3 LEM-LII coupling

LEM provides quantitative but path-integrated information about the soot volume fraction. LII, on the other hand, yields information about the spatial distribution of the soot volume fraction in a selected cross-section but is not quantitative per se. By aligning the two systems in a way that the LEM line-of-sight is part of the LII cross-sectional area it is possible to use the LEM result to calibrate the LII signal integrated along the same direction of LEM pathway as long as the LII image covers a cross-section though the entire soot cloud. In a turbulent environment, the soot volume fraction at a given location can vary considerably with time. Therefore, it is important to consider the different temporal characteristics of LII and LEM measurements. While the LII signal shows the instantaneous spatial distribution of soot, LEM depends on the soot during the integration time (that can be considerably longer). For minimizing the effect of this, LEM signals recorded within short integration times at nearly identical instants should be used for the calibration of the LII images. In contrast, a phase-averaged calibration in a quasi-stationary part of the spray has been used in [39].

From the combined measurement, a calibration factor can be derived that connects the LII signal intensity integrated along the path of the LEM laser and the laser attenuation and the laser attenuation with the soot volume fraction. The LII signal along the LEM laser path is integrated according to Eq. 9:

$$KL_{\mathrm{LII}} = \int_0^L I_{\mathrm{LII}} dx \qquad (9)$$

By combining Eq. 5, 6, 8, and 9 one can calculate the linear calibration constant α in Eq. 8 and use Eq. 10 for soot the determination of volume fractions for the entire LII image [21].

$$f_{\mathrm{v}}(x,y) = \alpha I_{\mathrm{LII}}(x,y) = \frac{\lambda}{k_e}\frac{KL_{\mathrm{LEM}}}{KL_{\mathrm{LII}}} I_{\mathrm{LII}}(x,y) \qquad (10)$$

3.3 Particle sizing

The primary soot particle diameter d_{p} is another important quantity to understand soot mechanisms. d_{p} shows an immediate reaction to any change in the ambient temperature or oxygen availability. The size and distribution of particles can be measured by various *in situ* techniques such as photoionization aerosol mass spectrometry (PIMS) [84], small angle X-ray scattering (SAXS) [85], and scanning mobility particle-sizer (SMPS) [86]. In this work particle size of soot is obtained via TiRe-LII and LII imaging coupled with LII modeling. The *ex situ* technique TEM analysis of thermophoretically sampled soot is also used to measure the reference d_{p} for validation and calibration purposes.

3.3.1 TiRe-LII

The discovery of LII as a potential diagnostic technique for soot particle sizing traces back to 70's [87,88]. It was first considered as an experimental tool by Melton [13]. He numerically showed that LII could be used to deduce information of relative soot volume fraction, particle temperature and primary particle-size distributions. The first quantitative application of LII as a diagnostic for soot particle sizing was made by Will et al. [16] and Roth et al. [24]. Almost a decade later, Dankers et al. [31] introduced a simplified approach to evaluate the particle-size distribution. Michelsen [89] introduced a new heat and mass balance model that also accounts for oxidation, melting, and annealing of the particles and non-thermal photodesorption of carbon clusters from the particle surface. LII model modifications for aggregates were presented for the first time by Snelling et al. [60] and were improved by Liu and coworkers [90,91]. Hofmann et al. [29,68] conducted particle-size measurements with two-color LII at high pressure. Particles of non-carbonaceous materials such as metal and silicon were also measured with TiRe-LII [92–94]. Many different experimental approaches and data evalua-

tion techniques exist and are employed by various research groups that are currently working on making LII truly quantitative. In order to strengthen the community, a series of joint meetings, called LII Workshop, has been established biennially since 2005 to discuss the status of the current understanding regarding LII diagnostics.

Particle-size measurements with TiRe-LII are based on the fact that, after the initial laser pulse, smaller particles cool down faster than large ones due to their larger surface-to-volume ratio [13]. In a quantitative approach, assuming that all soot primary particles are spheres, the temperature and size of any known particle size can be modeled for any given time by solving the energy and mass balances. As a consequence, the size of a particle can be evaluated from the temporally-resolved temperature or incandescence signal by using a numerical scheme. In this present work, LIISim, developed by Hofmann et al. [22,29] is used for this analysis. The heat exchange mechanisms considered in the LIISim are:

$$\dot{Q}_{\mathrm{abs}} = \dot{Q}_{\mathrm{int}} + \dot{Q}_{\mathrm{cond}} + \dot{Q}_{\mathrm{rad}} + \dot{Q}_{\mathrm{evap}} \qquad (11)$$

where $\dot{Q}_{\mathrm{abs}}$ is the energy flux of laser absorption, $\dot{Q}_{\mathrm{int}}$ is the rate of change of total internal energy, $\dot{Q}_{\mathrm{cond}}$ is the energy flux related to heat conduction, $\dot{Q}_{\mathrm{rad}}$ is the heat loss due to radiation, and $\dot{Q}_{\mathrm{evap}}$ is the energy flux due to evaporation of material from the surface. The latter term is effective only when the total energy gain due to absorption is sufficient to heat the particle above the vaporization threshold. Once the evaporation starts, soot particles are subjected to a mass loss and the mass of the gas phase increases. This mass balance is described as

$$\frac{dm_{\mathrm{p}}}{dt} = J_{\mathrm{evap}} \qquad (12)$$

with the particle mass m_{p}, the time t, and the mass flux J_{evap}. The underlying physics of all heat- and mass-exchange mechanisms used in LIISim are explained in the literature [22,29] and therefore will not be discussed here. Even though LIISim includes an evaporation sub-model, it should be noted that the current understanding of evaporation is not accurate. Therefore, it is recommended to avoid high laser fluences to keep the soot temperature below the vaporization threshold. For atmospheric conditions, evaporation starts around 3300–3400 K [27] and becomes considerable above 3700 K, however soot evaporation at elevated pressure is not exactly known.

LIISim allows choosing between mono- or poly-disperse particles. It is known that soot formation, surface growth, and oxidation are continuous processes and therefore primary soot particles in a flame are poly-disperse which LIISim describes as log-normal distributions. In real systems, primary particles tend to form aggregates [95,96]. A soot particle within an aggregate cools down slower than

an isolated single particle because of shielding by surrounding particles. These effects are considered in LIISim as well, and the details of poly-dispersion and aggregation can be also found in Refs. [14,22].

For moderate or low laser fluence, which can be simulated by keeping heat-up temperatures below ~3500 K, evaporation is negligible and cooling is dominated by heat conduction. Fig. 3 shows normalized LII signals for various particle sizes at atmospheric and engine-relevant conditions, i.e. at 1 and 60 bar. Such a collection of simulated data that forms the basis for subsequent analysis is called a signal "library" in this thesis. Increasing pressure further increases conduction and significantly reduces the LII lifetime [97] as can be seen in the time ranges of plots in Fig. 3.

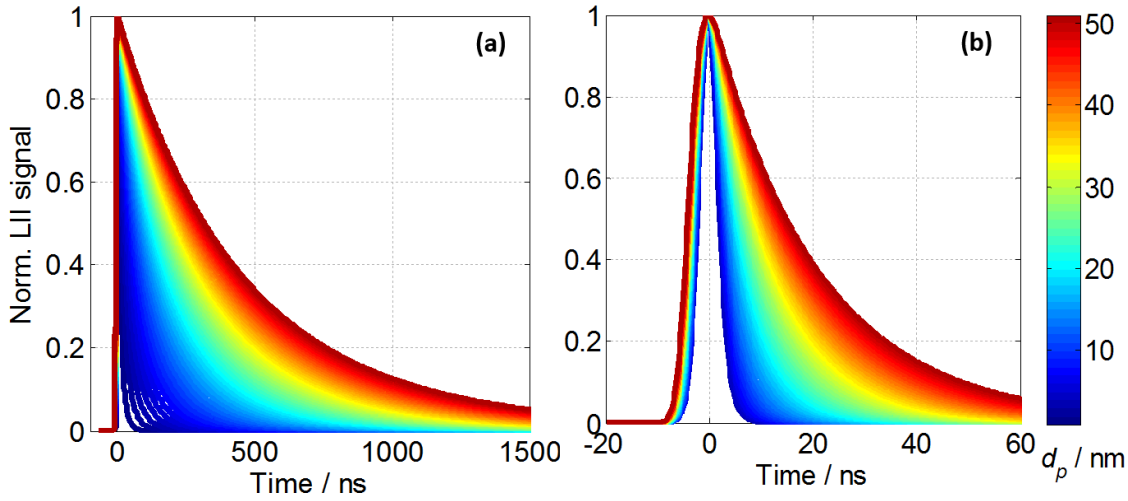

Fig. 3: LII signal "library" showing normalized time-dependent LII-signals for various primary soot particle diameters (d_{p}) at 1 bar (a) and 60 bar (b).

In these simulations the particles are assumed to be graphite-like and hence values of material constants associated with graphite are used [68,98]. For heat conduction the Fuchs approach [99] is chosen in LIISim that is known as the most appropriate model for particle-gas energy exchange in a wide range of gas pressures [100]. Other relevant boundary conditions are given in Tab. 1.

Tab. 1: Simulation parameters for the LII model

LII model input	**Atmospheric condition**	**Engine-relevant condition**
Ambient pressure	01 bar	60 bar
Detection spectral range	410–440 nm	410–440 nm
Bathgas temperature	1800 K	1800 K
Laser fluence at 1064 nm	0.08 J/cm^2	0.15 J/cm^2
Laser duration (FWHM)	7 ns	7 ns
$E(m)$	0.4	0.4
Aggregate size	50	50
Thermal accommodation coefficient	0.25	0.25

TEM studies of thermophoretically sampled soot from high-pressure combustion [12,79,101] show that primary particle sizes typically vary in between 5 and 40 nm. Fig. 3b shows that in this range the LII signal lifetime (time between 100 and 5 % of peak signal) varies from ~5 to ~50 ns. Therefore, when determining particle sizes from LII lifetimes, small uncertainties in data acquisition or modeling can lead to considerable errors. Fig. 3b shows that particle-size-dependent conductive cooling at high pressure is already relevant during the heat-up phase as each curve has a different shape. In practical applications, nano-second Nd:YAG lasers are widely preferred in LII soot research for their availability, high power and pulsed operating modes. These lasers have typically Gaussian temporal profiles with a full width at half maximum of 6–8 ns. Particles reach the maximum temperature only after some delay (~7 ns) after start of absorption. Within this period, particles loose energy at different rates depending on their size and therefore they have different signal histories in this phase. As a consequence each particle-size class reaches a different peak temperature [44]. This shows that including the heat-up phase in the simulation of the LII signal is essential in high-pressure LII particle sizing. Effects related to the heat-up phase in high-pressure environments are discussed in section 6.1.2.

3.3.2 Particle-size imaging with LII

The method is based on evaluating gated LII signals acquired with intensified cameras consecutively after the laser pulse and using LII modeling to deduce particle size from the ratio of local signals. With the state-of-the-art intensified camera technology, it is not possible for a single detector to provide consecutive images within the typical LII cooling time and multiple detectors (that are in few cases combined into a single “camera”) must be used. The temporal resolution of the collected data depends on the number of imaging detectors. In experiments in stationary flames the temporal LII signal trace can be determined with a single imaging sensor through time-gate sweeping relative to the laser pulses [16,17,46]. Fig. 4 shows an example of a LII signal trace that was constructed with 95 images acquired at different delays after consecutive laser pulses. The curve is normalized with respect to its peak point. Each data point is an ensemble average of a pixel-bundle in a 2 x 2 mm^2 area at 50 mm height above burner (HAB). For this measurement a co-annular non-premixed flame (Santoro burner) [102–104] was used at atmospheric pressure (also shown in Fig. 4). Five randomly chosen LII images in the figure have the identical color-mapping and the reducing signal intensity with increasing delay can be clearly seen. The accuracy of time-gate sweeping method is verified by comparing the constructed decay curve with a PMT acquired high-temporal resolution LII signal. Both signals are recorded at the identical flame location, HAB 50 mm and they are normalized with their respective peak

points. Each signal is ensemble average of 100 consecutive single measurements. Two curves are satisfactorily overlapping as shown in Fig. 5. The optical setup used in these measurements and the laser settings will be introduced more in detail in section 4.5.

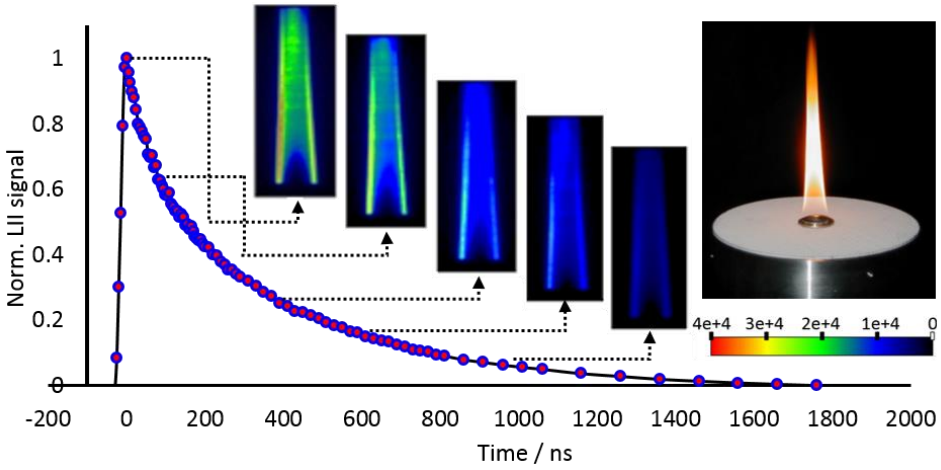

Fig. 4: A temporal LII signal trace determined through time-gate sweeping of camera relative to the consecutive laser pulses at 95 time delays.

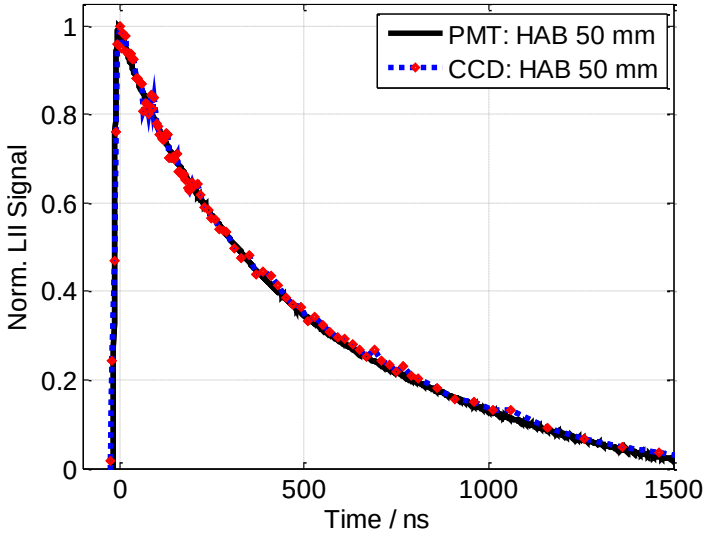

Fig. 5: LII signals acquired with a PMT and a camera (CCD) through time-gate sweeping. Both signals are acquired at the same flame location. Each signal is ensemble average of 100 single measurements.

For particle sizing two images are sufficient. These two images must capture different temporal information so that the ratio of both signals is a sensitive measure of the decay. Both images can be acquired either with various delays [17,82] and/or gate widths [105,106] within the signal decay. For each combination of delays and gate widths, signals and signal ratios can be computed by convoluting the temporal characteristics of the detectors with the respective LII signal library (cf. Fig. 3). There is a unique ratio of the two gated signals for each particle size as shown in Fig. 6. The ratio relates the

signal in the second gate (delayed) to the first gate and therefore is always below unity. The resulting look-up table can be then used for evaluation of the measured data. The example shown in Fig. 6 is based on data for the conditions in Tab. 1 at 1 bar and presents "look-up curves" for laser fluences from 50 to 100 mJ/cm^2. These curves are based on evaluated libraries simulated for all fluences with 10 mJ/cm^2 increments. Virtual gates with top hat (rectangular) temporal profiles of 20 ns are assumed for both gates.

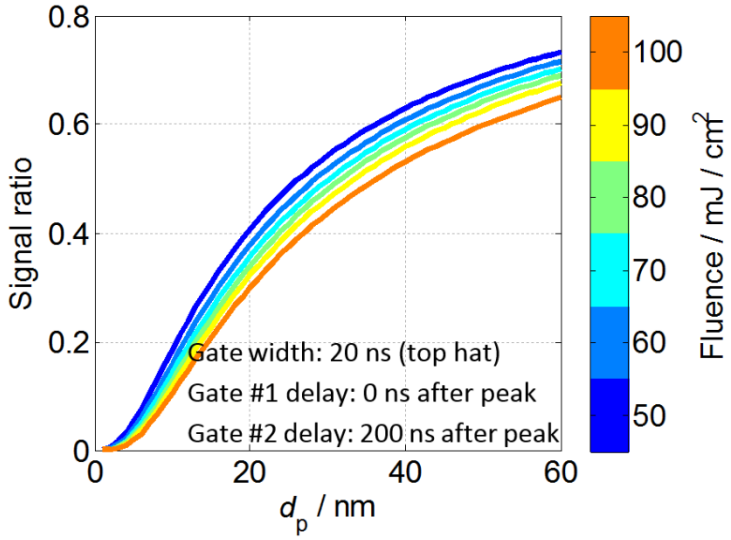

Fig. 6: Look-up table for the particle size as a function of signal ratio created from a modeled library for 1 bar. The influence of the laser fluence is shown for 50 to 100 mJ/cm^2 (10 mJ/cm^2 increments).

The comparison of an experimentally-obtained signal ratio image with this look-up table allows to determine particle sizes for each pixel. It is, however, important, that local conditions are well known. Fig. 6 shows that for a given signal ratio, a variation in the laser fluence by 50 mJ/cm^2 can cause a 30% deviation in the evaluated particle size.

To demonstrate the importance of input parameters in particle-size imaging, the combined effect of the aggregate size and the local bathgas temperature on the particle-size imaging is measured with the LII images acquired at the co-annular non-premixed flame between 40 and 65 mm HAB. As a typical characteristic of non-premixed flames, aggregate sizes changes with the flame height [62] and the values shown in Fig. 7 are estimations based on TEM analysis of thermophoretically sampled soot. The nature of this soot sampling process and the small radius of the flame does not allow a measurement of gradients in the radial direction. Therefore aggregate sizes along the radial direction are unknown and are assumed uniform at each flame height. In non-premixed flames large gradients can be observed in the bathgas temperature [103,107]. It should be also noted that any spatial variation in the bathgas temperature causes the same amount of change in the heat-up temperature (assuming

constant $E(m)$). In this analysis the bathgas temperature distribution of the flame is imported from the ref. [103] and shown in Fig. 7 at six different HAB for the left hand side of the axis-symmetric flame. The spatial resolution in the radial direction is set to 32 nodes per line by performing a linear interpolation between the known data. For every node in every line, a unique LII library is simulated with the respective aggregate size, bathgas and heat-up temperatures. The remaining simulation parameters are those from Tab. 1 at atmospheric condition.

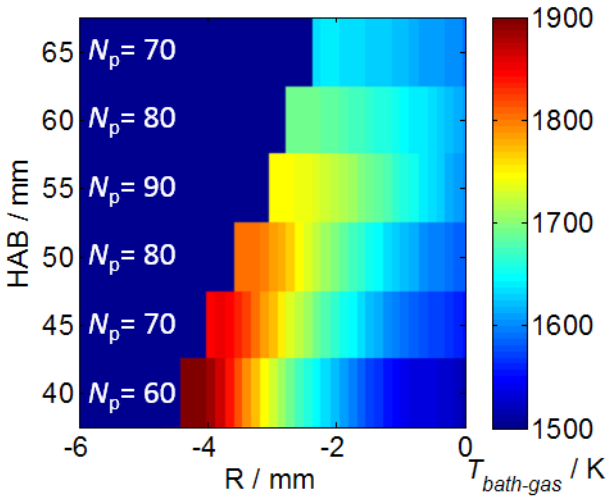

Fig. 7: Bathgas temperature distribution within the left hand side of the co-annular non-premixed flame. The image consists of radial profiles at six different HAB. At each HAB, the respective aggregate size is given.

Even though the flame is laminar and protected with a chimney (cf. section 4.5) in this experiment, slight random movement of the flame cannot be fully avoided. On the other hand, a precise one-to-one matching of pixels showing the identical physical location is essential when calculating signal ratios. Ensemble averaging of single measurements helps for increasing the correlation, nevertheless it does not provide a 100% satisfactory mapping of pixels. To further reduce the uncertainty related to this problem, radial profiles are created at every 5 mm HAB in the measurement domain, by binning the pixels vertically in 2-mm-tall pixel columns. Once the profiles are created, they are shifted horizontally until the respective maxima intensity pixels of different time-gates meet at the same point. By doing this, a perfect matching of pixels along the profiles is achieved with a compromise of spatial resolution. A second challenge in this experiment is the laser-attenuation (cf. section 6.1.3) which causes a spatial variation in laser fluence, hence in heat-up temperature, along the beam propagation direction. The stronger intensity at the left wing of the flame (laser enters from this side) is shown in the LII images in Fig. 4. The LII signal emitted from the right wing is 40% weaker compared to that of the left wing. To avoid any complexity related to this non-uniformness, in this analysis only the left hand side of the flame is considered.

The starting time of the first gate is fixed to the peak signal and the delay time δ for the second gate is set to 200 ns after the first gate. The width of both gates is 20 ns. Once the signal ratio is calculated, the particle size in each pixel is evaluated with the respective library of that specific location and shown in Fig. 8a. In another attempt, the spatial variations of the bathgas temperature and the aggregate size in the measurement domain are not taken into account, and at all locations one single library is used that was created with a bathgas temperature value of 1800 K and an aggregate size of 60. The particle sizes evaluated with this single library are shown in Fig. 8b, and Fig. 8c shows the particle-size difference between the two methods. Although an evaluation with a single library is much more time effective, local deviations of the result are as high as 25%. Effects of simulation input parameters at high pressures are discussed in section 6.1.1.

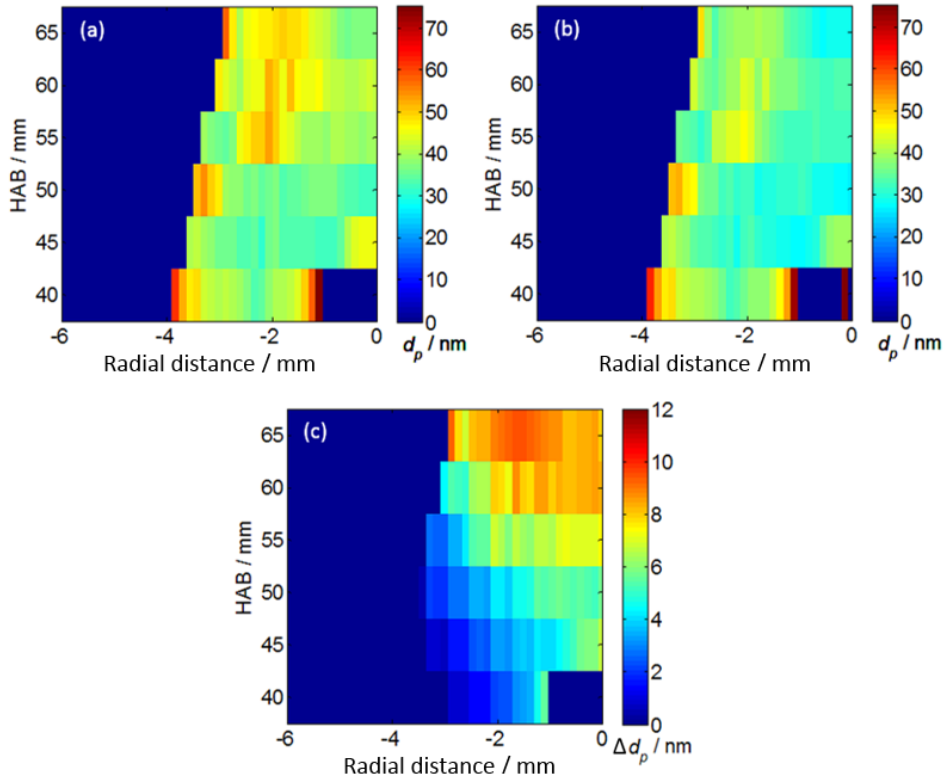

Fig. 8: Particle-size distribution in the left hand side of the axis-symmetric non-premixed flame between 40–65 mm HAB. At each node particle sizes are evaluated with (a) unique libraries created with the respective aggregate size, bathgas and heat-up temperature, (b) with a single library created with N_p = 60 and $T_{bathgas}$ = 1800 K. (c) Temperature difference between the two methods.

Crucial for LII particle-size imaging is optimizing the delays of the detector gates. Will et al. [17] showed an optimum timing for high-fluence scenarios that provided the minimum contribution from photoelectron noise to the signal ratio. Mewes and Seitzman [82] reported that both gates must be placed in the temporal section of particle cooling past the end of the laser pulse to provide good size

sensitivity. To optimize gate timings, multiple effects must be considered such as particle-size dispersion, signal-to-noise ratio and LII lifetime. Especially at atmospheric pressure, where the LII signal lifetime is much longer than the camera gate width, additional information about particle-size dispersion can be derived by altering the delay timing. To demonstrate this, particle sizing in the non-premixed flame is performed with five delay times δ of the second gate from 300 to 700 ns and the results are shown in Fig. 9. The starting time of the first gate is again fixed to the peak signal and the width of the gates are kept at 20 ns. Before the ratioing, high resolution images are again reduced to spatially overlapping radial profiles with 5 mm intervals as explained above. The evaluation is performed with the multiple libraries those are simulated with location-specific input parameters. In Fig. 9 half-side images (profiles) are mirrored around the flame axis for an enhanced visualization.

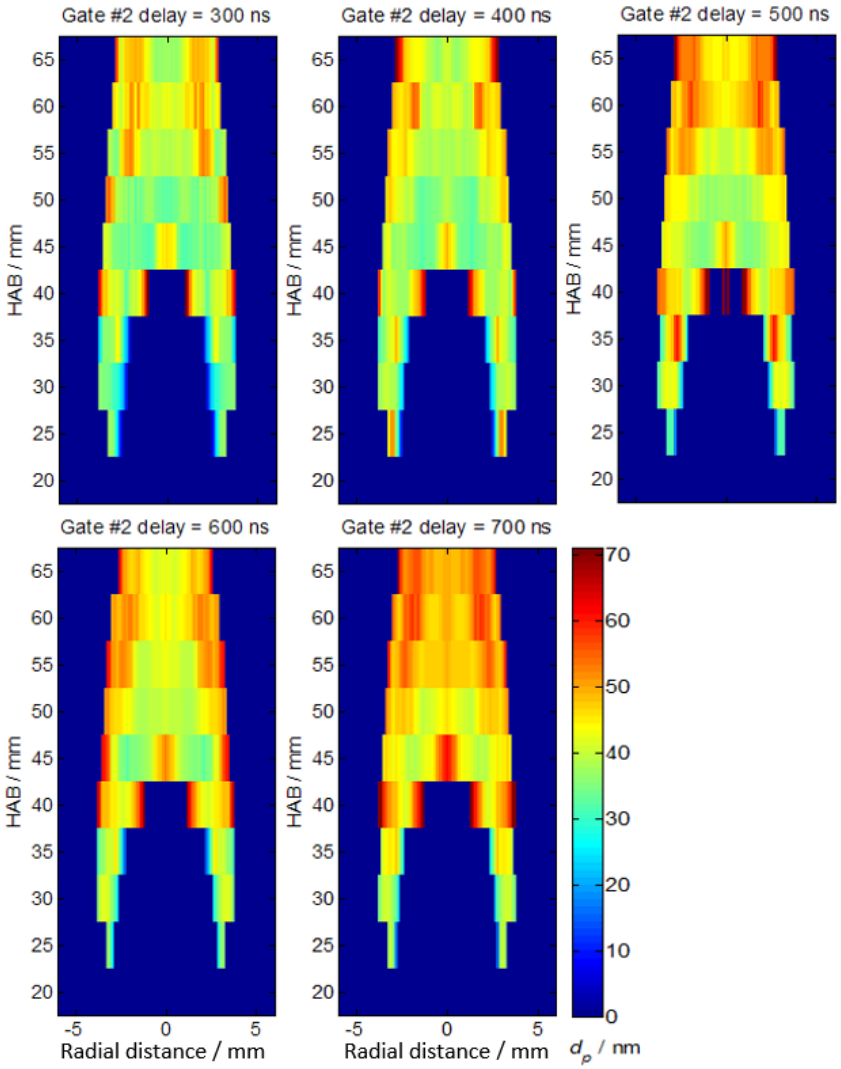

Fig. 9: Particle-size distribution in the non-premixed flame evaluated with five different delays of the second gate. The first gate is fixed to the peak signal. The analysis is conducted only in the left hand side of the flame

and the resulting image is mirrored around the flame axis. With increasing delay smaller size classes fade out and evaluated particle size increases.

As mentioned earlier, in a poly-disperse soot ensemble, particles in smaller size-classes reach thermal equilibrium faster than the larger particles. Therefore, at long delays, the LII signal does not contain information from such small size-classes and info about large particles is gained. This preliminary particle-size imaging study at this non-premixed flame provided an insight for the two-time step size-imaging technique. Experience gained at this step formed a basis for the measurements at high pressure in the succeeding stages. For the 60 bar case considered in section 6, weak signals and hence signal-to-noise ratios are the major concern. This strongly restricts the choice of potential gate timings. Fig. 3b shows that the LII signal of a 20 nm diameter particle falls below the 10% of its peak value in less than 20 ns. Therefore, only gates in the vicinity of the signal peak provide sufficient signal. Effects of gate timing are discussed in section 6.1.4. In turbulent flows time-gate sweeping at consecutive laser pulses is not possible. Thus, a two-camera strategy for instantaneous imaging is necessary (cf. section 6.2.1).

3.3.3 Transmission electron microscopy (TEM)

The principle of TEM is similar to the principle of optical microscopy. However, the wavelength associated with the electron beam is much lower than the wavelength of light and the resolution in electron microscopy is clearly improved. The use of electrons require the use of ultra-thin samples (thickness of about 100 nm) to be as transparent as possible to electrons. The major interest of TEM is to obtain structural and morphological information [108].

For TEM soot deposited on special support grids via thermophoresis. Thermophoretic deposition is driven by the presence of a temperature gradient in the vicinity of a cold surface in a particle-laden gas [109]. Therefore the probe must be much colder than the flame. This can be achieved by introducing a probe that is initially at room temperature rapidly into the hot flame with a pneumatic or mechanic actuator. The exposure time should be long enough to capture sufficient material but short enough to present a cold surface to the flame-born particles. This cold surface serves a second important purpose which is that it freezes heterogeneous reactions of the captured particles. This freezing prevents changes in the soot morphology after the particles have impacted upon the cold surface [109]. When a dynamic probing is not possible, for example in a high-pressure spray vessel or in an IC engine [12,79,110], TEM grids have been installed on a stationary probe. The temperature difference necessary for thermophoresis is then realized by keeping the combustion duration limited.

TEM grid materials depend on the application (temperature, hardness, corrosion resistance, etc.). All grids are 3.05 mm diameter, but the thickness (a few micrometers) varies with mesh size. The mesh

size of the grid indicates the number of holes per inch and generally varies from 50 to 400. The grid material is responsible for rigidity, and the sampling of the soot is achieved by the electron transparent carbon film coated on this grid, see Fig. 10. Depending on the necessity, the thickness and the structure (solid, amorphous, holey, or lacey) can vary.

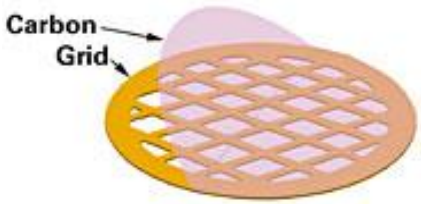

Fig. 10: Schematic of a TEM grid [111].

From the analysis of TEM images of soot aggregates, different information such as the primary particle-size distribution, and the number of primary particles per aggregate, N, and the fractal dimension, D_f, can be obtained. Although frequently considered as a primary reference method, TEM has uncertainties. The *ex situ* nature of the sampling (changing flame flow, changing local temperature, etc.) has an effect on the soot processes. The TEM images are only projection of soot aggregates, therefore interpretation of the three-dimensional (3D) features from the two-dimensional (2D) TEM images is a nontrivial task and loss of information is unavoidable. Additionally, analysis of particle size from the micrographs is an operator-dependent task and therefore obtained results include user subjectivity.

4 Particle-size dispersion

Regardless of the actual particle-size distribution, a direct fitting for the entire TiRe-LII signal trace yields a mono-disperse equivalent mean particle-size that is known to be biased towards larger sizes for poly-disperse ensembles [62]. By assuming a size distribution, information about the different particle-size groups (the shape of a size distribution and its mean value) can be gained from a two-parameter fit of TiRe-LII [24]. Lehre et al. [25] applied an implicit scheme to solve for the size distribution of a poly-disperse aerosol using a multidimensional non-linear regression. Liu et al. [27] describe an approach that transforms the multivariate minimization problem into a univariate minimization problem by also using a size distribution assumption. Lognormal size distributions are good approximations for soot formed under various flame conditions and are widely assumed for data evaluation [14,27,29,56]. Nevertheless, it is generally challenging to fit poly-disperse distributions to LII signal-decays because the fitting problem is ill-posed [28,62]. Particle-size distributions with various combinations of count median diameter d_{cmd} and geometric width σ_g might produce identical simulated LII signal decay profiles and therefore the evaluation of measured data does not always lead to unique solutions. Also, a lognormal size distribution may not always be the best assumption. It is reported that multi-lognormal [30] or bimodal distributions [98,112] may show better agreement for some specific environments. Dankers et al. [31] showed a rather simple engineering approach that determines d_{cmd} and σ_g from exponential fits to the LII signal decay at two different delay times and within predetermined time intervals. Nevertheless, this method is also based on pre-assumed lognormal distributions.

The new method presented in this work, TERF, shows similarity to Dankers et al. [31] as it also uses a simple exponential fit for a delayed part of the LII-signal trace. In TERF approach, however, it is not necessary to make assumptions about the shape of the particle-size distribution. The TERF method differentiates between signal contributions from small and large particles. It determines mono-disperse equivalent mean particle-sizes for both size groups and evaluates the relative ratio of particle number densities for both groups.

4.1 Poly-dispersity

The TiRe-LII signal acquired from poly-disperse soot is the superposition of individual decaying functions for the various size classes weighted by their respective probability *df*. For a lognormal distribution, *df* of a particle-size class between d_p and $d_p + dd_p$ is

$$df = \frac{1}{\sqrt{2\pi}\, d_\mathrm{p} \ln\sigma_\mathrm{g}} \exp\left[-\frac{\left(\ln d_\mathrm{p} - \ln d_\mathrm{cmd}\right)^2}{2\left(\ln\sigma_\mathrm{g}\right)^2}\right] dd_\mathrm{p} \qquad (13)$$

The distribution is characterized by the count median diameter d_{cmd} and the geometric width deviation σ_g. The geometric width is a multiplicative factor, and thus is dimensionless, rather than having the same dimension as the input values. The distribution is not symmetric but has a long tail towards larger particles. Some examples for different values of the d_{cmd} and σ_g. are shown in Fig. 11.

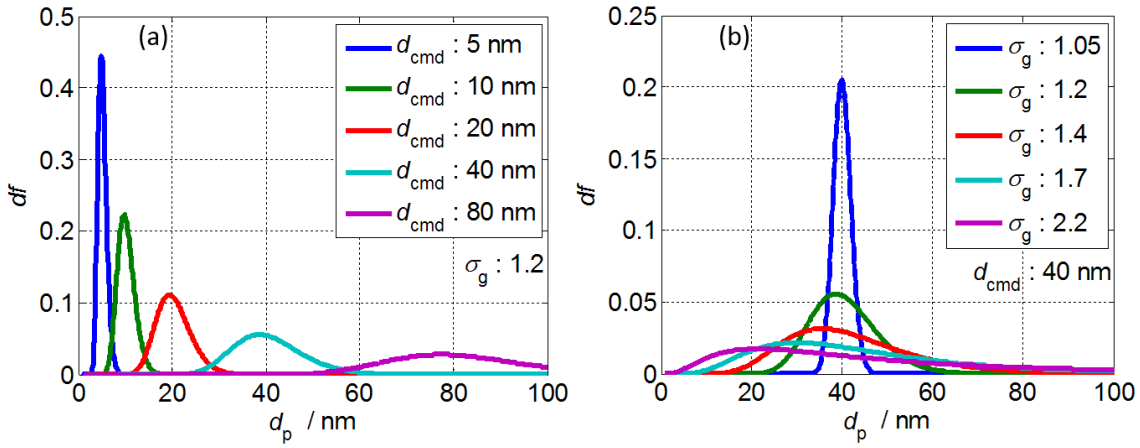

Fig. 11 Lognormal distribution for a fixed geometric width of 1.2 with different d_{cmd} (a) and a fixed d_{cmd} and different σ_g (b).

Evaluating the particle size from such a signal with a mono-disperse assumption yields a mono-disperse equivalent mean particle-size that is biased towards larger sizes. The magnitude of this bias is related to the width (i.e., σ_g) of the distribution. To quantify the bias, a set of LII signals was simulated with a poly-disperse (lognormal) particle ensembles for d_{cmd} varying from 10 to 50 nm in 1 nm increments and σ_g varying from 1.1 to 1.8 in 0.02 increments. To ensure that each signal trace covers the entire process from reaching the peak temperature back to thermal equilibrium with the bathgas, the duration of each simulation was set to 2 µs. Input parameters are given in Tab. 2. For each case, the signal was then evaluated using a mono-disperse approach.

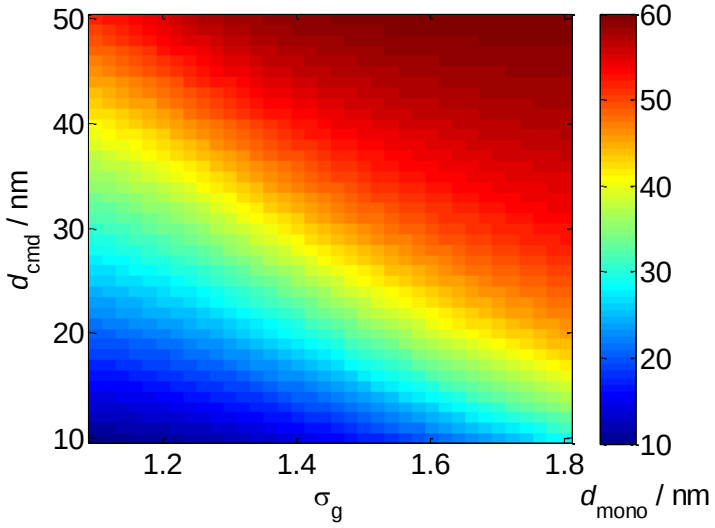

Fig. 12: Mono-disperse particle-sizes evaluated from synthetic LII signals simulated for lognormal particle-size distributions with various values of d_{cmd} and σ_g.

The results for the mono-disperse response to the poly-disperse input are shown in Fig. 12. The determination of the particle-size distribution using an inverse approach is an ill-posed problem. To better illustrate this, six TiRe-LII signal traces with the same mono-disperse equivalent mean particle-size of 40.2 nm (same color code in Fig. 12) but differing values of d_{cmd} and σ_g are selected. The almost identical LII-signal traces are plotted on Fig. 13a. Fig. 13b shows the strongly varying underlying particle-size distributions with the respective color code (each data point on the distribution curve represents the probability density of a 1 nm wide bin).

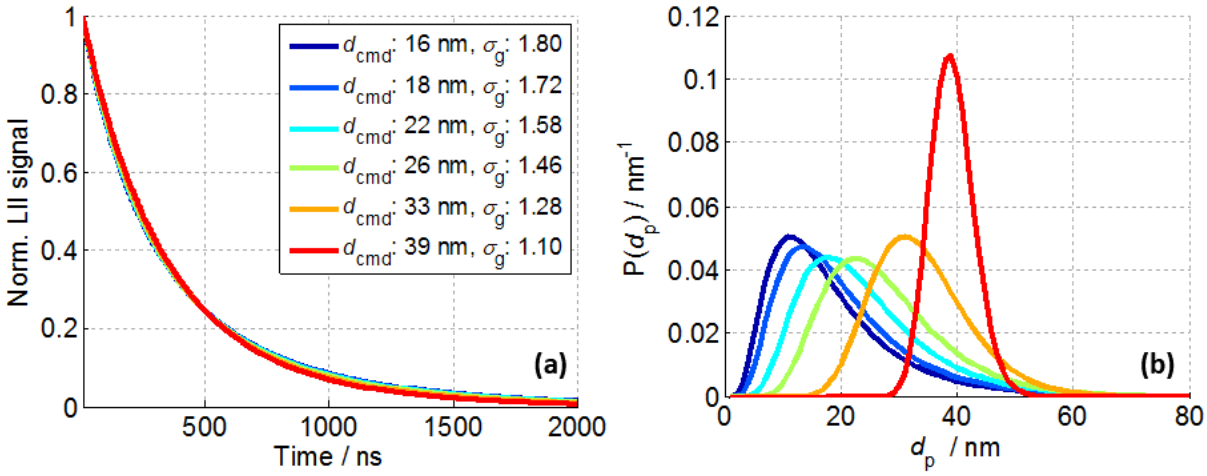

Fig. 13: (a) TiRe-LII signals simulated for soot ensembles with the particle-size distributions shown in (b).

This comparison makes clear that signal interpretation based on standard inversion schemes suffers from this ambiguity with a fairly wide range of satisfactory solutions. To overcome this problem, various approaches were proposed and Daun et al. [28] reviewed various implicit solution schemes for

recovering particle-size distributions from TiRe-LII data. It is shown that such implicit solution approaches suffer loss of accuracy when the input data is slightly modified or when the noise contribution to the measured signal is considerable. Furthermore, approaches that aim at solving the forward problem are time intensive, thus they are not suitable for on-line analysis.

4.2 Simple exponential approximation

In the absence of strong evaporation, heat conduction is the dominant cooling mechanism of soot particles after laser heating. During this cooling, the decay rate remains almost unchanged for an isolated particle or a soot aggregate composed from mono-disperse particles, and therefore the LII signal can be approximated by a simple exponential decay. Liu et al. [90] showed histories of the particle temperature of mono-disperse soot ensembles (with various mean particle sizes) in log scales. The conditions for simulating the LII signal were set for a moderate laser fluence and non-premixed atmospheric flame conditions. For all mean particle sizes, the results exhibit a nearly linear decay (in log scale), i.e., the signal decays almost exponentially. A simple exponential decay is defined by the following equation:

$$y = k\, e^{-t/\tau} \qquad (14)$$

where k is the pre-exponential factor, t is the time and τ is the lifetime of the LII signal of the respective size group. To verify the accuracy of this approximation, a “control LII signal” is simulated for the input parameters shown in Tab. 2 that is later on used as a reference case for comparison with simulated signals with varying input parameters.

Tab. 2: Input parameters for modeling the standard “control signal”.

Property	Standard condition
Particle-size distribution	mono-disperse
Particle size	30 nm
Aggregate size	50
Ambient pressure	1 bar
Bathgas temperature	1750 K
Maximum heat-up temperature	3300 K
Thermal accommodation coefficient	0.25
Soot absorption function $E(m)$	0.4
Detection spectral range	410–440 nm

An exponential function is fitted to this control signal with a least-squares minimization routine for the time range where the LII signal intensity decays to 5% of its peak value. Both curves are shown in Fig. 14.

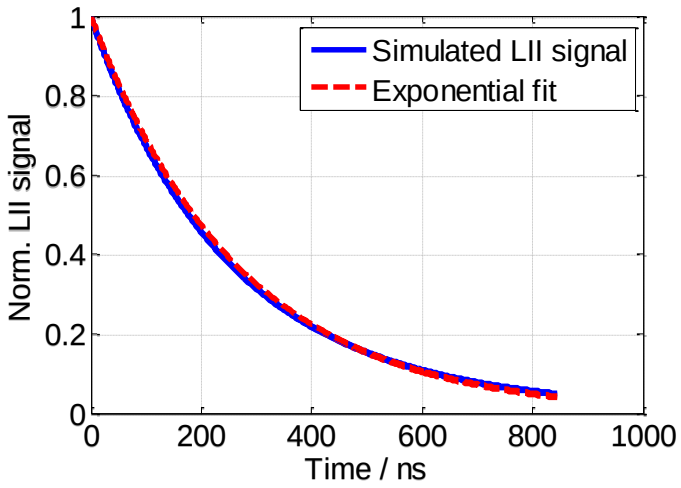

Fig. 14: Simulated LII signal for a mono-disperse aggregate (conditions cf. Tab. 1) and a mono-exponential fit.

The goodness of the fit R^2 is over 0.9994. To quantify the systematic error in particle sizing due to such an approximation, LII-signal curve-fitting is performed by using the new exponential fit (red dashed curve) and the identical input parameters of the control LII signal as model input. This fitting yielded a particle size of 30.6 nm which is only 2% larger than the original input. This minor deviation results from the small contributions of radiation and evaporation to the total cooling. Each of these heat exchange mechanisms contributes its own independent exponential decay rate leading to a deviation from the mono-exponential decay. Because of the low heat-up temperature in the control case, the difference, however, is negligible.

For the validity of the mono-exponential approximation, the experimental conditions (i.e., input parameters of the simulation) are important as they influence the relative importance of the various heat-exchange mechanisms. To quantify this influence, the same procedure is repeated by systematically changing one individual input parameter (keeping all others fixed), and the resulting systematic errors (i.e., the difference caused by the exponential approximation relative to the input data) are shown in Fig. 15 for varying pressure, particle size, aggregate size, and heat-up temperature. Unless otherwise stated, each simulation is performed with the conditions shown in Tab. 2.

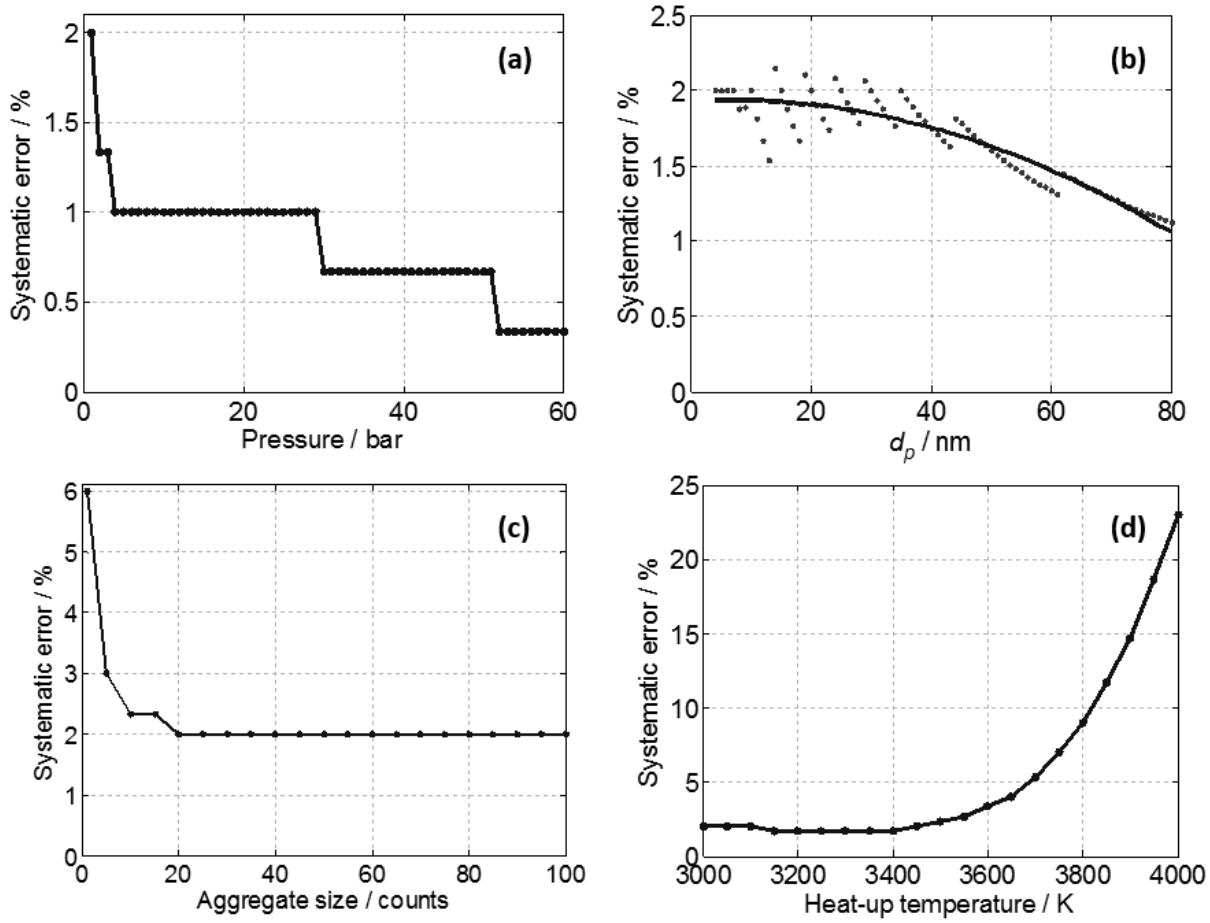

Fig. 15: Systematic errors in particle sizing due to approximating a simulated LII decay with a mono-exponential decay for varying pressure (a), particle size (b), aggregate size (c), and heat-up temperature (d).

In many practical combustion devices soot is formed at elevated pressure. At high pressure, the LII-signal lifetime is significantly reduced due to enhanced heat transfer caused by increased collision rates. In comparison, pressure has a negligible effect on the evaporation rate and radiation is not affected at all. Therefore, with increasing pressure, the importance of conduction in the total heat exchange further increases and the LII signal converges to a simple exponential decay. Fig. 15a shows this effect for pressures from 1 to 60 bar in 1 bar increments. The systematic error further reduces

from 2% at 1 bar to below 0.5% at high pressures. The particle sizing routine of LIISim has a resolution of 0.1 nm. Therefore, the evaluated systematic error shows distinct steps as a function of pressure.

The systematic error evaluated for particles from 4 to 80 nm with 1 nm increments is shown in Fig. 4b (4 nm is the minimum input value for LIISim). The actual data is shown with black dots and the curve is a second-order polynomial fit to illustrate the trend. The oscillation of the data is caused by the 0.1 nm resolution of LIISim. Theoretically, no dependence on the error on particle size is expected because all the heat exchange mechanisms are affected equally. Nevertheless, a slight 1% change in the systematic error is observed over the given particle-size range (systematic error starts to reduce after around 40 nm). This is, however, a result of the data format of LIISim. By default, LIISim uses the first microsecond of the data only for fitting. When the particle size increases from 4 to 80 nm, the LII-signal lifetime increases from ~30 ns to ~2 µs (it exceeds 1 µs at around 40 nm). With large particles, a part of the signal trace is thus disregarded. Such a partial using of the LII signal results in a better fitting by a simple exponential function. Therefore, for particles larger than 40 nm smaller systematic errors are observed. If the curve-fitting routine was not limited in time, no particle-diameter dependence would occur.

Soot aggregates can be described as random fractal structures. In LII modeling, the evaporation rate, the change in internal energy and the heat loss due to radiation are not affected by aggregation as long as the individual particles remain in the Rayleigh regime. The signal scales linearly with the number of primary particles within an aggregate and hence the mass [68]. However, heat conduction is affected by aggregation. A primary soot particle within an aggregate cools down more slowly than an isolated one because of shielding by the surrounding particles [8]. Fig. 15c shows the systematic error for an isolated particle and aggregates with 5 to 100 particles. With increasing aggregate size, the contribution of heat conduction to the total cooling decreases which leads to the assumption of an increasing deviation from a mono-exponential decay. Surprisingly, the results show the opposite trend. The greatest change occurs when switching from isolated particles to the aggregate model. For aggregates larger than 20 particles the magnitude of the change is below the resolution of LIISim. This contradiction requires further investigation and might indicate an incorrect treatment of shielding effects in the underlying submodel in LIISim.

The particle heat-up temperature reached during the laser pulse depends on laser fluence. A change of this parameter influences the heat exchange rates of radiation, conduction, and evaporation. The most critical change occurs with evaporation when the temperature exceeds approx. 3400 K (Fig. 15d). Its contribution to the total cooling increases significantly which causes a strong deviation from the simple exponential decay.

All these analyses indicate that, compared to other uncertainties in LII particle sizing [18], the error due to the mono-exponential approximation is minor for mono-disperse particle ensembles heated in the low-fluence regime. Deviating from the low-fluence regime, however, causes a strong deviation from the mono-exponential assumption. Increasing pressure in contrast is beneficial. Hence, to benefit from the simplicity of fitting exponential functions, this approximation can be used as a tool for further detailed size-distribution analysis.

4.3 Size-distribution analysis with the TERF method

In poly-disperse particle ensembles where each size group has a unique LII-signal lifetime, the signal superposition causes a deviation from the mono-exponential decay behavior. The relative contribution of each size group is linearly proportional to its relative volume fraction f_v. Hence, such a LII signal cannot be accurately approximated by mono-exponential decay. Nevertheless, with increasing time after the laser heat-up, the particle temperature depends on size. Because smaller particles cool faster than larger ones, their contribution to the overall LII signal decreases over time and the remaining signal becomes increasingly dominated by the larger particles [14].

The TERF method couples the fact that the LII signal is dominated by large particles at long delay times and the mono-exponential approximation to derive information about the particle-size distribution. When starting the signal evaluation after a certain delay after laser heat-up, the remaining signal trace preferentially represents the largest particles. Although this signal still contains contributions from particles with various particle sizes, the relative size distribution is narrowing with increasing delay. For such narrow distributions, it has been shown [31,62] that particle sizing via a mono-disperse fitting yields a good approximation for the mean particle-size. Therefore, mono-exponential fitting eventually becomes possible with an acceptable uncertainty that represents the large particles in the ensemble. Once the parameters of the mono-exponential fit are determined, the respective signal contribution of the subsection of the particle ensemble can be extrapolated back in time into the time domain before the above-mentioned delay and into the data disregarded before. This extrapolated curve represents the theoretical cooling of the large particle fraction right after the laser pulse and has a slower decay rate than the overall signal. The additional signal (the difference between the measured signal and the back-extrapolated signal) then stems from smaller particles.

To illustrate this approach, a LII-signal trace is simulated with a wide lognormal distribution (d_{cmd} = 20 nm, σ_{g} = 1.8, black curve in Fig. 16a). All the other parameters are those from Tab. 2. The delay time for starting the data evaluation is 300 ns (dash-dotted grey vertical line) and a mono-exponential function is fitted to the delayed signal portion that is then extrapolated back to the 0–300 ns time

range (dashed red line). The original LII signal has a steeper decay than that of the back-extrapolated fit and it is stronger because of the additional contribution of signal from small particles (shown by the blue dotted curve). The comparison of the normalized curves (Fig. 16b) shows the difference in decay times and thus the origin from different sub-sections of the particle-size ensemble. It should be noted that the signal representing the small particle class (blue dotted line) is also composed of contributions from various particle sizes, however the distribution is again narrower than that of the total ensemble.

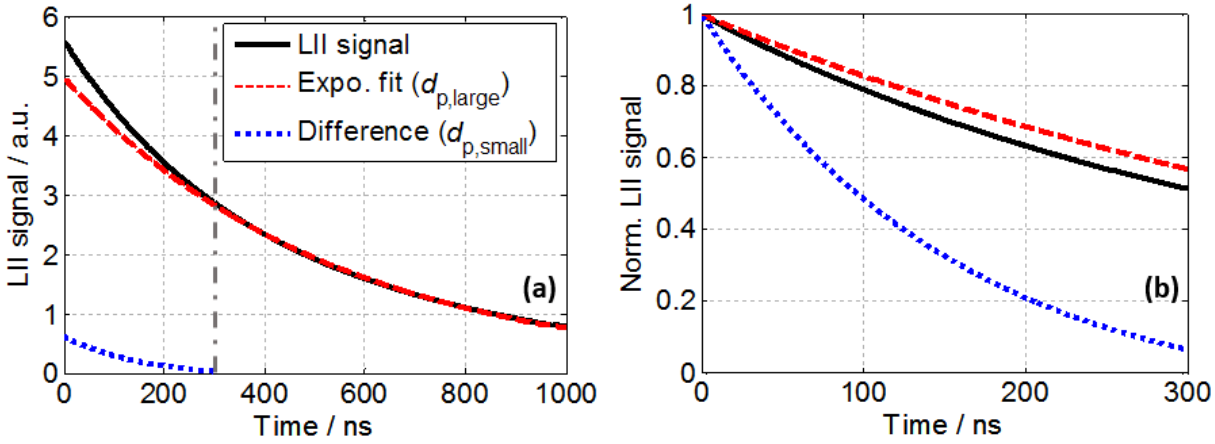

Fig. 16: (a) Simulated LII signal for poly-disperse soot with a lognormal distribution (d_{cmd} = 20 nm, σ_g = 1.8, black solid line). A mono-exponential decay is fitted to the section of the LII signal from 300 ns down to 5% of the peak signal and extrapolated back into the time domain from 0 to 300 ns (red dashed line). The difference between both curves represents the signal contribution from small particles (blue dotted line). (b) The same data normalized to the respective peak values.

A mono-disperse equivalent particle-size can be evaluated from each of these LII signals representing small and large particles, respectively. The evaluation of the time-delayed data requires the knowledge of the actual temperature of the particles at that delay as heat-up temperature for the LIISim simulation. When calculating the extrapolated exponential curve starting at 0 ns, the original heat-up temperature can be used and a temporally-resolved temperature information is not necessary. In Fig. 17, the evaluated small and large mono-disperse equivalent particle-sizes, $d_{p,small}$ = 15 nm and $d_{p,large}$ = 57 nm, are shown along with the actual distribution of the particle size used for the simulation (each data point on the distribution curve represents the probability density of a 1 nm wide bin). These particle sizes represent a mean of different size classes at the two ends of the distribution curve. When particle sizing is performed with the entire LII signal (from peak signal to 5% of this peak) using a mono-disperse approach, the evaluated particle size is 45.3 nm.

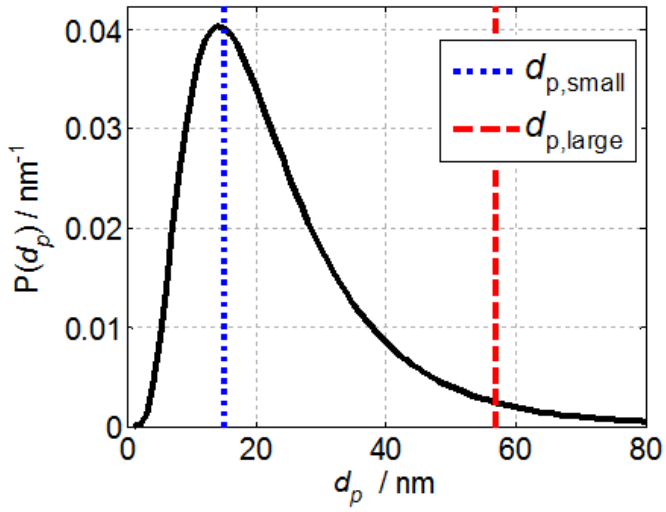

Fig. 17: Lognormal distribution function of particle sizes for d_{cmd} = 20 nm and σ_g = 1.8. The vertical lines show the mono-disperse equivalent particle-sizes evaluated from the exponential decays (see text) representing the small and large particle class of $d_{p,small}$ = 15 nm and $d_{p,large}$ = 57 nm, respectively.

In addition to the mean particle sizes from both size classes, the ratio of their number densities can be evaluated from the pre-exponential intensities with the TERF method. In a mono-disperse soot ensemble, the LII signal is linearly proportional to the soot volume fraction [48] which can be defined in terms of the primary particle diameter, and the average number of primary particles, n_p:

$$f_v = \frac{\pi}{6} n_p d_p^3 \qquad (15)$$

The magnitude of the LII signal at $t = 0$ for the small and large particle-size classes where all particles are at the same temperature (at least for atmospheric or sub-atmospheric pressure, see [44]), is given in Fig. 16a by the ratio of the LII signal intensities, $S_{LII}(0)$ at the time of the laser pulse (t = 0 s):

$$\frac{S_{LII,small}}{S_{LII,large}} = \frac{n_{p,small}}{n_{p,large}} \frac{d_{p,small}^3}{d_{p,large}^3} \qquad (16)$$

The ratio of number densities, $n_{p,small}/n_{p,large}$ (denoted with $\mathcal{R}_n$ hereafter) is calculated as 12.9. The actual ratio for the identical $d_{p,small}$ and $d_{p,large}$ is 14.4 over the assumed lognormal distribution curve.

Because the particle-size distribution is a continuous function, the diminishing contribution of the small particles to the overall signal also continuously decreases with time. Therefore, there is not a perfect delay time that can be defined to separate the range of small and large particles. To see the effect of various chosen delay times, this value is changed from 10 to 600 ns in 10 ns increments while determining $d_{p,small}$, $d_{p,large}$, and $\mathcal{R}_n$ (Fig. 18).

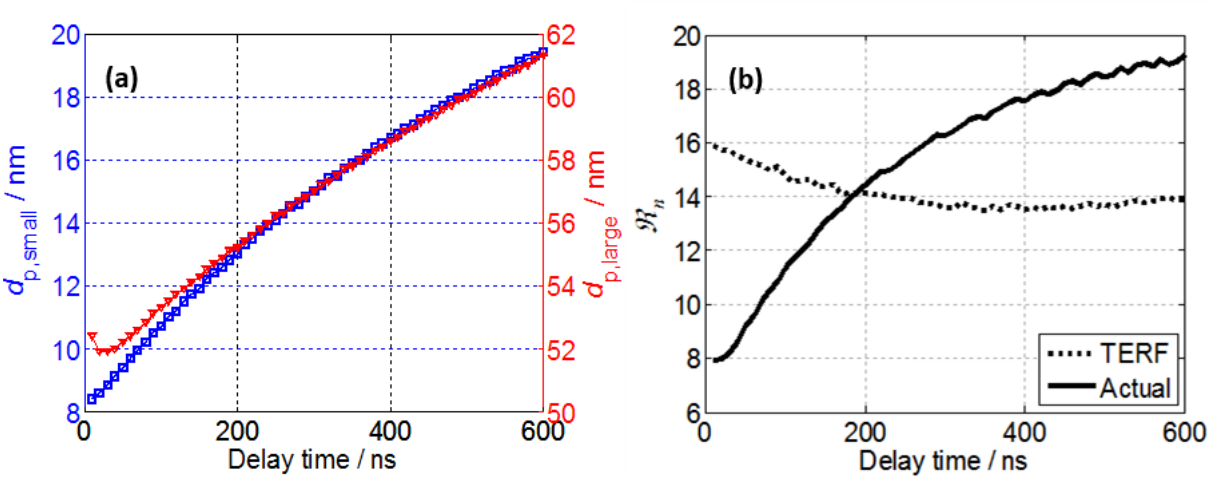

Fig. 18: (a) $d_{p,small}$ and $d_{p,large}$ and (b) ratio of the number densities as a function of the chosen delay time.

As the delay time increases, the contribution of the small particles to the signal segment after the delay gradually decreases, and the lifetime of this signal segment increases resulting in evaluation of larger particles. Similarly, when the delay time increases, the difference curve representing the cooling of the small particles contains a larger contribution from larger particle classes, and consequently the evaluated particle size increases (Fig. 18a). However, an optimum delay time range exists for this strategy. When the delay time is too short, the latter segment used for the exponential fit contains too much information from the different size classes leading to a severe reduction of the fitting accuracy. Likewise, with a too large delay, the weight of larger particles in the difference curve increases and the evaluated $d_{p,small}$ does not represent an accurate mean size for the smallest size classes. The $\mathcal{R}_n$ curves in Fig. 18b also verify this argument: For too early or too late delay times, the predicted results with the TERF method deviate from the actual $\mathcal{R}_n$ that is evaluated from the original distribution. For the present conditions, a delay time at around 200 ns gives a ratio close to the actual distribution. This optimum delay may vary for different distributions (this will be further analyzed in section 4.6.2).

4.4 Evaluation of various particle-size distributions

The strategy described before was tested on poly-disperse soot ensembles with various distribution characteristics. In addition to the wide lognormal distribution introduced in section 4.3, a narrower lognormal distribution and two bimodal distributions with distinctive shapes were analyzed. The bimodal distribution functions, p_{bimodal}, were created from two standard lognormal distributions superimposed with independent weight functions [98]:

$$p_{\mathrm{bimodal}} = w_1 p_1\left(d_{\mathrm{cmd},1}, \sigma_{\mathrm{g},1}\right) + w_2 p_2\left(d_{\mathrm{cmd},2}, \sigma_{\mathrm{g},2}\right) \qquad (17)$$

p_1 and p_2 are the probability density functions with lognormal distributions, whereas w_1 and w_2 are the weight factors for the small-size mode and the large-size mode, respectively. The distribution parameters used in this section are listed in Tab. 3.

Tab. 3: Parameters of the investigated particle-size distributions.

Parameters	**a**	**b**	**c**
Distribution	lognormal	bimodal	bimodal
$d_{\mathrm{cmd},1}$ / nm	15	15	15
$\sigma_{\mathrm{g},1}$	1.5	1.4	2
w_1	1	3	1
$d_{\mathrm{cmd},2}$ / nm	-	40	30
$\sigma_{\mathrm{g},2}$	-	1.3	1.5
w_2	-	1	1

The distribution functions are shown in Fig. 19 (each data point on the distribution curves represents the probability density of a 1 nm-wide bin) along with the evaluated small and large mono-disperse equivalent mean particle-sizes (vertical lines). For all the three cases, the delay time was 220 ns. The actual $\mathcal{R}_n$ calculated from the distribution function (ratio of $P(d_\mathrm{p})$ at $d_{\mathrm{p,small}}$ and $d_{\mathrm{p,large}}$) and the $\mathcal{R}_n$ calculated with the TERF method are given on the respective plots. In all three cases the evaluated $d_{\mathrm{p,small}}$ and $d_{\mathrm{p,large}}$ fall within the distribution and represent a mean particle-size within their size classes. The $\mathcal{R}_n$ values evaluated with the TERF method also show good agreement with the actual $\mathcal{R}_n$ derived from the probability density functions at $d_{\mathrm{p,small}}$ and $d_{\mathrm{p,large}}$.

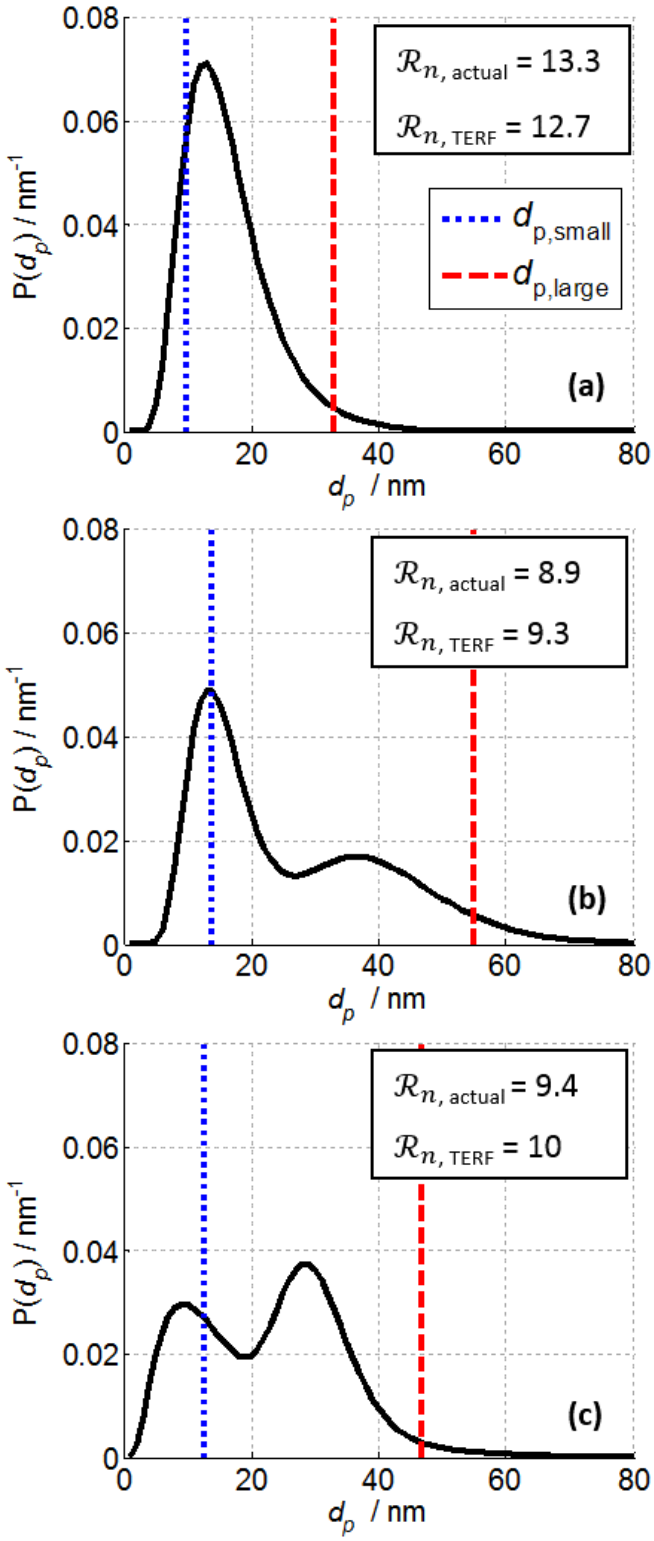

Fig. 19: Probability density functions for lognormal (a) and bimodal (b, c) distributions. Vertical lines show the mono-disperse equivalent s evaluated for the small and large particle classes.

4.5 Experiment

Particle-size measurements were performed in a non-premixed ethylene/air Santoro flame [102] operated under standard conditions (C_2H_4: 0.232 standard liters per minute (slm), air co-flow: 43 slm). To stabilize the flame, a chimney with a 25 cm diameter was mounted 30 cm above the burner. The schematics of the experiment is shown in Fig. 20. For LII, the fundamental of a Nd:YAG laser at 1064 nm was used with a pulse width of 7 ns. A set of cylindrical lenses forms a horizontal laser sheet, and a 1 mm slit aperture crops the laser sheet into a rectangular shape that is relay-imaged into the center of the flame with a spherical lens at a 2*f* distance creating a nearly top-hat intensity profile. This spatial profile was measured with a beam profiler. The laser fluence was set to 0.08 J/cm^2 which does not cause any considerable soot evaporation. The LII signal was detected with a fast photomultiplier (PMT, Hamamatsu R7400U-04, rise time ~0.78 ns) coupled with a bandpass filter (425±15 or 676±14 nm) and stored on a 1 GHz oscilloscope. The photomultiplier was combined with a system of two spherical lenses and a circular aperture to provide high spatial resolution. This collection volume (circular probe zone) in the flame has a diameter of 1.5 mm and it was located at a 2 mm distance to the burner axis on the pump laser entrance side. This radial location has a higher soot mass with respect to the burner axis location, thus better signal-to-noise ratios can be achieved. The burner and the chimney were mounted on a vertical translation stage independent from the optical path, which enables different heights in the flame to be probed.

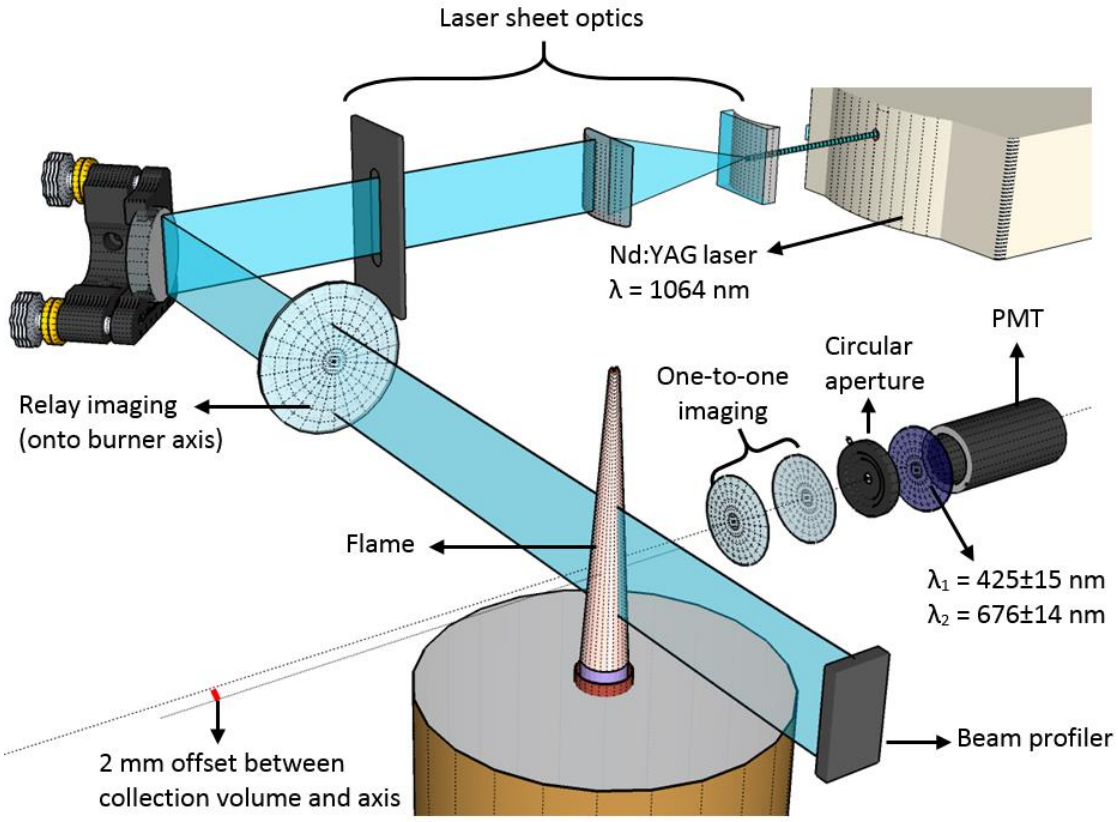

Fig. 20: Experimental arrangement

The measured LII decay curves were recorded at heights between 30–70 mm above the burner (HAB) in steps of 5 mm. At each location 100 single measurements were recorded with each of the two bandpass filters. Prior to the LII measurements, the detection system was spectrally calibrated by replacing the burner with a broad-band halogen lamp with known irradiance.

For *ex situ* characterization, thermophoretic sampling was achieved at five HAB positions using a pneumatically-driven soot sampling probe on which lacey carbon-coated copper grids were attached. Grids were purchased from Tedpella (Product No: 01895) [111]. The probe consisted of two thin metallic plates in a sandwich form, with a 3-mm-diameter hole exposing both sides of the TEM grid to the flame (a similar design is shown in ref. [109]). The purpose of using a lacey grid was to minimize the distortion of the electron beam by the carbon film during the microscope imaging. A high-frame-rate camera (1000 fps) positioned perpendicular to the pneumatic cylinder axis was mounted to measure the probe trajectory and the timing precisely. The exposure time of the probe to the flame environment (time duration where the grid rests within the flame) was set to 40 ms whereas the transit time (where the grid moves within the flame boundary) was shorter than 3 ms. Additional samples were collected with 60 and 80 ms exposure times at 50 mm HAB to analyze the effect of exposure time on soot sampling. The radial distance of the grid center was 2 mm from the burner axis. The

sampled soot was analyzed with a Tecnai FEG 200 kV transmission electron microscope and images were recorded at 26000× magnification and micrographs were manually analyzed using the freeware ImageJ. It should be noted that the TEM analysis of grids in this work were conducted by a third party TEM operator who had no extensive experience in soot research. The operator acquired ~40 images from each grid, and it is lately understood that in each of these images large aggregates were targeted and all the possible isolated particles and small aggregates were omitted. Therefore, the TEM-derived results in this work do not represent the entire soot ensemble in the respective sampling location.

4.6 Results and discussion

4.6.1 Input parameters

At each probe volume along the flame, the ambient conditions must be known for accurately modeling the LII heating and cooling processes that may vary due to radiative cooling, changing mixture fraction, and changing soot morphology. In this study, the heat-up temperature of the laser-heated soot particles was derived via pyrometry from the ratio of peak LII signal intensities within two detection bands by using a lookup table method [64]. These spectral bands (425±15 and 676±14 nm) were selected according to the recommendation of [65]. The specific emissivity values for each of these spectral bands are calculated with Eq. 4. A variation of the soot absorption function $E(m)$, therefore emissivity, along the flame height was not considered in this work and identical values were used at all locations. To suppress the influence of background signal, i.e., line-of-sight integrated flame luminosity, the baseline signal before the laser pulse was subtracted at each location. To measure the effective bathgas temperature, the measurements were repeated at HAB 60 mm without the laser pulse. At around this height the radial temperature gradients are minimal and the temperature is radially uniform [103], thus a biasing towards lower temperatures due to edge effects was negligible. Through subtracting the the bathgas temperature from the heat-up temperature, the temperature increase due to the laser light absorption was calculated as 1650 K at this height. By assuming a constant soot absorption function $E(m)$ at all flame heights, the temperature increase was also assumed constant at all locations, and the bathgas temperatures were calculated for the flame heights, respectively. The flame- and heat-up temperatures used for simulating LII signals are shown in Tab. 4.

Tab. 4: Heat-up temperature, bathgas temperature, and aggregate size input parameters imposed for particle sizing at different heights above burner (HAB).

HAB / nm	$T_{heat\text{-}up}$ / K	T_{gas} / K	N_p
30	3414	1764	40
35	3390	1740	50
40	3351	1701	60
45	3271	1621	70
50	3259	1609	80
55	3282	1632	90
60	3225	1575	80
65	3235	1585	70
70	3162	1512	60

At the investigated radial location bathgas temperatures decrease with increasing HAB due to the cooling of the flame via radiation and convection (at another radial position different trends might occur depending on air entrainment). Aggregate sizes also change with flame height [62] and the values shown in Tab. 4 are estimations based on TEM analysis. The other input parameters used at each location are shown in Tab. 2. With a rough estimation, the precision of the heat-up temperature measurement via two-color pyrometry can be taken as ±100 K, the bathgas temperature ±200 K and the aggregate size ±40 particles. The influence of these uncertainties on the evaluated particle size is shown in Fig. 21. The total uncertainty of the evaluated particle size due to these input parameters is approximately ±20%.

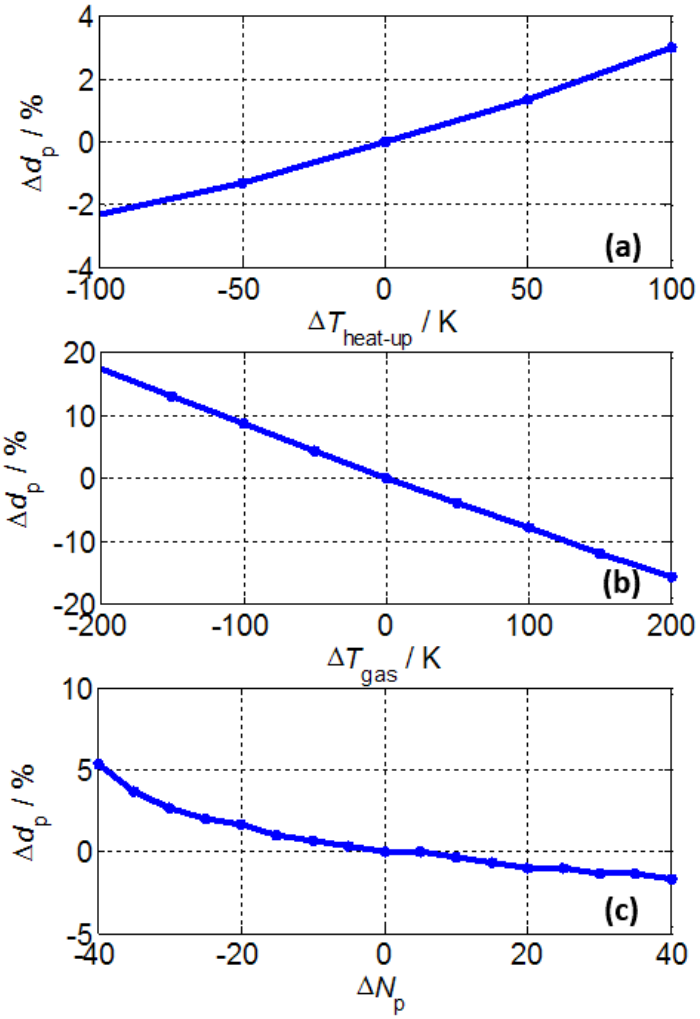

Fig. 21: Uncertainties of the particle-size determination from the TiRe-LII signal traces due to variations in the underlying heat-up temperature (a), bathgas temperature (b), and aggregate size (c) compared to Tab. 2 conditions.

For this analysis, a control LII signal for Tab. 2 conditions is generated. Subsequently, this simulated signal trace is fitted by the LII model by systematically changing the assumed values for the relevant input parameters within a given range (one by one). The differences between the evaluated sizes and the initial particle size for the control signal shows the sensitivity of the particle-size determination on the respective parameters.

4.6.2 Particle sizing

Particle sizes were determined from the LII-signal traces acquired at 425±15 nm. The TERF method introduced in section 4.3 was applied for each signal trace. Additionally the mono-disperse equivalent mean particle-sizes were evaluated by full signal fitting. To investigate the influence of the delay time with the TERF method, it was swept from 20 to 800 ns in 20 ns increments and at each delay $d_{p,small}$

and $d_{p,large}$ were calculated (Fig. 22). Similar to the model-based analysis results, $d_{p,small}$ and $d_{p,large}$ increases with increasing delay time due to the increasing contribution of larger particles in the respective input signal segments.

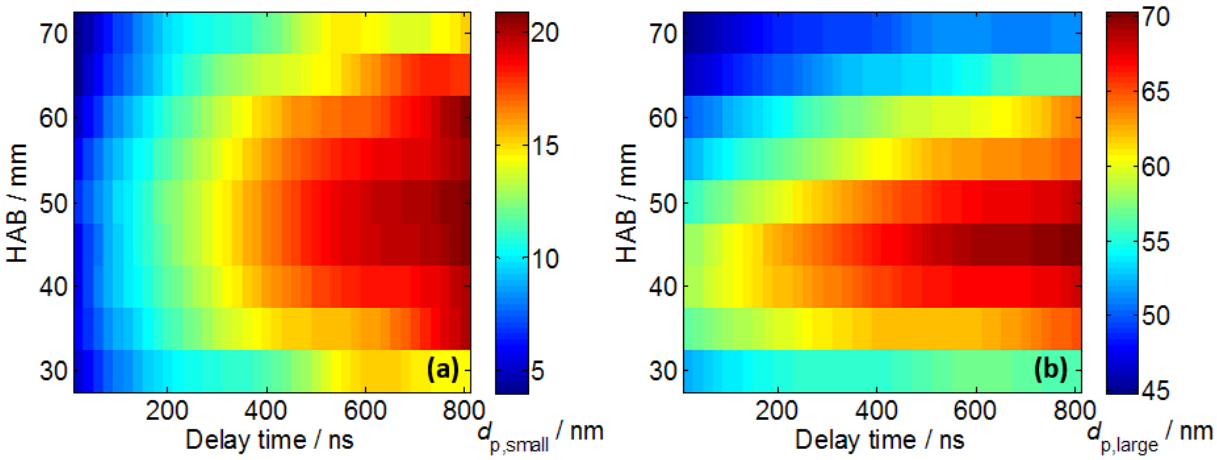

Fig. 22: (a) $d_{p,small}$ and (b) $d_{p,large}$ at different delay times evaluated for nine HAB positions.

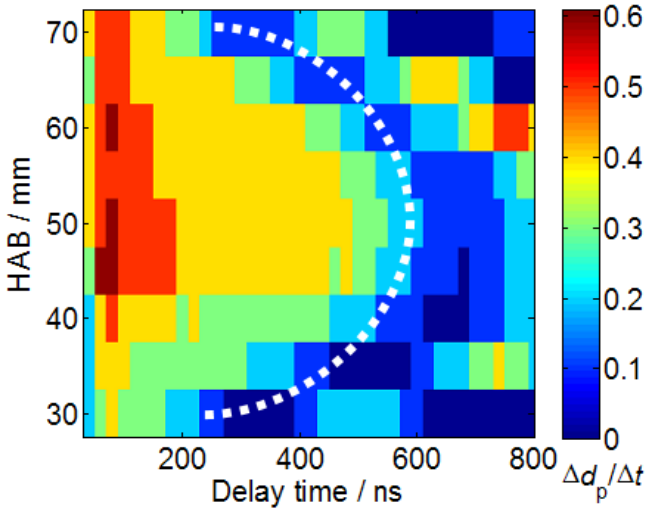

Fig. 23: Derivative of the particle sizes at each HAB with respect to changing delay time.

As described in section 4.3, the optimum delay time for each signal depends on the actual particle-size distribution. In an ideal case the evaluated particle-size should be least sensitive to changing delay time at around its optimum as it ensures that information blending from different particle-size classes is minimal. To define these optimum points, a derivative of the particle sizes (large mode) at each HAB was taken with respect to the changing delay time as shown in Fig. 23. The strong oscillations in the derivative results (for fixed HAB) were filtered out with a median filter. The optimum delay time is defined as the point where $\Delta d_p/\Delta t$ first approaches 0.1 nm/ns and is marked with a white dashed

line (parabola). The optimum delay time is as low as 240 ns at zones where particles are relatively small and reaches values above 600 ns at flame locations where the largest particle diameters are expected. Any increase in $\Delta d_p/\Delta t$ after this optimum delay can be attributed to noise in the acquired data.

By using these optimum delay times, $\mathcal{R}_n$ at each HAB is calculated and shown in Fig. 24 with the respective $d_{p,small}$ and $d_{p,large}$. The mono-disperse equivalent particle-size $d_{p,mono}$ is also shown. For all size classes, the particle diameter increases with the flame height and reaches a maximum at 50 mm HAB for the small mode, and at 45 mm HAB for the large mode and the mono-disperse equivalent size. After these peak points, particle diameters gradually decrease indicating that soot particle-sizes are affected by increasing oxidation. Within the flame height domain between 30 and 70 mm HAB, the deviation in particle size is ~10 nm for the small mode and the mono-disperse equivalent mean size, whereas it is more than 20 nm for the large mode. Fig. 24 also shows that $\mathcal{R}_n$ has an inverse relation with particle sizes. In soot formation and oxidation zones the population of small particles with respect to larger ones is greater and reaches its minimum within the zone where the largest particle diameters are evaluated (soot oxidation and soot formation are in balance). This trend of $\mathcal{R}_n$ is directly related to different rates of changes in particle-size classes. The relative difference of $d_{p,small}$ and $d_{p,large}$ with respect to $d_{p,mono}$ at each flame height shows that the small particles are generally much smaller than the mean particle-size in the formation and oxidation zones. This gap reaches its minimum around in the zone where formation and oxidation is balanced whereas the difference between large particles and mean particle-size reach its maximum in the zone.

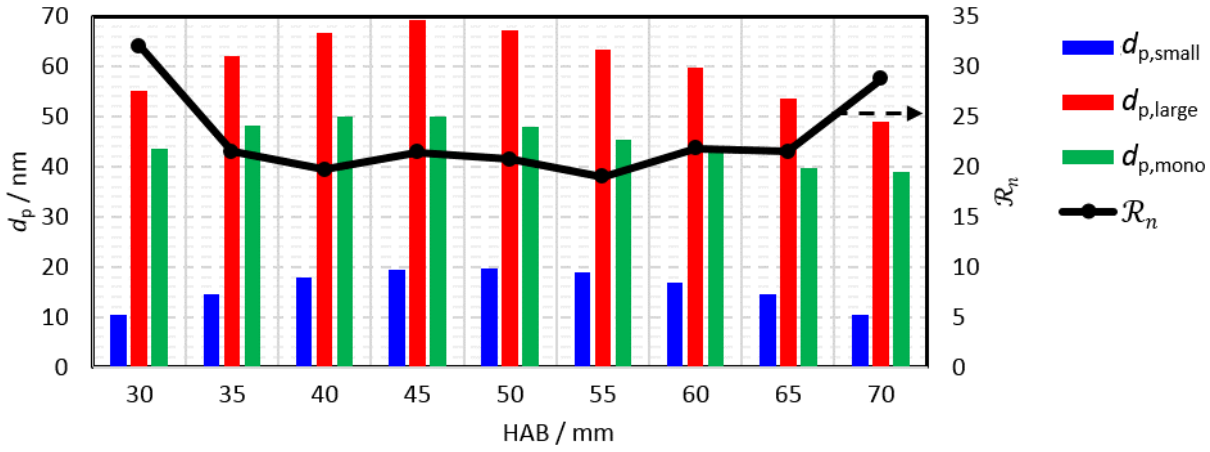

Fig. 24: $d_{p,small}$, $d_{p,large}$ and relative ratio of number densities calculated with the respective optimum delays (cf. Fig. 22) as a function of HAB. $d_{p,mono}$ is evaluated with full curve-fitting.

4.6.3 Comparison of LII and TEM particle sizing

The soot particle-size was additionally determined from TEM micrographs acquired at five HAB ranging from 30–70 mm. For each position the obtained primary particle diameters were divided into size bins and represented as a histogram. The histograms were then fitted by lognormal particle-size distributions to obtain continuous distribution functions. A lognormal distribution fits the particle sizes well for all locations (Fig. 25a). The total number of samples N_{TEM} counted as a function of HAB is given in each graph. The $d_{p,small}$ and $d_{p,large}$ values obtained from the TERF-derived LII signal analysis for the same locations are also plotted as blue and red dashed vertical lines, resp. $d_{p,mono}$ values obtained by full curve fitting are shown with green dash-dotted vertical lines. The TEM measurements yielded a similar trend of particle-size change as the LII measurements along the flame height. The mean particle size reaches a maximum at 40 mm HAB and then gradually decreases due to oxidation.

In most of the locations, $d_{p,large}$ obtained by LII falls within the particle-size distribution derived from TEM measurements, particularly within the large particle classes. On the other hand, $d_{p,small}$ is smaller than the smallest particles measured from TEM for all cases. The main reason for this difference is attributed to the strong bias in evaluating TEM images. Usually, the small particles are either isolated or they exist as small aggregates which reduces the probability of their collision to the lacey carbon film used here (cf. Fig. 25b). Furthermore, as mentioned in section 4.5, the TEM operator was prone to capturing large aggregates as they provide more information for the statistical analysis of primary particle-size measurements (on each grid ~40 images were taken) and mostly ignored isolated particles. Structures of soot aggregates can also be problematic for the measurement of small particles. Identifying the smaller particles at the center of an aggregate is hindered due to the relatively larger optical density of large particles that cover the small ones. Additionally, even with a small degree of bridging [113] between small and large particles, it becomes more difficult to perceive the spherical structure of small particles and a diameter cannot be measured successfully. Such bridging of small particles was mostly observed at the periphery of the aggregates and two examples are shown in Fig. 25c. These images also indicate that initially loosely connected small individual particles that give rise to rapidly-cooling LII signal might get fused to the larger particles in the supporting agglomerate during sampling and aging in between sampling and TEM measurements. Therefore, the statistical relevance of the TEM-derived number of particles with small diameters may be biased. All these observations indicate that large numbers of very small particles might be systematically overlooked when investigating TEM images of poly-disperse soot samples.

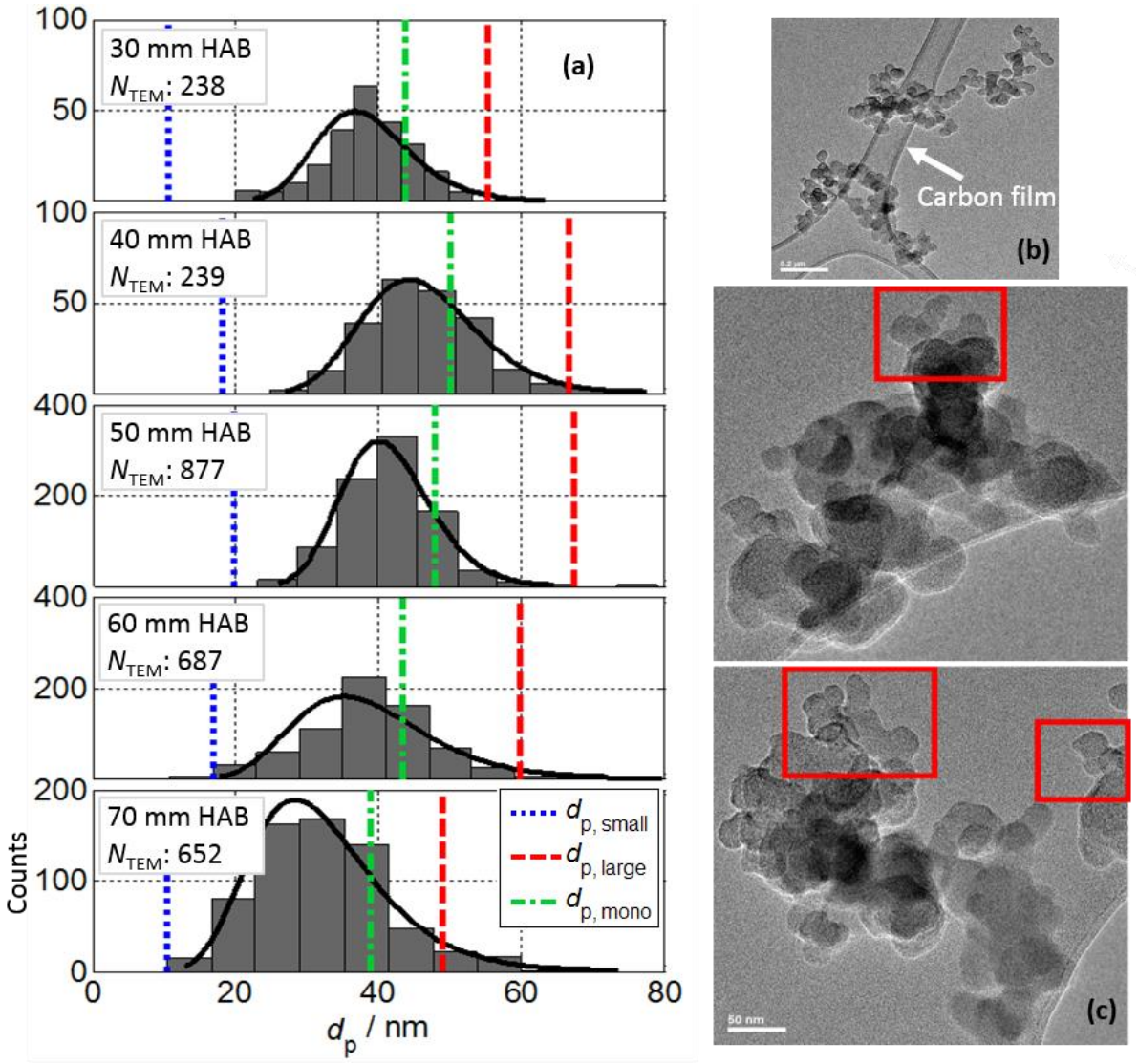

Fig. 25: (a) Classification of primary particle-sizes from TEM (gray bars) with lognormal fits (black lines) obtained from soot at five HAB from 30 to 70 mm. LII TERF-derived $d_{p,small}$ and $d_{p,large}$ values are shown as blue dotted and red dashed vertical lines, resp. $d_{p,mono}$ values are shown with green dash-dotted vertical lines. (b) Soot aggregates on a lacey carbon film. (c) Bridging of small particles with the larger ones at the aggregate periphery. Due to the lost perception of sphericity, a measurement of diameter is not possible for such particles and therefore they are systematically not included in the statistical analysis. Even smaller particles that might have existed on the agglomerate surface might have got fused entirely with the surface layer and therefore remain invisible.

Another reason for the discrepancy may be the unknown thermal accommodation coefficient, α_T. Bladh et al. [62] reported that α_T depends on the soot morphology and also may decrease with increasing soot maturity (i.e., higher up in the flame). In this work, however, a constant α_T was used for all locations and all size groups. If a relatively larger α_T was used for the younger particles, i.e., smaller particles in the formation zone, a more efficient loss of energy to the surrounding atmosphere would

be simulated for these particles. This would eventually lead to a faster signal decay, hence evaluation of relatively larger diameters in the small size classes.

To better understand the discrepancy between the TERF-LII-derived and the TEM-derived small particle-sizes, for each HAB a phantom poly-disperse TiRe-LII signal was simulated with the respective TEM distributions shown in Fig. 25a and input parameters shown in Tab. 4. This means that the resulting phantom signal includes no information for particles smaller than what observed in the TEM. Consecutively, $d_{p,small}$ and $d_{p,large}$ were evaluated with the TERF method. At each HAB, the evaluated $d_{p,small}$ were found to be larger than the values obtained from the experimental data, cf. Fig. 26. This indicates that the discrepancy between *in situ* and *ex situ* measurements is most likely due to the incomplete information derived from TEM.

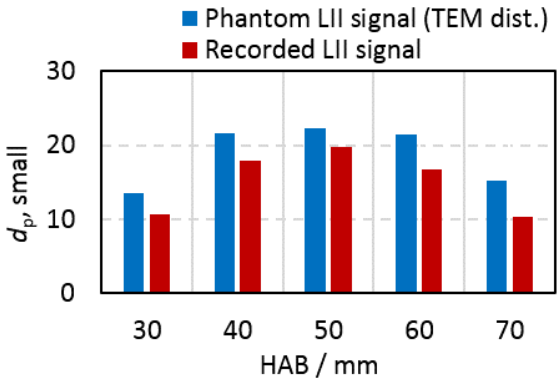

Fig. 26: $d_{p,small}$ calculated with acquired LII signal and phantom poly-disperse TiRe-LII signal simulated with the respective TEM distributions. The larger $d_{p,small}$ evaluated with the phantom signal at each HAB indicates that the TEM may fail to provide correct information about the smallest particles that contribute to the LII signal.

For thermophoretic sampling, various exposure times of the grid varying from 25 to 300 ms were used in the past [62,109,114]. In this study, the effect of varying the exposure time on the TEM particle sizing was investigated by exposing the grid to the flame for 40, 60, and 80 ms. The respective particle-size histograms together with their lognormal fit are compared in Fig. 27. The corresponding d_{cmd} and σ_g values are given in each plot. A systematic decrease in the d_{cmd} and a widening of the distribution is observed with increasing exposure time. The measurements were taken at 50 mm HAB where soot oxidation dominates and deposited soot particles are exposed to excess oxygen and high temperature. Because the soot particles are only loosely attached to the thin lacey carbon coating, cooling from the supporting copper grid is not efficient. During this phase, particles eventually partially oxidize and it cannot be excluded that small particles disappear completely. At the same time, additional particles are continuously deposited until the end of exposure time. Therefore, the width of the particle-size distribution σ_g increases with increasing exposure time and the distribution increasingly deviates from lognormal. This exposure-time dependent particle sizing result is in contrast to the conclusion

drawn in ref. [109]. Nevertheless, the sampling location in that work is not mentioned which can be the reason of the discrepancy. In fuel-rich zones, deposited particles would not oxidize. Instead, the deposited particles would be subjected to co-aggregation with the latter particles. To minimize the effects of sampling on particle sizing, the shortest exposure time should be selected that permits collecting sufficient particles for the TEM imaging.

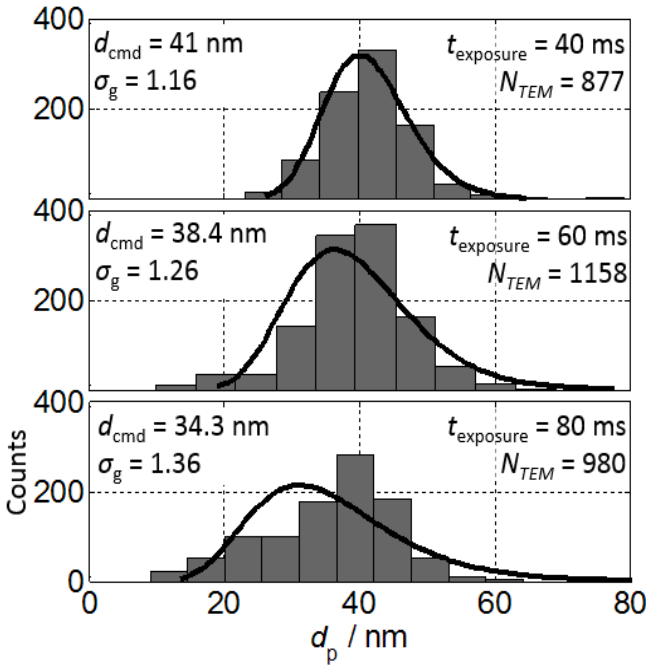

Fig. 27: Histograms of TEM-derived particle-sizes with lognormal fits for soot sampled at 50 mm HAB with varying exposure times.

Perturbations of the flame during sampling can cause additional uncertainty in TEM particle sizing. The high-repetition-rate movies showed that the flow induced by the moving probe severely distorts the flame. This distortion starts shortly after the probe reaches its stationary position and lasts up to 10 ms. The forced flow and the subsequent unsteadiness of the flame may cause deposition of soot on the grid that stems from locations outside the intended probe volume.

4.7 Conclusions

A signal-processing method, TERF, was developed for TiRe-LII in poly-disperse soot that provides information about the size range and the relative weight of the small and the large fraction of the particle ensemble. The method separates the signal contribution of small and large particles from the overall signal by approximating the LII signal from size classes with narrow size distributions with mono-exponential decays. A mono-disperse equivalent mean particle-size is then evaluated for both size classes and the relative ratio of the number densities of both groups is determined. Compared to

time-consuming poly-disperse fitting algorithms, the extracted information is limited. Nevertheless, compared to previous methods it is not necessary to assume the shape of the distribution and the much faster evaluation makes TERF suitable for real-time analysis.

The validity of approximating LII signal traces with mono-exponential decays was analyzed with LII-signal traces simulated for mono-disperse soot for various input parameters such as pressure, aggregate size, and heat-up temperature. Suitable ranges of conditions where the TERF method works reliably were determined and the error imposed by the approximation was found to be less than 2%. High heat-up temperatures that cause strong soot evaporation was found to be the conditions where the method cannot be used. The accuracy of the method was tested on simulated signals with lognormal and bimodal particle-size distributions with various distribution parameters. In all cases the method yielded satisfying results.

The TERF method was applied to measured signal traces acquired with a time-resolved detection setup at nine axial locations in a non-premixed atmospheric laminar ethylene/air flame from a Santoro burner. The LII measurements were supported by two-color pyrometry of particle heat-up temperatures. Low-fluence excitation prevented soot evaporation. A model-based analysis was performed to identify the dependence of LII particle sizing quantitatively on the assumed input parameters such as bathgas temperature, heat-up temperature, and soot morphology. At each location a mono-disperse equivalent mean particle-size was also evaluated and compared to TERF method results.

For *ex situ* characterization, soot particles were sampled at multiple flame heights using a pneumatically-driven soot sampling-probe. Particle-size distributions were derived from TEM measurements and compared to the LII-derived results. It was observed that the TERF method provides sizes for the large particle class that are in good agreement with the TEM measurements. Substantial discrepancies were observed, however, between LII and TEM results for the small mode. The discrepancies were mainly associated to the biased sampling and TEM operations that omits the analysis of small size classes. The effect of varying exposure times of the TEM grid to the flame was analyzed. At a location with excess oxygen, long exposure times cause an increased oxidation of initially deposited soot, thus the measured mean particle-size decreases and the distribution widens.

5 Soot volume fraction

Soot investigations in optically-accessible engines as well as high-temperature, high-pressure combustion vessels have shown that soot formation in reacting fuel jets begins shortly after autoignition [39,115–119] at a finite distance from the initial high-heat-release reactions and then continues throughout the mixing-controlled combustion phase [39,47,117,118]. Investigations indicate that mixing-controlled Diesel combustion for quiescent Diesel engine conditions occurs in a lifted, turbulent non-premixed flame mode. The non-premixed flame takes place at the periphery of the spray. Inside this hollow high-temperature reaction zone, a fuel-rich mixture with relatively lower temperature and slower reaction rate is present. Dec [118] showed these two modes, mixing-controlled and non-premixed flames, in a Diesel combustion with a conceptual model as shown in Fig. 28.

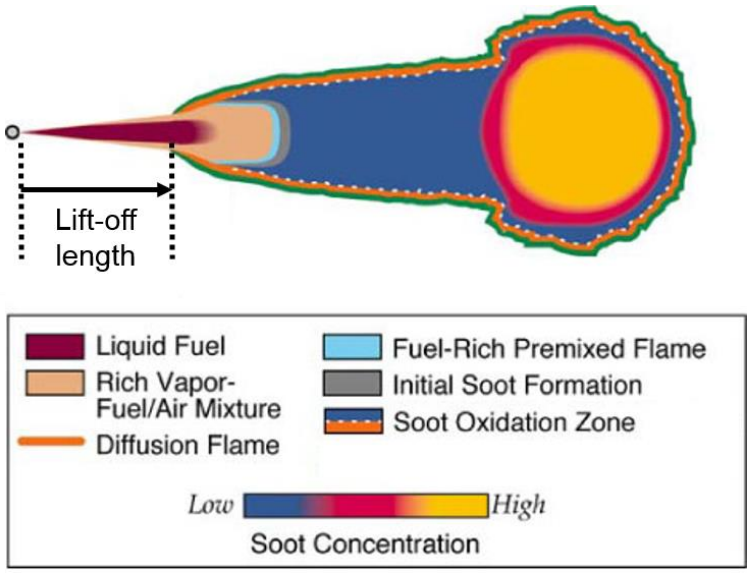

Fig. 28: Conceptual model of a quasi-stationary Diesel combustion plume by Dec [118].

Fuel and air in this core spray zone start to mix upstream of the flame lift-off, hence the position of lift-off is important for the mixture fraction downstream of this zone. For soot processes local availability of oxygen and temperature in the region are two key parameters. Therefore, the flame structure in the premixed phase and the lift-off lengths are crucial for the soot formation process [35,37,39,118].

The ECN has defined target sprays that can be operated in various facilities available in the contributing labs. The target conditions are confirmed by comparing to existing databases including liquid penetration-length, vapor penetration-length, ignition delay and lift-off length measurements

[20,45,120,121]. Well-characterized nominally identical injectors [121] are used in all contributing labs. Target Spray A (Tab. 5) acts as a reference case for low-temperature Diesel combustion in engines with moderate exhaust-gas recirculation (EGR) [45]. Extensive information about measurements on Spray A are given on the ECN website [20].

Tab. 5: Operating conditions for Spray A.

Gas temperature	900 K
Gas pressure	near 6.0 MPa
Gas density	22.8 kg/m^3
Oxygen concentration	15% O_2 reactive and 0% O_2 non-reactive
Gas velocity	Near-quiescent, <1 m/s
Fuel injection pressure	1500 bar
Fuel	n-dodecane
Fuel temperature at nozzle	363 K (90˚C)
Injection duration	1.5 ms
Injection mass	~3.5 mg

This section addresses the measurement of local soot volume fractions in transient and quasi-stationary cases of Spray A. Measurements for the standard operating conditions provide a basis for understanding the ambient and injector boundary conditions, and also provide the basis for interpreting the soot measurement results. Additional measurements with parametric variations (cf. Tab. 6) of the standard conditions permit investigation of the effect of the various operating conditions on the lift-off length and the soot level. For each boundary condition, OH chemiluminescence imaging is used to determine the lift-off length. The differences between nominal and actual gas temperatures mentioned in Tab. 6 will be explained in section 5.6.1.

Tab. 6: Parametric variations of the Spray A operating condition.

Nominal ambient gas temperature (actual)	800 (830), 850 (880), 900 (930), 1000 (1030) K
Oxygen concentration	11, 13, 15, 21% O_2
Injection duration	1.5, 4 ms

5.1 High-pressure high-temperature (HPHT) vessel

To mimic the thermodynamical conditions encountered in a real engine at the injection timing, a pre-combustion type vessel was used in this work. A schematic of the vessel is illustrated in Fig. 29 and its characteristics are listed in Tab. 7.

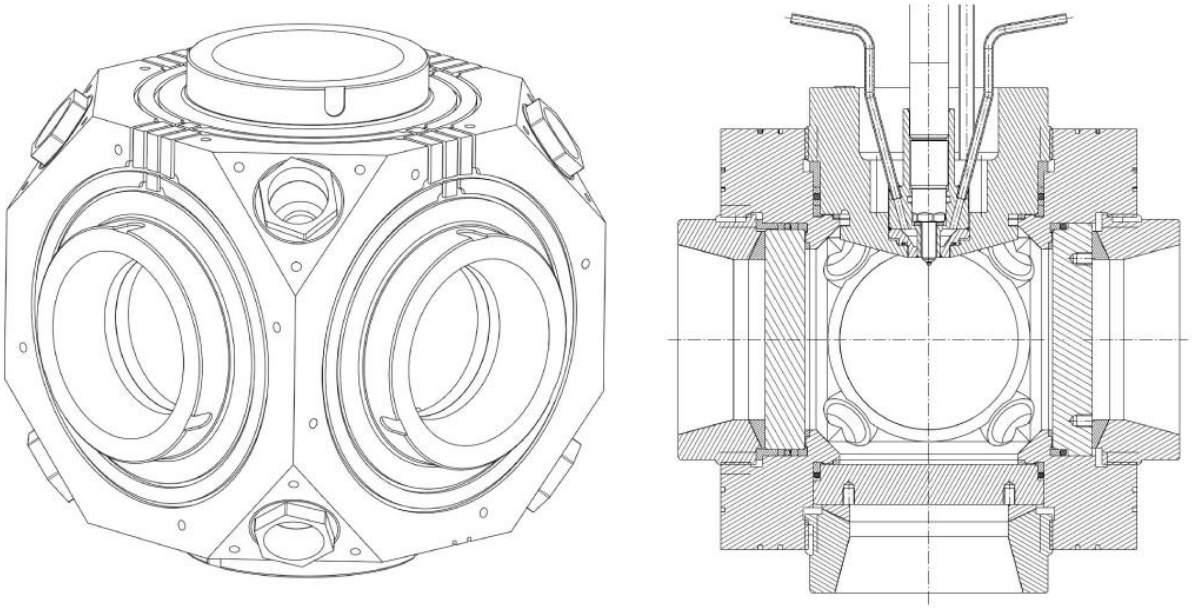

Fig. 29: Global view (left) and sectional drawing (right, with an injector in vertical position) of the IFPEN vessel.

Tab. 7: Characteristics of the IFPEN constant volume vessel.

Internal width	125 mm
Windows diameter	80 mm
Internal volume	1400 cm^3
Combustible gas fill	Sequential
Mixture preparation	Stirring fan, in the upper corner (3140 rpm)
Ignition system	4 spark plugs, in the lower corners
Wall temperature	473 K (200˚C)
Nozzle tip protrusion	3 mm

The working principle [122] of this HPHT vessel can be described as:

1. **Filling:** The vessel is sequentially filled with the flammable mixture, composed of hydrogen (H_2), ethylene (C_2H_4), nitrogen (N_2), and oxygen (O_2). The pressure and temperature of the mixture at the end of the filling process defines its density. The proportions of the gases are controlled by their partial pressures when introduced in the vessel. Product compositions are calculated assuming complete combustion [19]. With this method, the oxygen mole fraction at the instant of spray injection can be adjusted for different boundary condition targets.
2. **Pre-combustion (or pre-burn):** The mixture is mixed with a stirrer during 30 seconds after the end of the filling, before the flammable mixture is ignited by 4 spark plugs located in the corners of the vessel. The combustion of the mixture generates a rapid rise of the pressure and temperature within the vessel.

3. **Cool down:** Following the spark-ignited, premixed combustion, the combustion products cool over a relatively long time (700–2500 ms) due to heat transfer to the vessel walls and the pressure decreases slowly.
4. **Injection:** When the desired temperature is reached, the injection is triggered and the diagnostics are performed.

The wall temperature of the vessels are kept at 473 K (200˚C) with electric resistance heaters that are controlled by a closed control unit. This temperature is clearly above the room temperature and it provides a slower cool down after the pre-combustion and reduces the thermal stress on the glass parts. It also prevents condensation of water on metal and glass parts. More information about the facility is given in [109].

Injection system

The fuel is supplied to the injector through a pipe linked to a common rail, respecting the ECN specifications [120]. A hydro-pneumatic pump is used to generate the pressure. Its maximum capacity is 2750 bars. The injector nozzle is an ECN-standard nozzle (ECN reference: 678) and was produced by Bosch. It is mounted on commercial CRI 2.16 body. The nominal characteristics of this nozzle is described in Tab. 8.

Tab. 8: Nominal characteristics of ECN nozzles.

Number of holes	1 (single hole)
Nozzle outlet diameter	90 µm
Nozzle shaping	Hydro-eroded
Nozzle k-factor	1.5
Mini-sac volume	0.2 mm^3
Discharge coefficient C_d	0.86 (at 100 bar)

Spatially-resolved temperature measurements by thermocouples and schlieren measurements showed that in pre-combustion type vessels, temperature stratification in the vertical direction occurs [19] which is caused by buoyancy. Temperature can vary by ±4% over a vertical distance of ±15 mm. The temperature is uniform, however, along horizontal planes [19]. Therefore, in Spray A measurements, the injector is mounted at the side of the vessel to create a horizontally penetrating jet in a uniform temperature environment.

5.2 Characterization of the Diesel combustion vessel

5.2.1 Nozzle-tip temperature

The evolution of the fuel temperature during the injection event is likely to influence the spray characteristics, in particular the liquid length. Therefore it is important to be able to control its temperature. Since the measurement of the fuel temperature during the injection event is a challenge, the solution chosen by the ECN community is to measure the evolution of the temperature in the sac volume during the pre-combustion using a dummy injector [45]. The custom-made nozzle has no orifice, and the injector is equipped with a type K thermocouple which allows to measure the temperature in the sac volume, at different distances from the bottom of the sac (cf. Fig. 30). To provide the heat transfer from the nozzle to the thermocouple homogenously, the sac volume is filled with thermal paste.

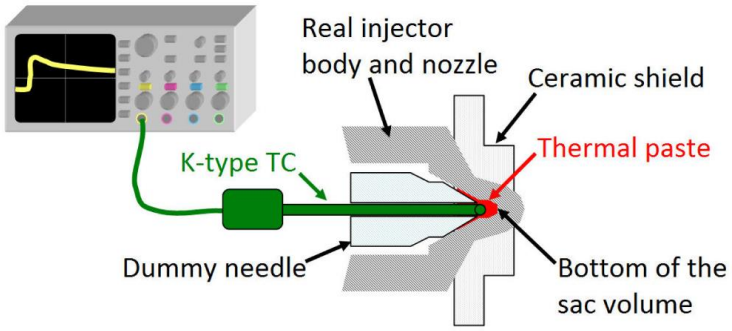

Fig. 30: Scheme of the setup used to measure the temperature in the sac volume with a dummy injector.

In order to limit the temperature rise within the sac volume, ECN injectors are shielded with a ceramic cover that insulates the nozzle and reduces the heat transfers between the hot gases within the vessel and the injector. The dummy injector is also mounted with the same ceramic shield. In order to keep the fuel at the target temperature that is well below the temperature of vessel wall (200˚C), a liquid cooling system is integrated to the injector body housing. This cooling system has also a closed control unit and the target temperature of the cooling liquid (water) can be adjusted. Fig. 31 shows the time-resolved nozzle tip temperature measured after the pre-combustion event. To keep the nozzle tip at 90˚C temperature at the time of injection, the liquid temperature of the cooling system should be set to ~70˚C in this setup. The ~5˚C rise within the first 1 s is due to the above-mentioned rapidly increasing temperature inside the vessel with the pre-combustion. Without the ceramic shield this temperature rise would be more substantial.

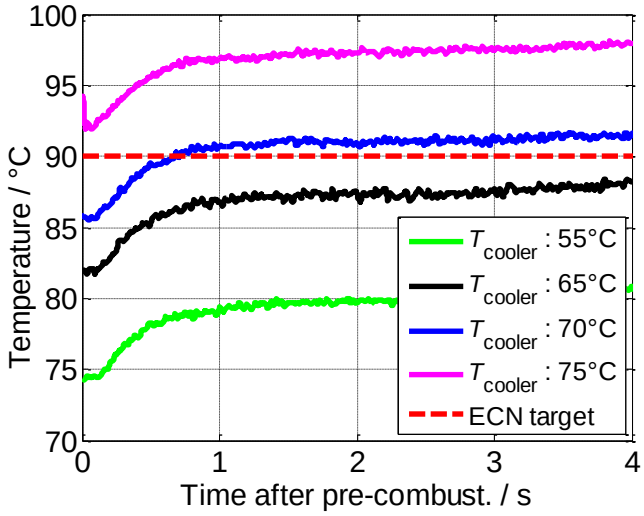

Fig. 31: Nozzle-tip temperature controlled by the liquid cooling system.

5.2.2 Ambient temperature and density

After the pre-combustion event, during the cool down process, the gas temperature and the density are not homogeneous in the vessel due to buoyancy and thermal boundary layers generated by heat transfer at the walls of the vessel [19]. Meijer et al. [45] investigated this spatial temperature stratification in the vessel with fine thermocouple measurements and showed that the average temperature values (named as “bulk”) are different from the local values. The ECN standard conditions, however, represent the actual values at the region of interest (where the Diesel jet interacts with the ambient medium), therefore these local temperatures should be precisely measured and set to these target conditions. This geometric center of the vessel can be regarded as a reference point for the region of interest and named as “core” in this work.

Unlike the temperature, the pressure within the vessel p_{vessel} is homogeneous (at least for the subsonic time scales) and it is continuously monitored with a standard piezoelectric transducer assembled to the vessel. By using the real gas law and this pressure information, a bulk temperature T_{bulk} (i.e. the average temperature) in the vessel can be calculated as

$$T_{\mathrm{bulk}} = \frac{p_{\mathrm{vessel}}}{Z\, r\, \rho_{\mathrm{bulk}}} \qquad (18)$$

where Z, r and ρ_{bulk} are respectively the compressibility factor (needs to be taken into account for real gas effects) [122], the gas constant of the mixture, and the average density in the vessel (controlled during the filling of the vessel). The center of the vessel is the furthest point to the vessel walls in the combustion chamber, therefore this region is less affected from the colder walls than any other point in the vessel. This eventually leads that the core temperature T_{core} (in the center of the vessel)

is higher than T_{bulk} within the first 2 seconds after the pre-combustion. To quantify this difference, the temperature in the center of the vessel is measured with a type K 50 µm diameter thermocouple as shown in [45,122]. The raw temperature measured by the thermocouple is corrected to take into account the effects of the radiations, convection, and thermocouple inertia [122]. Fig. 32 shows the temporal evolution of T_{bulk} and T_{core} after the pre-combustion. T_{bulk} is calculated from the pressure data, and T_{core} is measured by the thermocouple. Each curve is an ensemble average of 5 measurements. The gray and black envelops around the temperature curves are the standard deviation evaluated during ensemble averaging.

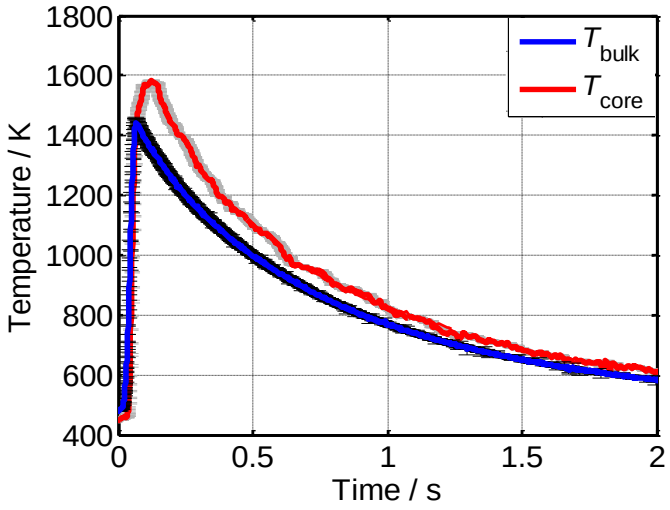

Fig. 32: Temporal evolution of T_{bulk} calculated from pressure data, and T_{core} measured by a thermocouple at the center of vessel.

The ambient temperature during a spray event is adjusted by the delay of injection with respect to the pre-combustion. The right delay time for Spray A condition is defined at where the ensemble averaged $T_{\mathrm{core}} = 900$ K. The thermocouple signal in this analysis is smoothed with a low-pass filter as described in [19].

Due to the temperature gradients (and uniform pressure), the density of the gas is also not homogenous within the vessel after the pre-combustion. The actual density in the spray zone ρ_{core} can be evaluated by using the pressure-temperature relation (Gay-Lussac's law) and thermocouple measurements:

$$T_{\mathrm{core}}\,\rho_{\mathrm{core}} = T_{\mathrm{bulk}}\,\rho_{\mathrm{bulk}} \qquad (19)$$

By using a time averaged value of T_{bulk} and T_{core} between 700 and 1000 K, the actual ρ_{core} is calculated as 5.3% lower than ρ_{bulk}. To compensate this reduction at the spray region, ρ_{bulk} is set to

24 kg/m^3 by increasing the amount of intake gases prior to the pre-combustion to match ρ_{core} = 22.8 kg/m^3.

5.3 Spray characterization

5.3.1 Rate of injection

The mass flow rate was measured with a commercial EMI2-EFS flowmeter. The measurement principle is the following: The fuel is injected in a chamber filled with fuel. The volume of this chamber is controlled by a moving piston. A back pressure is applied to this piston. The piston displacement is measured and is used to provide the mass flow rate. With the periodic mass flow rate measurements during the measurement campaign and by comparing the flow rates, the repeatability of the experiments is verified.

5.3.2 Liquid penetration length

Liquid penetration length is the maximum penetration distance of liquid-phase fuel in a Diesel spray at the steady state. At this point the total fuel evaporation rate in the spray is equal to the fuel injection rate. Once the liquid fuel reaches this point, it begins fluctuating about a mean axial location. The liquid penetration length depends strongly on the gas temperature and density, fuel volatility, density and viscosity, and the orifice diameter [109]. Therefore, it can be a good indicator to compare with the existing ECN database [21] and to verify how well the ECN conditions have been reached. Following the recommended best-practices in the ECN community [21], the Diffuse Back-Illumination (DBI) technique is used to measure the liquid penetration length in this work. This method is based on the extinction of incident light by the liquid-phase fuel. Fig. 33 shows the setup used for DBI.

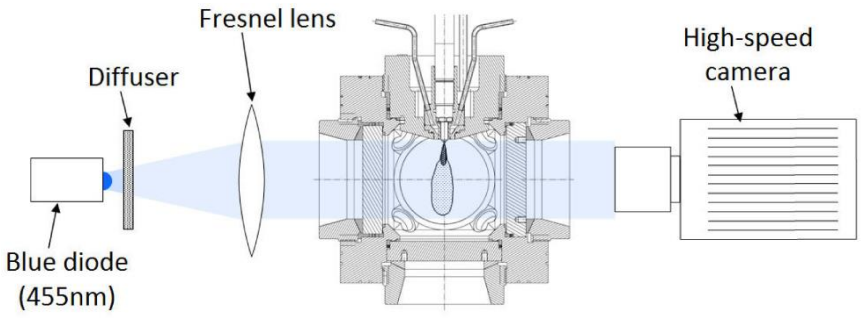

Fig. 33: Diffuse back-illumination setup for liquid penetration length measurements.

The light source is a blue diode at 455 nm. The homogeneity of the intensity of the incident light is essential for the accuracy of the measurements [110]. In order to obtain an illumination as uniform

as possible, an engineered diffuser is placed in front of the diode. A Fresnel lens is then used to collimate the light. The signal is collected by a high repetition rate Photron SA1 camera with a frame rate at 120 kHz, equipped with a 50 mm *f*/1.2 lens and an 8 mm extension ring. The resolution of the images is 320×112 pixels, and the spatial scale is 88.5 µm/pixel. In Fig. 34 four DBI images are shown obtained at different delays after the start of injection. The image at the lower right corner is acquired at the steady-state where the liquid length is fully developed. For extinction measurements the images acquired at steady-state are time averaged to suppress the fluctuations.

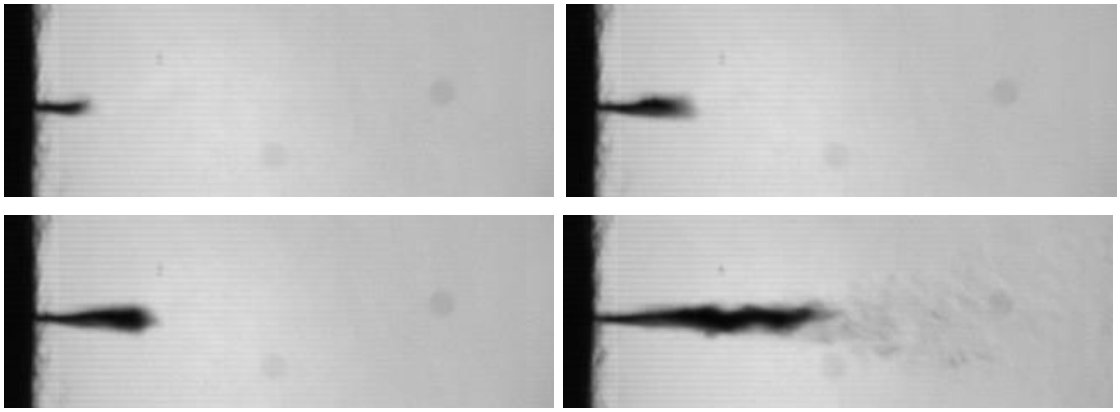

Fig. 34: Extinction images obtained with the DBI setup at different delays after the start of injection.

By following the Lambert-Beer's law (see section 3.2.1), the time-averaged intensity images can be converted into extinction images. Then, at each pixel column, pixels within the range of +/- 5 mm around the spray axis are averaged to a single value, and for each spray an axial extinction profile is created. Fig. 35 shows the extinction profiles of 10 sprays (gray thin lines) and the ensemble average of these profiles (thick blue line). Near the liquid core tip, beam steering is significant, and thus the extinction value is the consequence of both light extinction and beam steering. The profile in this region can therefore not be taken into account to compute the liquid length. Instead, the slope of the decay of the extinction profile is computed, and the liquid length is defined as its intersection with the *x*-axis [123].

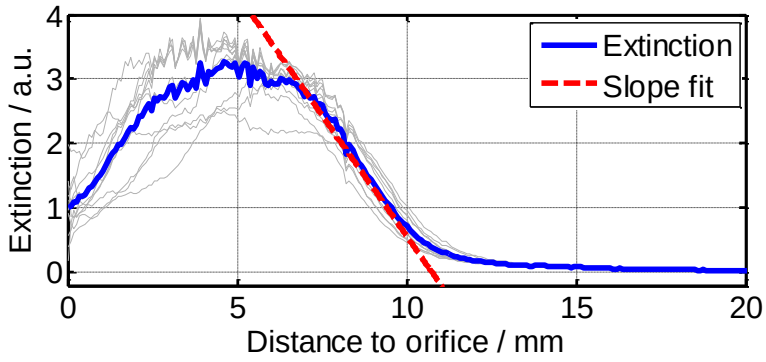

Fig. 35: Liquid length defined by the extinction profile at the spray axis.

Among different techniques [124] the ECN community announced that the DBI technique is the preferred method for back-to-back comparison of results originality from different labs. The prominent advantages of DBI are that it is has a simple setup and it is self-calibrated [124,125]. On the downside the DBI method suffers from beam steering and this limits the measurement precision for the actual liquid penetration length.

5.3.3 Vapor penetration length

The vapor penetration length is the maximum penetration for the length of vapor-phase fuel at a given time. It depends on the hydraulic flow rate of the injector (rail pressure and nozzle characteristics) and the ambient density. Therefore, like the liquid length, it is also a useful parameter to verify the validity of the ECN conditions in the cell. Schlieren imaging is used to identify the vapor boundary of the penetrating jet [19,122–124]. The evaporated fuel has a clearly different temperature and density than the ambient gas. Therefore its refractive index is also different than the ambient gas. The schlieren imaging is sensitive to gradients in refractive index, formed by either such density or composition differences along a line-of-sight, and is therefore a robust tool to mark the boundary of the vapor-phase of a penetrating jet. Fig. 36 shows the setup used for schlieren imaging. Vapor penetration length measurements are conducted in non-reactive Spray A (0% O_2).

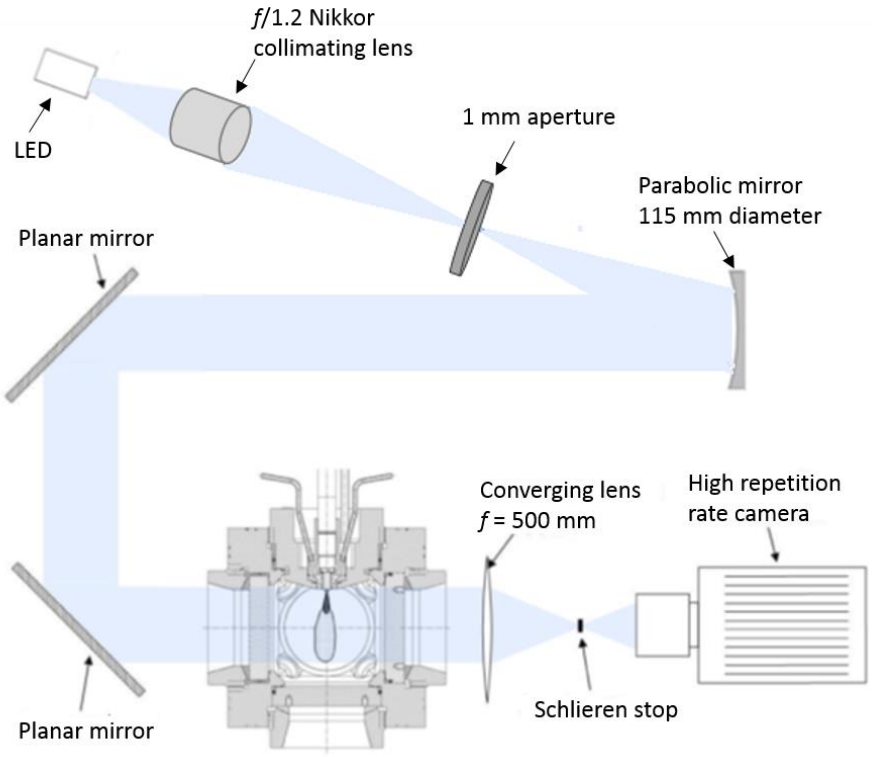

Fig. 36: Schlieren imaging setup for vapor penetration length measurements.

A parallel light beam with a diameter of slightly above 100 mm is created by using a set of a LED, a camera lens, a 1 mm aperture, and a parabolic mirror. The collimated light is passed through the combustion vessel. A large collection lens is used to direct the parallel light onto a cutoff disk (schlieren stop) with a diameter of 1.2 cm. Deviated rays do not fall onto the disk and they are collected with a high repetition rate Photron SA1 camera, equipped with a 100 mm *f*/2.8 lens and a 8 mm extension ring. The resolution of the images is 640×240 pixels, and the spatial scale is 117 µm/mm. The frame rate is 30 kHz. As a result, the sprays appear in white on a dark background (dark field schlieren). This setup has been chosen over the bright field setup because it gave the best contrast for the spray images. A set of schlieren images acquired at different delays after the start of injection is shown in Fig. 37. The outer boundary of the fuel vapor is determined through image analysis with MATLAB (shown as blue contour line). For each image the vapor length is defined as the maximum distance of the contour line along the spray axis to the orifice. Fig. 38 shows the vapor penetration length as a function of time for two different ambient bulk density targets. Each curve is an ensemble average of five cycles and vertical lines represent the standard deviation due to ensemble averaging. The reason why the vapor length curve does not start at 0 mm is related to an error encountered during the determination of boundary line.

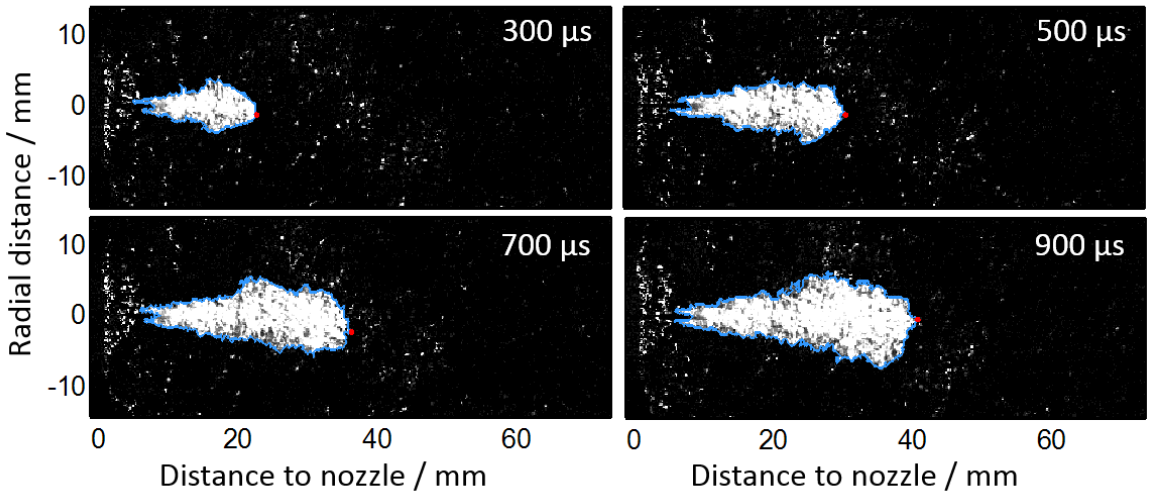

Fig. 37: Schlieren images acquired at different delays after the start of injection to measure the vapor penetration length.

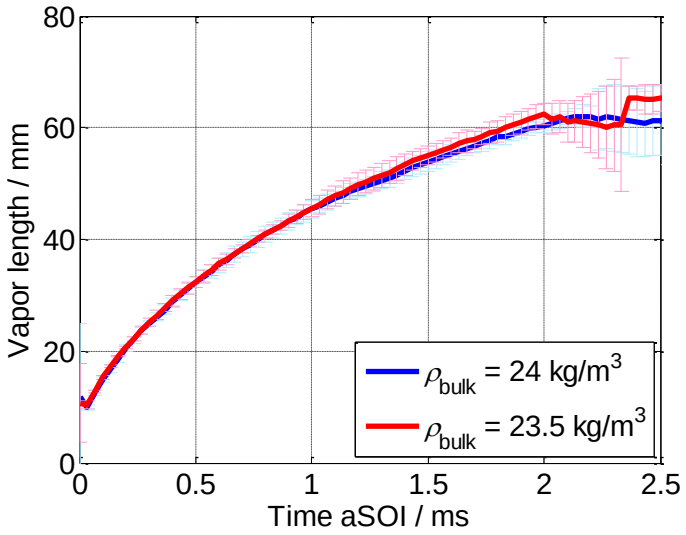

Fig. 38: Vapor penetration length at two different bulk ambient density.

5.3.4 Lift-off length

In near-stoichiometric, high-heat-release combustion reactions, excited-state OH radicals (OH*) are formed as intermediates. Unlike ground-state OH, which exists as an equilibrium product in regions of high temperature, including hot exhaust gases, OH* only exists in the flame zone [47] and emits chemiluminescence at around 310 nm. Thus, with an appropriate band-pass filter it is possible to locate zones that can be correlated with near-stoichiometric, high-heat-release conditions [47,116,126,127]. Because stoichiometric combustion is expected at the flame base [47,128], i.e., at

the lift-off location, chemiluminescence imaging is also the appropriate method to identify the lift-off length of a spray flame. During the quasi-stationary phase of the spray, the lift-off length is not varying systematically. However, small deviations occur due to turbulent fluctuations. In order to suppress these fluctuations and achieve a steady lift-off length measurement, time-averaged imaging is employed via sufficiently long camera gates (500 µs) within the quasi-stationary phase of the flame. Fig. 39 shows the OH*-chemiluminescence imaging setup for lift-off length measurements. The lift-off length imaging is done in a line-of-sight manner.

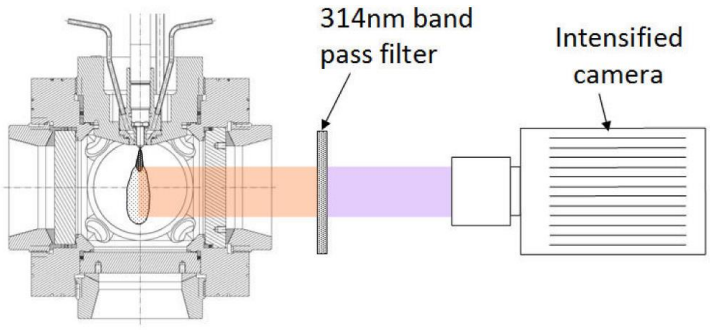

Fig. 39: OH*-chemiluminescence imaging setup for lift-off length measurements.

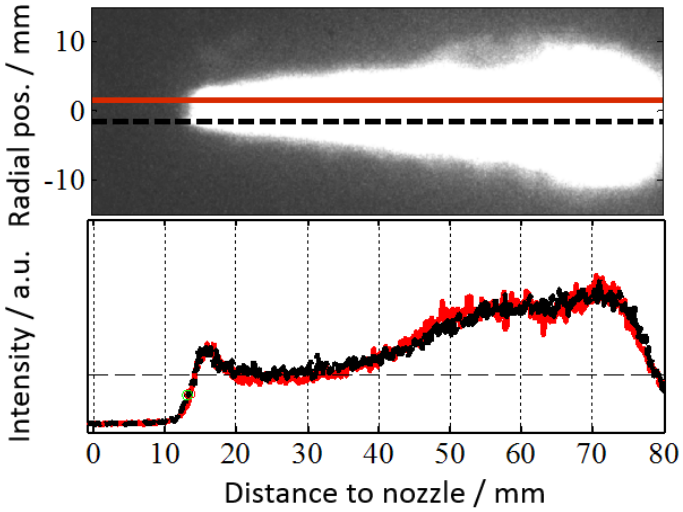

Fig. 40 OH*-chemiluminescence imaging of Spray A. Intensity profiles along the lines indicated in the image show the rapid intensity increase that allows identifying the lift-off length. The signal increase towards the right is due to interference from soot incandescence.

Fig. 40 shows an OH*-chemiluminescence image. OH*-chemiluminescence begins at a well-defined distance from the injector orifice, initially rising very sharply, and then leveling off. Two lobes of intense chemiluminescence on the top and bottom of the jet are typical near the lift-off length. The lift-off length was determined by finding the distances between the injector and the first axial locations

above and below the spray centerline with an intensity greater than approximately 50% of the leveling-off value. The average of these two axial distances is defined as the lift-off length [20]. The intensity increase downstream is due to broad-band blackbody-like radiation of soot particles.

5.3.5 Determination of the local oxygen/fuel ratio

An estimate of the amount of air entrained into a fuel jet was used to help analyze the soot and lift-off measurements. As shown in Fig. 40, Spray A is a lifted flame. The amount of fuel and air premixing that occurs upstream of the lift-off length affects the composition of the reactants downstream of the lift-off. Because soot formation and burnout is directly related to oxygen availability in a region, air entrainment into the jet is crucial for the soot formation rate and its location. Additionally, air reacting in the non-premixed flame and then entrained downstream of the lift-off length will affect soot formation processes further downstream [47].

When the ambient oxygen concentration is varied, fuel jets have different levels of relative oxygen entrainment at a given distance from the injector. For example, because a reduced mole fraction of ambient oxygen or reduced ambient density will result in less oxygen entrainment at the same axial position. Therefore, to compare the effects of oxygen concentration on soot, it is useful to compare the fuel jets at the locations of similar relative oxygen/fuel mixture. For this purpose, Pickett et al. [36,39] used the air/fuel ratio at various axial locations in a fuel jet relative to the air/fuel ratio required for stoichiometric combustion. This value is described as the oxygen/fuel ratio and denoted with Ω [36,37,39]. In spray research community Ω is also called as the effective "flame" coordinate since the fuel jet combustion and soot formation processes are compared at equal relative oxygen/fuel mixtures [36].

For non-oxygenated fuels [37], Ω defined by Eq. 20 is inversely proportional to the average equivalence ratio $\overline{\Phi}$.

$$\Omega = \frac{1}{\overline{\Phi}} \qquad (20)$$

The average equivalence ratio $\overline{\Phi}$ at a given axial distance is calculated with Eq. 21 [39,129]:

$$\overline{\Phi}(x) = \frac{2\,(A/F)_{st}}{\sqrt{1 + 16\,(x/x^{+})^{2} - 1}} \qquad (21)$$

where $(A/F)_{st}$ is the stoichiometric air–fuel ratio by mass, and x^{+} is a characteristic length scale for the fuel jet. The characteristic length scale is defined as:

$$x^+ = \sqrt{\frac{\rho_f}{\rho_a}} \frac{\sqrt{C_a} d}{\alpha \tan(\theta/2)} \beta \qquad (22)$$

where d is the injector orifice tip diameter, C_a is the orifice area contraction coefficient (it is taken as 0.89 according to the ref. [121]), ρ_f is the fuel density, ρ_a is the ambient gas density, α is a constant with a value of 0.75, $\theta/2$ is the jet spreading half-angle (it is taken as 21˚ for ECN Spray A nozzles [130]) and $\beta = (T_{ad}/T_a)^2$ (T_{ad} is adiabatic flame temperature of a stoichiometric fuel-ambient mixture and in this study it is calculated with CHEMKIN tool for constant volume conditions. T_a is the ambient gas temperature) is a term that accounts for a reduction in air entrainment in the reacting region of a fuel jet downstream of the lift-off length caused by heat-release effects. To estimate the air entrained at the lift-off length, a value of β = 1.0 is used since little heat release occurs upstream of the lift-off length [36].

5.4 Optical setup

Fig. 41 illustrates the arrangement used for coupling LII and laser extinction measurements in the vessel. The LEM setup is based on the work of Musculus et al. [40] and minimizes the influence of beam steering or soot incandescence interference. The same approach was also used for in-cylinder measurements [21].

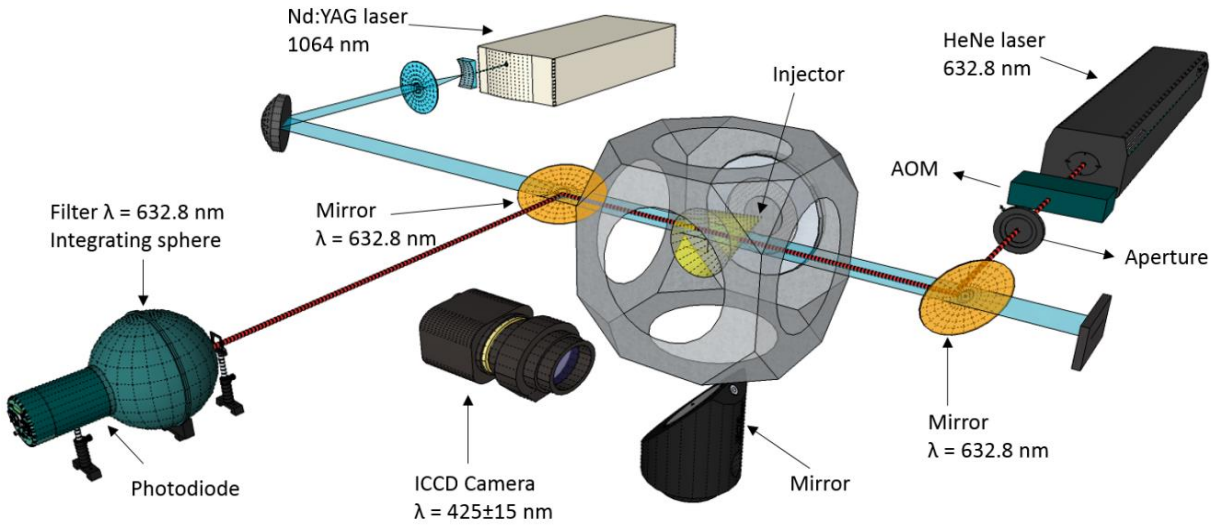

Fig. 41: Optical arrangement for combining LII and LEM.

For LEM the beam of a 35 mW continuous-wave (cw) HeNe laser (632.8 nm) is transmitted horizontally through the quartz windows of spray vessel. The laser targets the spray axis 58 mm downstream of

the nozzle orifice. This location is chosen deliberately in the light of preliminary studies. It is observed that highest soot concentrations in a Spray A occur at about this distance. The laser beam is modulated using an acousto-optic modulator (AOM) driven by a 100 kHz pulse generator for measuring the background luminosity and discrimination against incident laser light (method will be further discussed in section 5.5). An aperture selects the beam that is deviated to the first order when the AOM is active. Behind the vessel, the beam is collected into an integrating sphere using a lens of 50 mm diameter and 200 mm focal length. The role of the integrating sphere in front of the photodiode is to reduce the sensitivity to variations of the position and incidence angle of the laser beam. A circular 25-mm aperture is placed in front of the sphere, providing a 125 mrad collection angle. This provides a good compromise between the suppression of beam steering and forward-scattering [21,40]. A band-pass filter (633±0.5 nm) suppresses unwanted combustion luminosity and soot emission as well as 1064 nm laser radiation. It should be noted that the selected laser light (632.8 nm) can be absorbed by non-soot species, such as PAH [131]. This additional extinction of the laser light may lead to a discrepancy between the optical thicknesses obtained by LEM and LII measurements and should be taken into account as uncertainty for these measurements.

The LII measurements are based on soot heating with the fundamental of a Nd:YAG laser working at 10 Hz with a Gaussian beam profile. This 1064 nm wavelength is preferred over the frequency-doubled output to suppress the interference from fluorescence of polycyclic aromatic hydrocarbons (PAH) [14]. A set of cylindrical and spherical lenses forms a horizontal laser sheet intersecting the spray axis between 24 and 70 mm distance from the nozzle tip. In order to avoid thickness variation in the direction of laser propagation due to the convergence of the observed region, a second lens set (−100 and 1000 mm focal lengths for a cylindrical and spherical lens, respectively) is used with a focal point far behind the vessel. The laser sheet at the region of interest is measured as approximately 1 mm thick by a paper burn test. Because the Gaussian profile of the laser sheet in the axial direction, the laser sheet thickness loses its uniformity towards to the edges and gets thinner. However, paper burn tests also showed that the laser sheet thickness is uniform between 34 and 60 mm. Therefore, for soot volume fraction measurements, only the axial distances between these two limits are used. The laser sheet is coplanar with the 632.8 nm LEM laser.

The LII measurements are performed in the high fluence regime with a Gaussian profile of the beam across the short axis of the laser light sheet. The beam-integrated laser fluence is above 1 J/cm^2 which is securely above the saturation regime (~0.3 J/cm^2 at 1064 nm) [14,55]. Nevertheless, the reported LII signal plateau zone value in the literature for increasing laser fluence was measured under atmospheric conditions. The sublimation behavior of the soot at ~60 bar, however, is not fully known. In this

study, it is assumed that the soot at such pressures also reaches to the constant sublimation temperature. The LII signal is detected with a 16 bit intensified CCD camera equipped with a f = 50 mm, f/1.2 lens and a band pass filter (425±15 nm). In this spectral range, the sensitivity of blackbody radiation to temperature is higher when compared to longer wavelengths [65]. Therefore, a better differentiation of natural incandescence of particles outside of the measurement volume and the LII signal can be achieved. The temporal camera gate is 50 ns. To prevent the LII laser from hitting the LEM photodiode the two laser beams cross the combustion chamber in opposite directions.

5.5 Measurement strategies

For each measurement, LEM was conducted in a temporally-resolved manner. Data acquisition started with triggering of the injection triggering and continued for the next 8 ms. The high-frequency modulation of the laser light enables the suppression of the flame luminosity. Within the entire period of a measured time trace (8 ms), the laser is switched on/off 800 times. During the off-time, the photodiode detects only background intensity. During the on-time, photo diode detects both laser and background intensity. By subtracting the consecutive off-time from the on-time intensities, one can measure the transmitted laser intensity. This consecutive subtraction is done with a lock-in amplifier. The output voltage is measured with an oscilloscope. Such high frequencies of modulation are normally preferred to freeze the chemical and physical processes between consecutive on/off times.

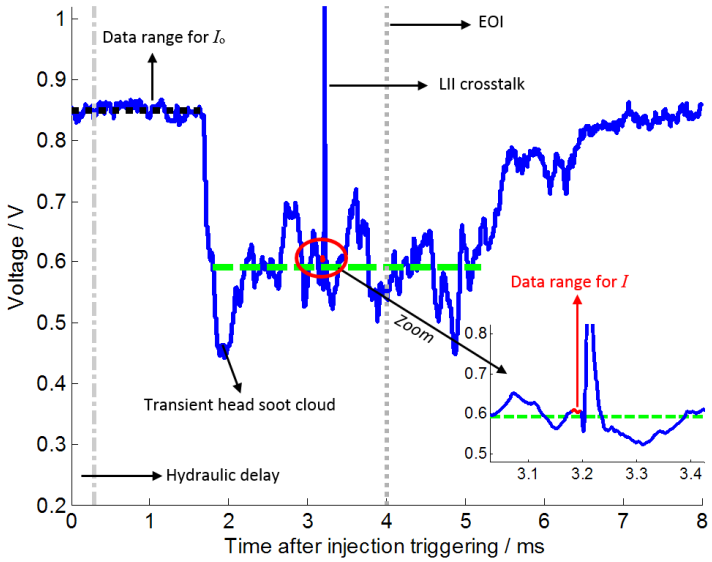

Fig. 42 Extinction signal for a single spray event with 4 ms injection duration. Data acquisition starts with the injection triggering signal. After ~2.0 ms the tip of the soot cloud reaches the measurement location. The dashed green line indicates the mean during the quasi-stationary period. The sharp signal at 3.2 ms is due to interference from LII.

Fig. 42 shows an extinction signal from a single Spray A event with 4 ms injection duration (End of Injection event is denoted as EOI and shown with a vertical dotted line). After the injector trigger, a ~300 µs hydraulic delay occurs. Following this delay, the spray starts to penetrate into the chamber. This actual start of injection event is denoted as SOI. Following the autoignition and soot formation processes, the first soot particles reach to detection zone at 58 mm depth in spray axis about 1.5 ms after the start of injection. Within the first 1.5 ms, the signal exclusively shows the incident signal and I_0 is calculated as the mean of this data range. The fluctuations in this time zone are due to the electronic noise in the detection system.

As shown in the next section, the transient soot cloud head is larger in diameter compared to the quasi-stationary spray. Therefore, when the soot cloud first arrives at the measurement location, the laser extinction is stronger compared to the quasi-stationary spray. Following this instant, extinction, i.e., the line-of-sight integrated soot concentration is steady without any systematic changes. However, random deviations around the mean value occur due to turbulent fluctuations. The mean value is shown with the dash-dotted green line between 2 and 5.2 ms to show these fluctuations. This quasi-stationary behavior lasts for slightly more than 3 ms. Note that this duration does not represent the injection duration time of 4 ms.

Shortly after 3.2 ms, a sharp signal peak can be seen that is due to interference with the LII laser and signal. This signal is almost instantaneous and can easily be subtracted from the LEM signal. It acts as a marker for the exact determination of the timing of the LII measurement. The signal trace around the LII event is enlarged in the inset. For the calibration of LII with LEM, an LEM signal integrated over 10 µs right before the LII measurement is used.

The LII images must be corrected for signal contributions from “natural” incandescence of soot that are present behind or in front of the LII laser sheet. Additionally, CH* chemiluminescence is also in the spectral range of detection and thus contributes to the collected signal. Therefore, luminosity images were taken in independent spray events with the laser off at corresponding boundary conditions and with the same camera gate. For each condition at least five measurements were averaged to minimize the influence of turbulent fluctuations. The signal from these background luminosity images is then subtracted pixel-wise from the LII images. The average contribution of the background to the actual LII signal for Spray A is ~6% of the total signal. In lower soot conditions however, this contribution reaches up to 16% of the total signal measured.

As given in Eq. 8, a field-of-view integration of the LII signal across the sooting zone is necessary for the comparison and calibration with LEM measurements. The spatial location of this integration region is illustrated in Fig. 43 as a vertical line. This can be done by simply adding all the pixels in the

corresponding column where the LEM laser intersects the soot cloud. The width of a single pixel column is ~0.085 mm, however the diameter of the HeNe laser beam used in the LEM setup is ~1.5 mm. The HeNe laser has a 2D Gaussian profile and therefore measuring the beam diameter is not trivial. Knowing this, the KL_{LII_x} value is calculated for 18 consecutive pixel columns at the region of interest, and an arithmetic mean of these values is taken for calibration. Before averaging, a Gaussian distribution is also tried on KL_{LII_x} values. However, a higher accuracy over the direct arithmetic averaging is not seen.

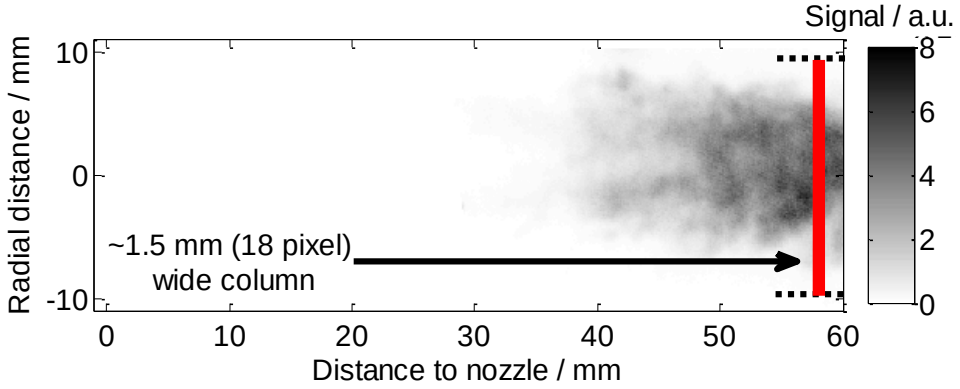

Fig. 43 Instantaneous LII image. The line at 58 mm indicates the position of the LEM laser beam. KL_{LII} is determined from an integration of the LII signal in a 1.5 mm wide area.

The fidelity of the KL_{LII} calculation is aided by identification of the spatial boundaries of the soot cloud for integration perpendicular to the spray axis. As background luminosity images are subtracted from the LII image, there is virtually zero signal outside the soot cloud (marginal deviations around zero value is due to noise and cycle to cycle variations). Nevertheless, a threshold can be defined to locate the boundaries of the soot zone thereby minimizing errors in the integration.

5.6 Results

5.6.1 Assessment of Spray A operating condition

The first aim of the measurements is to verify that the present experiment matches the target ambient conditions (temperature and density) for Spray A and compare those conditions with the similar vessel at IFPEN [19]. It is assumed that the gas inside the vessel is ideal gas [122] and the measured temperature and pressure are used to compute the gas density through the ideal gas law, including the compressibility of the gases. Temperature is measured with a thin thermocouple at the spray zone and pressure is monitored by a pressure transducer. Depending on the density predictions, the amount of fresh input gas prior to pre-combustion is adjusted as discussed in section 5.2.2. However,

due to the low signal-to-noise ratio of thermocouple data, the gas density could be calculated with a limited precision only. Several months after the soot measurements presented here, an improved analysis on the same vessel was conducted with more appropriate thermocouples. These recent measurements showed that the gas temperature used in the experiments shown in this work was 30 K above the Spray A standard. While the temperature was believed to be 900 K, the actual temperature at the spray instant was 930 K. This systematic error led to an overestimation of the gas density. Therefore, measurements in this thesis were done at around 21.8 kg/m^3 instead of the Spray A standard of 22.8 kg/m^3.

The recent determination of the ambient gas temperature also showed that the discrepancy between the two IFPEN vessels (that were used for this study and for previous ECN studies [19,45,120]) was due to a slight difference between the vessel temperature control systems. Indeed, both vessels are equipped with similar heating elements and temperature control systems. Because of the small differences found with the new thermocouples, the resulting ambient temperature before pre-combustion varies by about 20 K between the two vessels. If not taken into account, this 20 K difference affects the ambient density of the mixture before pre-combustion and is responsible for an error of 30 K and 1 kg/m^3 when targeting Spray A. However, at the time of the soot measurement experiments, these deviations have not yet been discerned and therefore soot measurements were conducted at these off-target boundary conditions. For future references, these deviations and their possible effects on the combustion process should be taken into account. Nevertheless, for simplifying the discussion, the operating point will still be labeled according to the nominal values of Spray A and its parametric variants (900, 850, 1000 K) in this work although the actual values (930, 880, 1030 K) will be reminded.

For comparison with the existing ECN data sets, fuel temperature in the sac volume, liquid penetration length, vapor penetration length (in non-reacting Spray A, i.e., 0% ambient oxygen), autoignition timing and lift-off length measurements were done following the best-practice rules of the ECN community [20]. The measured results are compared to the ECN database in Tab. 9. In addition, a third column called “ECN scaled” is presented in Tab. 9. Considering the above-mentioned discrepancies in boundary conditions, a scaling to the ECN database figures were applied based on modeling. For liquid penetration, the model from Musculus et al. [77] is used. It is found that for a deviation of +30 K and −1 kg/m^3, the liquid penetration length shortens by 5%. The same model also showed that a decrease of 1 kg/m^3 leads to about 1 mm increase in vapor penetration length at 1 ms aSOI. Finally, for the lift-off length scaling, the model from Pickett et al. [41] is used. The stated deviations in the boundary conditions resulted in a 15% shorter lift-off length. These scaling models indicate that the departures

from the ECN database for the *near* Spray A conditions in this study are in the expected direction, and can be recovered if parameters are scaled to nominal Spray A conditions.

Tab. 9 Comparison of the results of standard diagnostics to verify Spray A against the ECN database.

	Measurements	ECN database	ECN scaled
Fuel temperature / K	363±1	363	--
Liquid penetration length / mm	11±0.35	10-11	9.5-10.5
Autoignition aSOI / µs	400	390-440	--
Lift-off length [mm]	14.5±0.5	15.4-16.7	13-14
Vapor pen. length at 1 ms aSOI / mm	49.5±4	46.7±0.7	48

For liquid penetration, the measurement results were slightly above the ECN-scaled values. It is known that fuel temperature and ambient density have a major influence on the liquid penetration length. Sac volume temperature measurements were done by a dedicated injector with a thin thermocouple inside. They showed that the initial fuel temperature was precisely set to a predefined value. Considering the relatively large span of values in the ECN database, the deviation of this measurement is considered acceptable. For vapor penetration and lift-off lengths, however, the measurement results were still higher than the scaled ECN figures. In the vapor penetration measurements, a large uncertainty could not be avoided. The measurements on different days resulted with large differences. The trend of larger vapor penetrations can be explained by a combined effect of higher ambient temperature and lower ambient densities. Nevertheless, scaled ECN figures are acceptably close to what have been measured. The measured lift-off lengths are in good coherence with the ECN-scaled figures. Such uncertainties in the boundary conditions may most likely affect soot processes. Nevertheless, these deviations from the ECN database were also revealed after the soot measurement experiments only.

5.6.2 Assessing laser and signal attenuation

Under conventional Diesel spray conditions, high soot concentrations can lead to severe attenuation of the LII signal and the laser light. In case of randomly distributed soot between the laser-heated plane and the camera, this signal trapping is difficult to correct for. Attenuation of the laser light on the other hand prevents the application of low-fluence LII (where the signal depends on the knowledge of the local laser intensity). High-fluence LII in the plateau zone can even be limited in its applicable range, because the laser intensity can fall below the plateau fluence after traveling through a dense soot cloud for a longer distance. Both effects limit the applicability of LII under conditions with high soot load and larger geometric dimensions [132].

Thus, a verification of the applicability of LII diagnostics is required for the present case. In Fig. 44, simultaneously recorded KL_{LII} and KL_{LEM} values for over 100 spray events are presented. A linear curve-

fit to the entire data set (solid red line) and two linear curve-fits to lower and higher edges of the data envelope (dashed blue and green lines) based on the ordinary least squares solution are also shown. All these curve-fits are also forced to intersect the origin. Note that these measurements were conducted for calibration purposes and to allow for correlation between LII and LEM on a larger range of operating conditions and soot volume fractions. Therefore, ambient temperatures were varied for the individual measurements around the given Spray A target (±100 K).

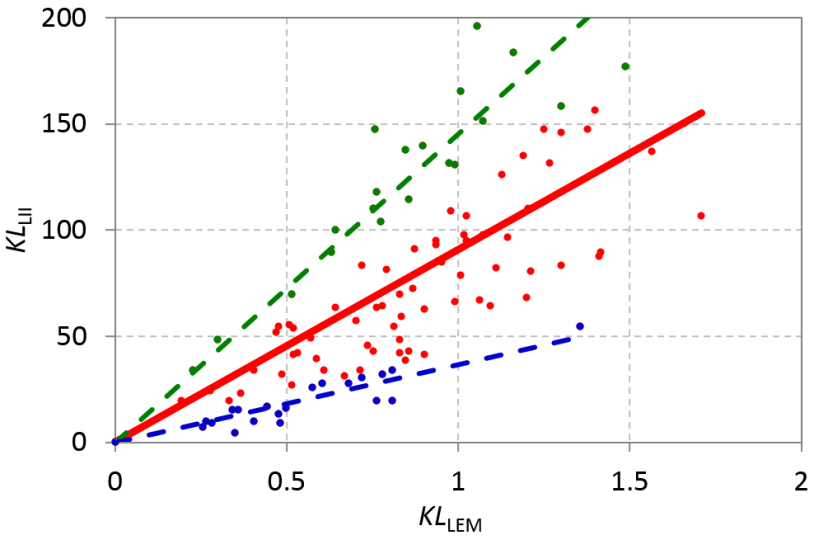

Fig. 44: Correlation between KL_{LII} and KL_{LEM} over 100 individual measurements.

The coefficient of determination for the entire data set linear curve-fit is calculated as 0.54 where the slope of the curve is calculated as 90.9. It can be speculated that this data set acknowledges the linear assumption between LII and LEM signals. However, the spread of the measurement points around the mean line is significant and represents the combined uncertainties of the measurement strategies applied here. To show the effect of this uncertainty on LII–LEM coupling quantitatively, the slopes of linear curve-fits to maximum and minimum data points are measured as 145.5 and 36.5, respectively. For these fits, data points are manually chosen from the scatter plot and can be identified with the respective blue or green color code. Concerning LEM, although the experiment was designed to minimize uncertainties due to beam steering and the natural soot incandescence as mentioned above, interference with forward-scattered laser light may remain [21]. The LEM detection is also affected by instabilities in the alignment and by variable transmission of the windows. Additionally, LEM uses an integration time of 2 µs and thus does not observe exactly the same conditions as LII (with a detection time in the tens of nanosecond regime) which can affect the correlation in a strongly turbulent and spatially inhomogeneous case. The magnitude of the total uncertainty on LEM was measured as

5% in a previous study not including the temporal variations that might occur in a turbulent application.

For LII, this present experiment was affected by a ±20 ns random jitter of the camera gate timing relative to the laser pulse which was noticed only after finalizing the measurements. The lifetime of the LII signal from the peak signal to 10% of the peak signal under the Spray A conditions was less than 50 ns (cf. Fig. 45). The LII signal is detected within a 50 ns gate. Its beginning is set 15 ns before the laser Q-switch trigger (after the Q-switch trigger, it takes approximately 5.5 ns for the laser pulse to travel the 160 cm distance from the laser to the jet). The intended position of the gate is shown by the red dotted lines in the figure. In case of a 20 ns positive jitter, shown with dashed green lines, the collected signal increases by ~5%. In the case of a 20 ns negative jitter, the collected signal reduces ~50% (dash-dotted, black lines). This jitter was caused by an electronic problem in the timing circuit and is thus responsible to a large extent for the deviations seen in Fig. 44. With an improved system, a correlation like that demonstrated in [21] is expected.

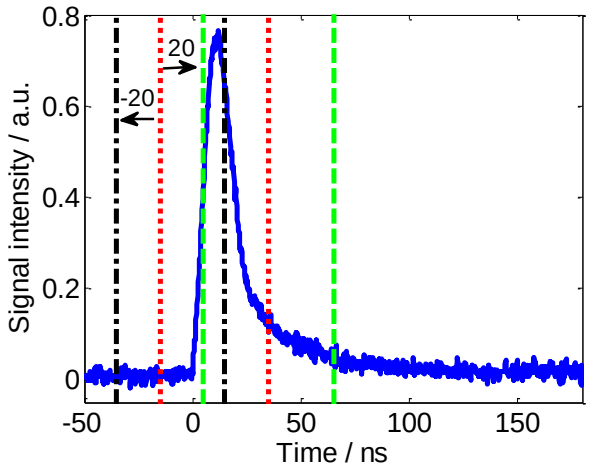

Fig. 45: Temporal variation of the LII signal. The red dotted lines show the intended temporal position of the 50 ns detection gate, black (dash-dotted) and green (dashed) lines indicate the shift of the gate caused by the unintended ±20 ns jitter that occurred in the present measurements.

Although the standard deviation is high, from Fig. 44 it can be derived that Spray A and its variants provide moderately sooting conditions with limited laser attenuation and signal trapping that allow the application of LII. In case of strong signal trapping, a systematic decrease in KL_{LII} would take place for increasing soot concentration showing a systematic deviation from the linear correlation with increasing KL_{LEM}. It should however be taken into account that completely avoiding signal trapping is not possible in such measurements. The contribution of the attenuation of the LII signal at 425 nm to the overall uncertainty can be estimated by using the extinction measurements at 632.8 nm. The line-of-sight integrated extinction along the diameter of the soot plume can be roughly halved to associate

it to the signal trapping in LII measurements. The wavelength-dependent absorption characteristics can be corrected by using Eq. 4.

First the transient soot structure in a Spray A with the original injection duration of 1.5 ms will be introduced. This time resolved imaging gives mainly an insight to the question of when the soot formation and oxidation mechanisms start in a Spray A. Following that, soot volume fractions of the quasi-stationary Spray A and its parametric variants will be presented. This study mainly shows the effects of ambient temperature and oxygen concentration on soot mechanisms in Spray A.

5.6.3 Transient Spray A

For imaging the transient soot cloud in Spray A, natural soot luminosity and the LEM-calibrated LII method were used. The results are given in Fig. 46 for seven instants of the spray flame development. The natural luminosity images on the left hand side cover 80 mm axial distance downstream of the nozzle. The LII images on the right hand side are limited to 60 mm which indicates the limit of the central part of the laser light sheet. The timing of these measurements with respect to start of injection is given in the figure. The actual injection duration is 1.5 ms, therefore, all the images in this time sequence show the soot behavior while no additional fuel is injected into the system. The ignition delay is around 0.4 ms, therefore, the injection duration of 1.5 ms is longer than the ignition delay, and this case is identified as *negative* ignition dwell in spray research [35].

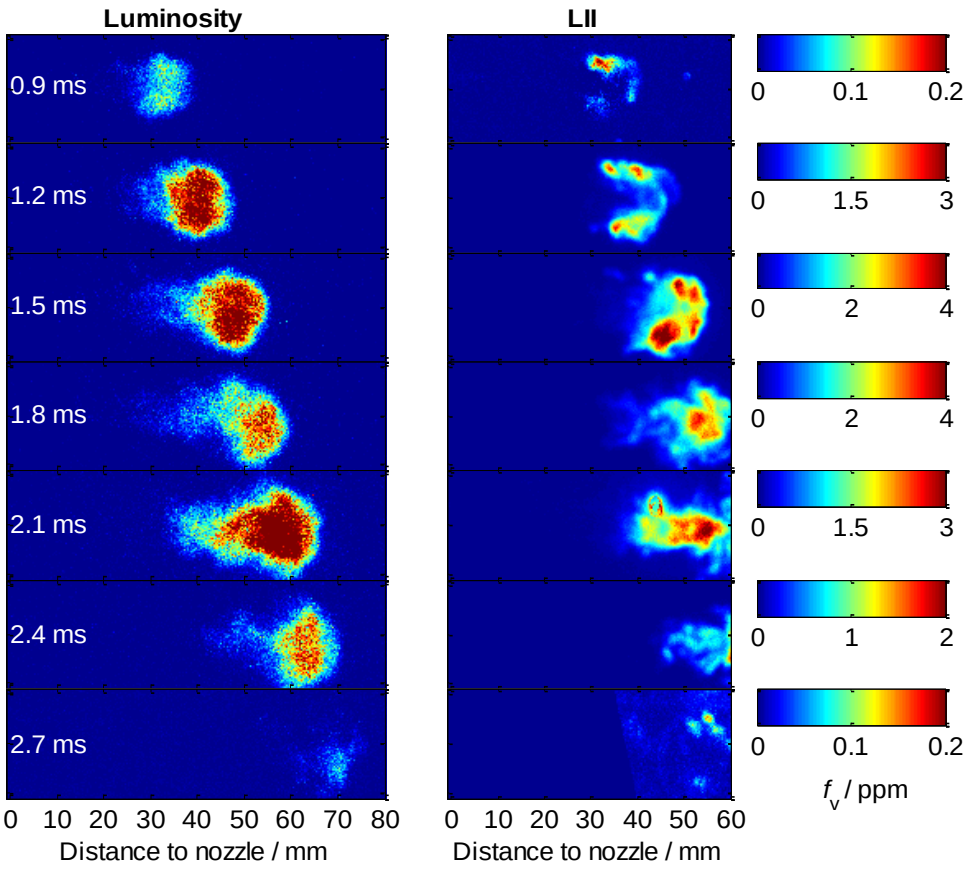

Fig. 46: Soot luminosity and LII imaging of the Spray A at seven times after SOI. Luminosity images are captured with a 50 µs camera gate. All luminosity images share the same color scale. The calibrated LII images have unique color scales giving the soot volume fraction.

Each luminosity image on the left column, is an ensemble average of three individual measurements. They are captured instantaneously with the identical camera settings of LII system. At such short gate durations with the given camera gain, lens and filter setup, soot luminosity is the only detectable process. Luminescence such as CH* emission or cool flame luminescence is too weak to significantly contribute to the signal. These images are not calibrated and are shown for qualitative comparison only. They are also used for background correction of the LII images (gate width is scaled to 50 ns with a linear assumption). LII images, on the right column, are also ensemble averaged. At each time, four LII images were captured from individual experiments. For all measurements a unique camera setting is used. After the LEM calibration, pixel intensities are converted into soot volume fraction in particles per million (ppm) units. For better illustration of the various measurement instants, different color scales are applied.

LII images at 0.9 ms after SOI shows that the soot volume fraction at this instant is very low (below 0.2 ppm). LII imaging was also conducted at 0.6 ms after SOI; however, no detectable signal is found

with the given camera setting. It is difficult to comment that soot formation in Spray A starts at the instant of 0.9 ms after SOI. Soot formation most probably starts at a slightly earlier instant and could be detected with a higher camera gain setting but the amount of soot would be marginal. Nevertheless, it can be concluded that soot volume fractions in Spray A reach considerable values first at 0.9 ms after SOI. Both luminosity and LII images at this instant also show the first-soot distance. It can be seen that this noticeable amount of soot formation occurs around 30 mm downstream of the nozzle orifice. Additional information captured from the soot images at 0.9 ms is the radial location of the soot cloud in the spray. Because luminosity images include line-of-sight-integrated data, it is difficult to identify the radial distribution of soot. The LII images, on the other hand, reveal the soot volume fraction within a cross section. It is observed that during the early phases, soot is located at the periphery of the jet, i.e., in the vicinity of the non-premixed flame zone where the temperature is expected to be higher than the reactions in the core of the jet. In the central region of the jet at lower temperature and richer mixture, there is almost no traceable soot.

At 1.2 ms the soot volume fraction increased more than 10 times with respect to previous time step. Qualitative luminosity images also verify this increase. The LII images show that at this time soot is still preferentially located at the jet periphery. The center of the jet has still not reached soot formation temperatures or residence times. The LII image at 1.5 ms shows that soot formation dominates over oxidation and therefore soot volume fractions are slightly higher with respect to 1.2 ms. Soot formation at the spray center is enhanced at this instant and the soot volume fraction is increased in this region. Images at 1.8 and 2.1 ms show that a systematic global decrease in the soot volume fraction has already started. This is attributed to oxidation of soot. As the air entrainment increases with penetration and time, soot first starts to oxidize in oxygen-rich high-temperature zones such as the boundaries of the jet. Therefore it can be seen in these images that the soot volume fraction is higher in the core area but it has already diminished at the periphery in contrast to the previous time steps. The reduced intensity at 1.8 ms with respect to earlier and later measurements is unexpected and is considered random because of the limited number of measurements and the jitter that causes a random variation in signal intensity. At 2.4 and 2.7 ms, the soot cloud has already left the observed area and only the tail of the soot cloud can be seen.

5.6.4 Quasi-stationary Spray A and parametric variation

Extinction measurements (cf. section 5.5) and transient Spray A imaging have shown that a spray with 4 ms injection duration shows a quasi-stationary behavior after the first ~3 ms of injection upstream of 60 mm. While investigating the impact of different ambient boundary conditions on the soot volume fraction, such quasi-stationary sprays allow easier evaluation of these ambient condition effects.

The steady state may also be more convenient for modeling comparison. Fig. 42 showed, however, that the turbulent fluctuations still occur in the quasi-stationary state, therefore soot volume fraction at a location may change strongly from spray to spray, i.e. cyclic variations. To suppress this, at each condition resulting soot volume fraction images are ensemble averaged. At Spray A conditions 30 single-shot images, and at other conditions 10 single-shot images are used.

Fig. 47 gives soot volume fractions of Spray A together with its ambient temperature and oxygen parametric variants. 50 ns gate duration LII images are taken 3.2 ms after injection triggering where the spray flames are in a quasi-stationary phase within the laser sheet domain. Soot volume fractions are determined from extinction-calibrated LII images. For all the conditions a single calibration constant is used as measured for Spray A (cf. Fig. 44). Figures are presented in a contour plot color scale with seven equally spaced isolines appropriate for each condition. For each parametric variation, only a single boundary condition was modified and all the other boundary conditions were kept constant.

The flame lift-off length is an essential parameter to interpret the effects of ambient conditions on soot volume fraction. The measured lift-off length is given as red vertical solid lines in Fig. 47. These lift-off measurements were not performed simultaneously with the soot measurements, but are the ensemble averaged results of five measurements. Measured lift-off lengths over a wider range of conditions are given in Fig. 48, where mean values are presented with 95% confidence intervals (vertical error bars). As known from past research [36,41,47], decreasing ambient temperature or oxygen concentration increases the lift-off length. With enough increase in lift-off length (at 800 K ambient temperature or 11% ambient oxygen concentration), the LII experiments could not detect any discernible signal, indicating low or no soot concentration within the measurement domain.

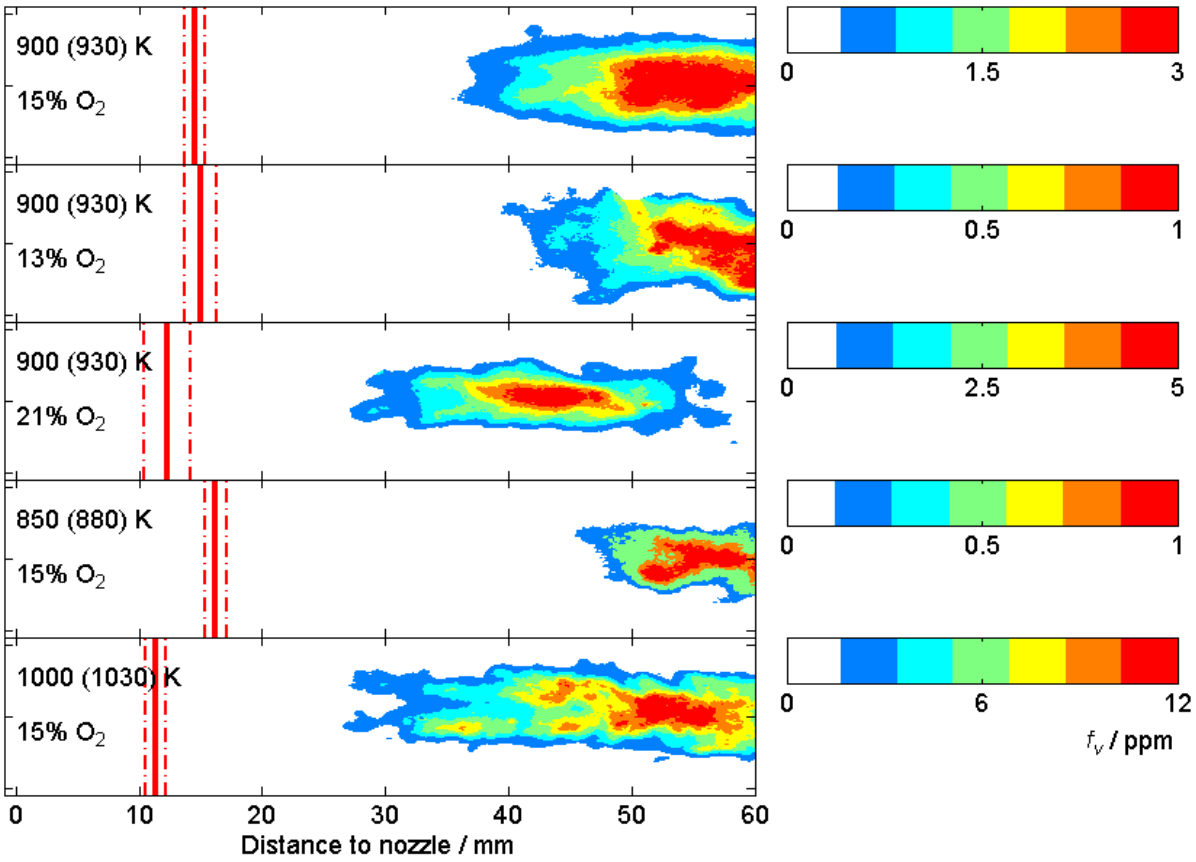

Fig. 47: Ensemble-averaged soot volume fraction images during quasi-stationary combustion for Spray A and its ambient temperature and oxygen parametric variants. Plots are labeled with nominal temperatures (actual temperatures are indicated in the parenthesis). Lift-off lengths for each condition are given as solid vertical line with 95% confidence intervals in dashed lines.

For all conditions displayed in Fig. 47, the soot formation begins well downstream of the lift-off length. The Spray A condition at the top shows soot concentrations reaching measureable amounts between 30 and 40 mm of axial length to nozzle. After this distance soot concentration gradually increases and reaches a plateau between 50 and 60 mm. The plateau indicates that soot oxidation and soot formation are in balance. Based on soot measurements at identical conditions but with different fuels, it is known that soot oxidation continues downstream of 60 mm and there is a gradual decrease in the soot concentration [38,110].

Fig. 47 shows that quasi-stationary Spray A is a moderately sooting jet. Maximum soot volume fractions of around 3 ppm are obtained at the nominal temperature of 930 K. Taking into account the peak soot volume fraction of around 1 ppm obtained at 880 K, a maximum value of around 2–3 ppm is expected at 900 K for Spray A conditions. This result confirms that signal trapping is not significant for Spray A conditions (cf. section 5.6.2). Also when increasing the ambient temperature to 1030 K, the soot level remains moderate since its peak value is below 12 ppm.

These soot levels can be compared to recent measurements at Spray A conditions using a more heavily sooting fuel [38,110]. In these studies a mixture of 23% m-xylene and 77% n-dodecane was the fuel, rather than pure n-dodecane as the Spray A standard. Maximum soot volume fraction in the jet increased from 5 ppm at 900 K to 25 ppm at 1000 K, indicating higher soot levels for the m-xylene-mixed fuel compared to n-dodecane, which is consistent for a fuel with higher aromatics. The soot measurements presented here for n-dodecane are therefore consistent with expectations based on ambient temperature and fuel type.

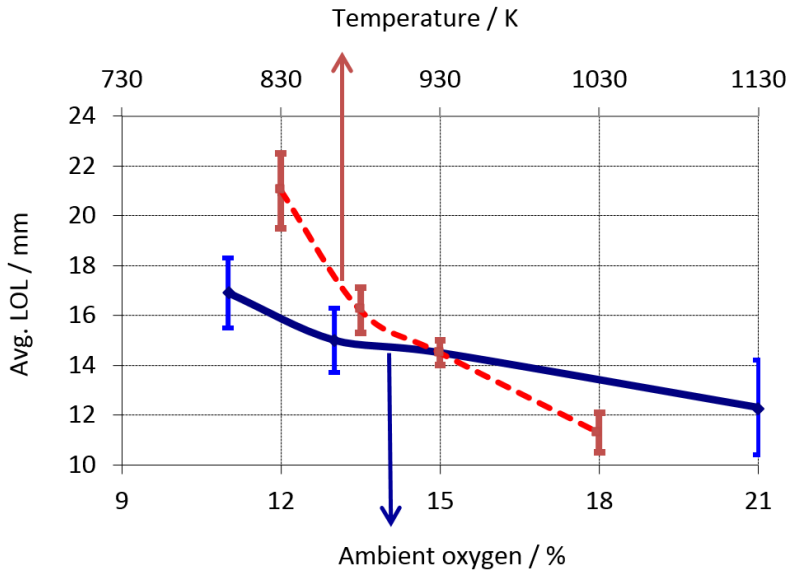

Fig. 48: Average lift-off lengths at varying ambient temperature and oxygen concentrations. The dashed red line shows the temperature changes (x axis at the top) and the solid blue line shows ambient oxygen concentration changes. Vertical error bars give 95% confidence intervals.

When ambient oxygen is varied, the region of soot formation and oxidation tends to shift upstream (increasing ambient oxygen) or downstream (decreasing ambient oxygen) [37]. For example, at 21% oxygen the peak soot concentration is at 40–50 mm and soot oxidation consumes nearly all soot by 60 mm. In contrast, at 13% oxygen, soot formation processes are delayed and pushed downstream in comparison to the Spray A condition. When only the ambient temperature is varied, the soot formation zone tends to advance towards the injector with increasing ambient temperature [39].

To account for the variation in ambient oxygen concentration, and hence the total oxygen entrained into the spray at the lift-off length or downstream, it is helpful to consider the soot measurements in a coordinate system with equal oxygen entrainment or oxygen ratio, Ω [37]. As discussed in section 5.3.5, model jet scaling laws are applied to understand the total oxygen entrained into the jet, which transforms the axial coordinate into a more universal “flame” coordinate. For the calculation of these flame coordinates, the spray angle is taken as 21° and nozzle-related flow coefficients that

were shown in ref. [121] (label of the nozzle: 210678) are used. Shown in Fig. 49 are two different analyses of the soot datasets: Fig. 49a shows integrated soot masses in thin (1 mm) radial cross-sections inside the jet are presented as a function of axial distance. To calculate the total mass of soot present within the jet, Eq. 23 is used as given in [36]:

$$m_{\mathrm{soot}} = \rho_{\mathrm{soot}} \int_{x_1}^{x_2} \int_{0}^{R} f_{\mathrm{v}} 2\pi r \, dr \, dx \qquad (23)$$

where the integral term represents the volume of soot within certain axial limits (x_1 to x_2) over the cross section of the jet, and ρ_{soot} is the soot density, assumed to be 1.8 g/cm^3 [36]. Fig. 49b shows the same integrated soot masses as a function of flame coordinate determined for each unique boundary condition.

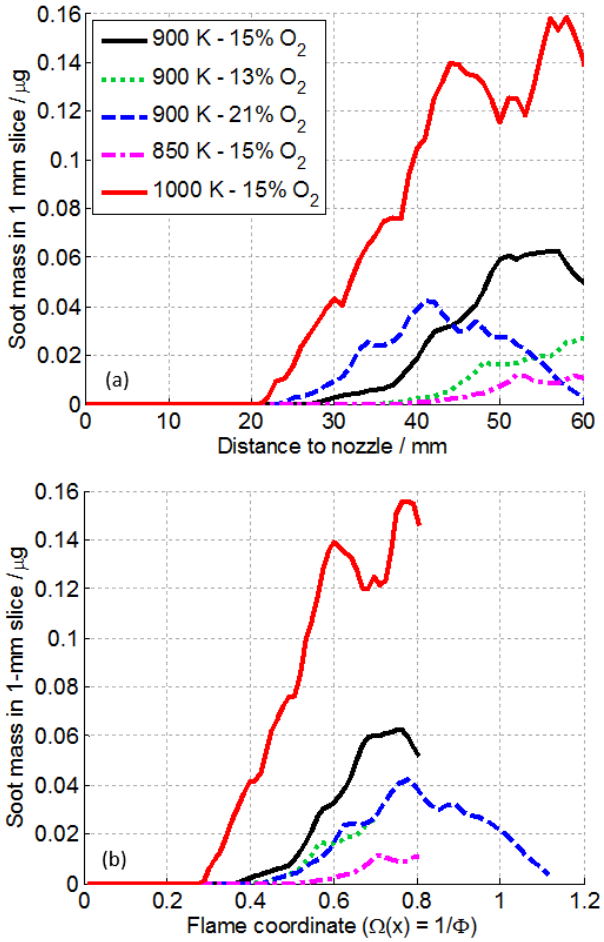

Fig. 49: Soot mass for various boundary conditions in thin (1 mm) cross-sections of the jet as a function of axial distance (a) and flame coordinate (b).

Fig. 49a shows that increasing the ambient temperature leads to an increase in the peak soot mass as well as a shift of this peak point towards the nozzle. Fig. 49b shows that as the ambient temperature

increases, soot formation occurs in more fuel-rich regions. These results are consistent with previous studies [39], shown to be the consequence of the combined effects of a shortened lift-off length, an increase in the soot formation and oxidation rates, and a shift in the balance between formation and oxidation axially along a fuel jet as temperature increases.

Furthermore Fig. 49a shows that when the ambient oxygen concentration decreases from 21 to 15%, the soot mass first increases. By further decreasing the ambient oxygen concentration from 15 to 13%, a reduction in the soot mass is observed. This initial increase and then decrease of soot mass with reducing oxygen concentration is known as “soot bump” [35,36], and it is related to the competition between residence time and soot formation rates [36]. The maximum soot mass observed at 15% oxygen concentration in this work is comparable to the results of [36] in the same temperature range. With reducing oxygen concentration soot processes also shift downstream. However Fig. 49b indicates that, although the magnitude of soot level may be different, the soot formation happens at similar flame coordinates. Unfortunately, the soot oxidation region is not within the measurement domain for most datasets (except 21% oxygen), and so this region is not represented in the flame coordinate in Fig. 49b. However these results are again consistent with previous studies [36,37] where it was found that dilution and reduced flame temperature can greatly reduce soot formation (and oxidation) rates, thereby lowering the soot concentration.

5.7 Conclusions

The work performed in this part of the thesis was the first attempt to measure the soot volume fraction of Spray A within the ECN community. Measurements are conducted for transient and quasi-stationary conditions. The relation between lift-off length and soot processes was also examined. For diagnostics, LEM coupled with LII and OH chemiluminescence methods were used. Measurements are also extended to parametric variations of the Spray A pre-defined in the ECN. Consistent with the literature results, it is shown that ambient temperature and ambient oxygen concentration have significant impact on soot processes. The following conclusions are drawn from the measurements:

A precise setting of operating conditions to the standard Spray A conditions in this study could not be achieved. For all soot measurements, the ambient density was about 1 kg/cm^3 lower and the ambient temperatures were about 30 K higher than the target values. Therefore for future references, it is recommended to take these variations into account. The difficulties in setting operating conditions to the standard Spray A conditions, which found to be caused by a lack of characterization of the ambient

temperature before pre-combustion, lead to an error in the density of the pre-combustion gas mixture. It is therefore also recommended to carefully characterize the temperature and take it into account when monitoring the gas mixture of ECN pre-combustion vessels.

Significant statistical error was observed in the present LII experiment. It was shown that jitter between the laser and the camera was the main contributor. It is therefore recommended for future ECN soot experiments to minimize the jitter.

Soot volume fraction measurements showed that Spray A is a moderately sooting spray. Maximum soot volume fractions around 2–3 ppm are obtained at near Spray A temperature (930 K) and 12 ppm at elevated temperature (1030 K). As a result, significant signal trapping of LII radiation does not occur. This was confirmed by a linearity analysis of KL_{LEM} and KL_{LII} as well as the measured laser transmission loss due to the extinction below 35% leading a KL_{LEM} value below 0.5. This measured value at the peak soot volume fraction region of Spray A is well below those values mentioned in the literature where signal trapping takes place. Therefore, 2D soot volume fraction measurements based on the LII method can be done without significant signal trapping or laser attenuation correction.

The temporally-resolved imaging of the Spray A showed that soot formation begins after autoignition during the premixed burn phase at a finite distance to the lift-off length. Cross-sectional images reveal that soot formation initially starts close to the spray periphery whereas the core region has no soot at early formation timings and locations. The expansion of soot formation process into core region happens only a finite time after the first soot formation. These transient images also show that 1.5 ms of original injection duration of Spray A is too short to establish a quasi-stationary mode of jet flow and combustion between the soot formation and oxidation zones.

With a 4 ms injection duration of Spray A, as the jet continues to penetrate downstream, a quasi-stationary region is established upstream of the penetrating transient head of the jet. The soot measurements in the quasi-stationary region show that the soot concentration in a fuel jet initially increases with axial distance downstream of the lift-off length and reaches a peak value or a plateau. However, the soot oxidation processes for Spray A could not be captured in this study entirely. For an attempt to analyze this process, a laser sheet covering all the way downstream the jet axis is necessary. The effect of ambient temperature and oxygen concentration variations were found to be consistent with previous studies.

6 Particle-size imaging at Diesel engine conditions

6.1 Sensitivity analysis for in-cylinder particle-size imaging

In this section, a model-based analysis is performed to identify an optimum strategy for particle-size imaging at engine relevant conditions. The methodology and the simulations designed for 60 bar were already introduced in section 3.1. For practicality, the LII signal library (Fig. 3b) and the simulation parameters (Tab. 1) used in this section are reprinted below in Fig. 50.

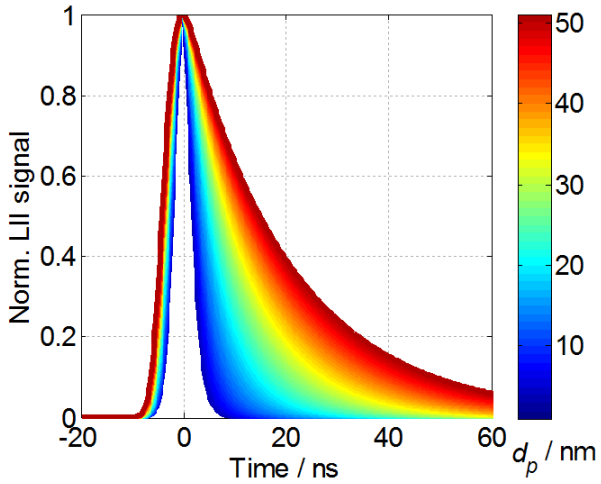

LII model input	Engine-relevant condition
Ambient pressure	60 bar
Detection spectral range	410–440 nm
Bath gas temperature	1800 K
Laser fluence at 1064 nm	0.15 J/cm^2
Laser duration (FWHM)	7 ns
$E(m)$	0.4
Aggregate size	50
Thermal accomm. coeff.	0.25

Fig. 50: LII signal "library" showing normalized time-dependent LII-signals for various primary soot particle diameters (d_p) at 60 bar and simulation parameters for the LII model.

6.1.1 Sensitivity to boundary conditions

A reference LII model function is generated for all subsequent comparisons that is calculated for mono-disperse soot particles with 30 nm diameter with the boundary conditions shown in Tab. 1. Using this signal and the identical boundary conditions as input for the curve-fitting procedure, the original 30 nm size is reproduced. By systematically changing one individual boundary condition (and keeping all others fixed) in the curve-fitting routine, the sensitivity of the system to the respective variable can be determined from the deviation in the evaluated results. Sensitivities of the LII particle sizing to the thermal accommodation coefficient, bathgas temperature, peak temperature, aggregate size and ambient pressure are shown in Fig. 51. Each plot has two *x*-axes: The axis on the top shows the nominal value of the modified variable whereas the axis on the bottom indicates the relative change of the variable with respect to the control boundary conditions. The *y*-axes show the relative change in the calculated particle diameter with respect to the original diameter, d_p = 30 nm.

The thermal accommodation coefficient, denoted by α_{T}, describes the efficiency of energy transfer during molecular collision in the heat conduction mechanism. Various values from 0.07 to 1.00 were reported in the literature. A larger value of α_{T} leads to a more efficient loss of energy to the surrounding atmosphere and, hence, a faster signal decay at the same collision rate [14,133]. α_{T} is a dimensionless coefficient and depends on temperature as well as on particle morphology [134]. Therefore, it cannot be directly measured in real systems. In this study, the control signal is simulated with a value of 0.25, and various values from 0.1 to 0.4 with 0.01 increments are tested for particle-size evaluation. Fig. 51a shows that a too small value of α_{T} results in smaller evaluated particle sizes because it causes the simulated signal decays to become too slow. To match the input data, this slow decay is compensated by a small particle size, hence faster decay, by the curve-fitting algorithm. Vice versa, for too large α_T values, too large particle sizes are returned. A 40% inaccuracy in α_{T} causes as a 20% inaccuracy in the evaluated results.

The bathgas temperature (Fig. 51b) is a physical property of the system. It affects both the radiative and the conductive heat transfer rates and it defines the initial temperature of the soot particles before the laser heat-up. Therefore, the peak temperature of soot and the evaporation rate also depend on the bathgas temperature. To understand how the particle-size evaluation is influenced by incorrect assumptions of the gas temperature, these mechanisms are investigated independently. During laser heating with a constant laser fluence, the peak temperature of the particles increases with increasing gas temperature. This slightly increases the radiative heat flux which remains, however, negligible compared to conductive cooling. For conduction, the bathgas temperature has competing effects. While increasing the gas temperature enhances the thermal conductivity and the heat capacity of air, and thus increases particle air energy transfer, the overall conduction-related heat flux reduces due to a smaller temperature difference ΔT between particle and surrounding gas. Additionally, depending on the laser fluence, the increased bathgas temperature may eventually cause the particle temperature to exceed the evaporation threshold and therefore causes additional energy loss. Fig. 51b shows that with increasing gas temperature at moderate laser fluence, the decrease in heat conduction due to a reduced ΔT is larger than the sum of enhancing effects in the other mechanisms. Therefore, smaller particle sizes are evaluated to compensate the reduced LII signal decay rate when higher gas temperatures are assumed. According to this evaluation, a 20% error in ΔT causes as a 20% error in the evaluated particle sizes.

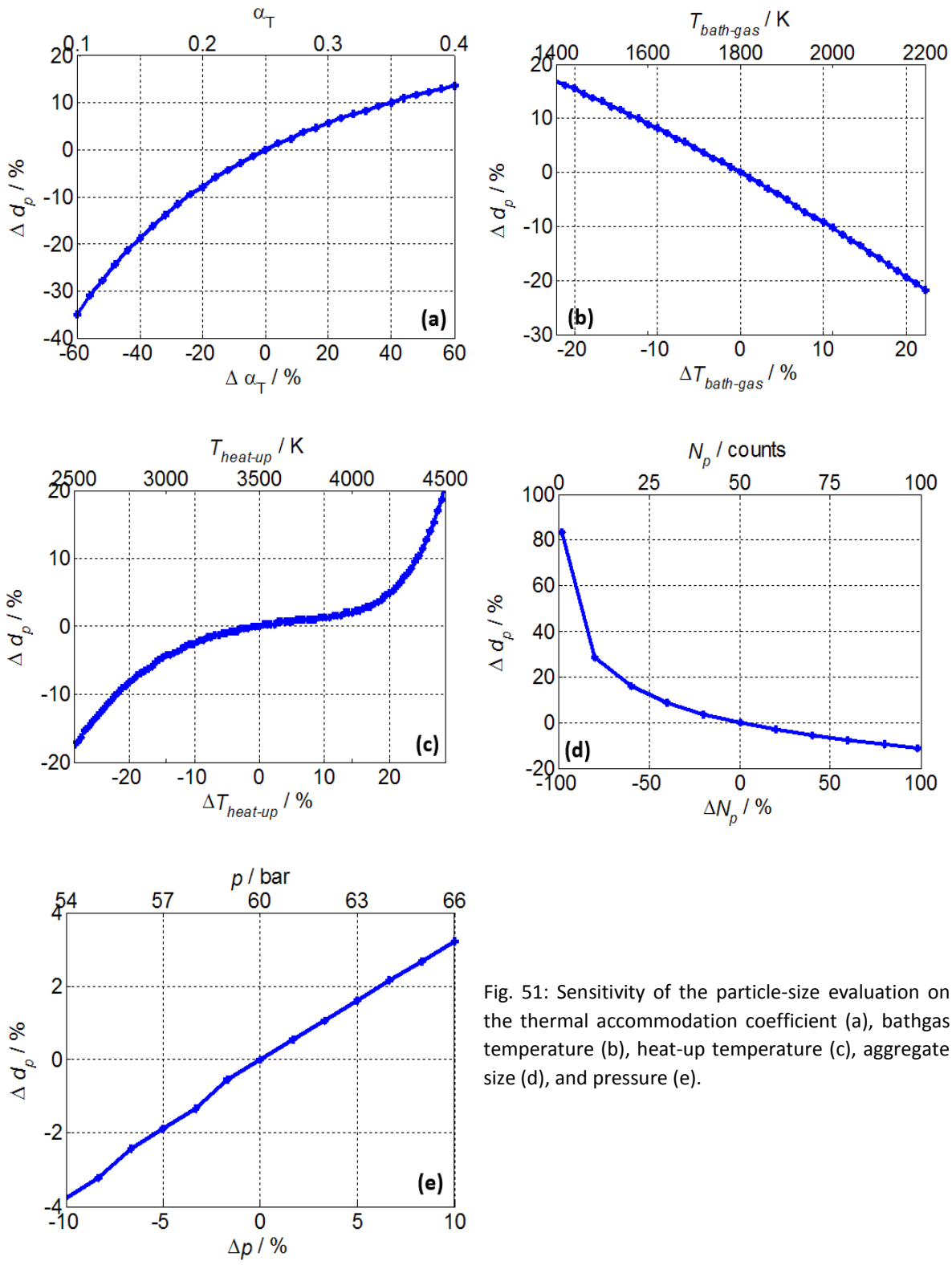

Fig. 51: Sensitivity of the particle-size evaluation on the thermal accommodation coefficient (a), bathgas temperature (b), heat-up temperature (c), aggregate size (d), and pressure (e).

The particle heat-up temperature (Fig. 51c) reached during the laser pulse depends on the laser fluence chosen for the experiment. As in the case of bathgas temperature, the signal decay and therefore

the size evaluation is influenced by the heat-up temperature via radiation, conduction, and evaporation. In all three heat transfer mechanisms, an overestimated heat-up temperature causes faster LII decay that then leads to the prediction of too large particle sizes. The sensitivity of the particle sizing to heat-up temperature is largest in the evaporation regime because the large heat loss encountered with evaporation. Fig. 51c shows that the heat-up temperature has the lowest sensitivity for moderate peak temperatures between 3400 and 3900 K. Tuning the laser fluence to this target temperature range minimizes the uncertainty in size evaluation for the case calculated here at 60 bar.

Soot aggregates can be described as random fractal structures. When modeling LII-signal traces, the laser absorption rate, the change in internal energy and the heat loss due to radiation are not affected by aggregation as long as the individual particles remain in the Rayleigh regime. The signal scales linearly with the number of primary particles within an aggregate, N_p, and hence the mass [29]. However, heat conduction is affected by aggregation. A primary soot particle within an aggregate cools down more slowly than an isolated one because collisions with gas molecules are reduced by the surrounding particles. This phenomenon is known as shielding. Fig. 51d shows that an underestimation of the N_p causes too fast simulated LII decays resulting in an overestimation of particle sizes. The greatest change occurs when switching in LIISim from isolated particles to the aggregate model. N_p, however, is a difficult parameter to measure. The variable range (1–100) investigated here is based on a statistical analysis of TEM measurements of thermophoretically sampled soot obtained from high-pressure combustion processes [95,110]. The ambient pressure is a significant parameter for the shielding-related change in heat flux [29].

The ambient pressure (Fig. 51e) is also a physical property of the system under investigation. In a combustion chamber it is spatially uniform and can be measured by pressure transducers. The pressure affects both conductive cooling and evaporation, while the latter effect is negligible. When the pressure is underestimated, a slower heat exchange, and hence longer signal lifetime is modeled. In such case, the curve-fitting compensates this slower decay by returning smaller particles. The deviation in the particle size was not greater than ±4% for an error of ±10% in pressure. Nevertheless, the pressure and the signal lifetime have a logarithmic relation (cf. section 6.1.4 and Fig. 60). Around 60 bar, the influence of pressure on particle sizing can be marginal whereas at pressures lower than 10 bar, small deviations can lead to large discrepancies.

Besides its direct effect, the pressure influences the sensitivity of the particle sizing to the other experiment and modeling parameters. To determine the effect of pressure on the influence of the bathgas temperature, the analysis shown in Fig. 51b was repeated at pressures from 1 to 80 bar. All

the other modeling parameters were kept constant. Fig. 52a shows that, as pressure increases, the sensitivity of the evaluation to the input data reduces. When the bathgas temperature is assumed 20% lower than the actual temperature, the error on the evaluated size is around 30% at atmospheric pressure whereas this error reduces below 15% at pressures above 60 bar. The same analysis is repeated for the heat-up temperature and shown in Fig. 52b. At atmospheric conditions, a 20% higher heat-up temperature can cause errors above 60%, whereas the same variation causes only 5% error at pressures above 40 bar. This reduction in the sensitivity can be attributed to the fact that at higher pressures the normalized LII signal decay traces of different particle sizes fall into narrower envelopes and curves resulting from different environmental conditions become closer.

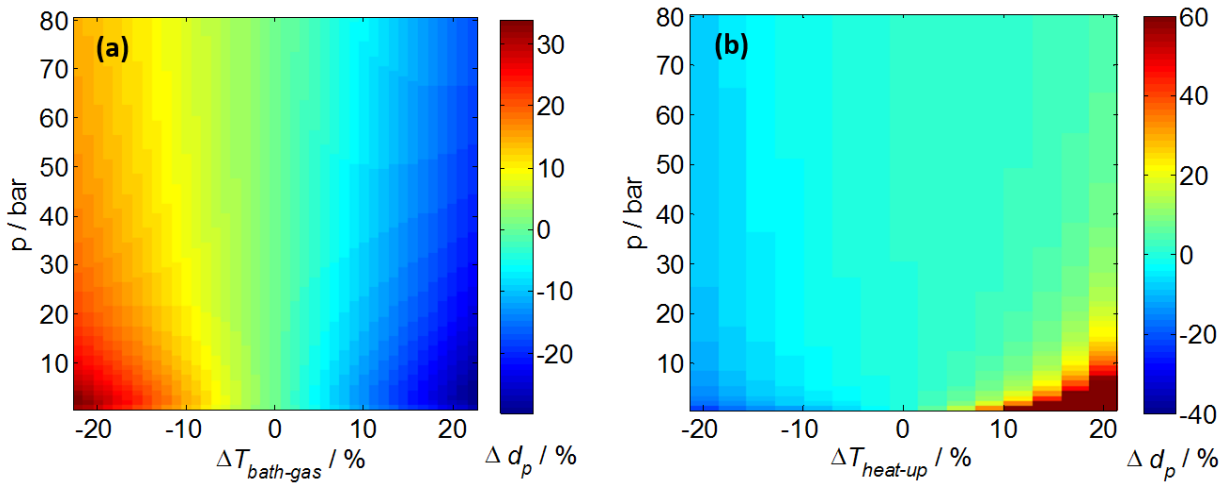

Fig. 52: Sensitivity of particle sizing to the bathgas temperature (a) and heat-up temperature (b) at various pressures.

6.1.2 Particle-size dependent heat-up temperature

Within the Rayleigh regime, $\pi d_{\mathrm{p}}/\lambda_{\mathrm{ex}} < 0.3$, (with λ_{ex} the laser wavelength) the energy absorbed by a particle depends on its volume [22]. Independent of the particle size, the same energy density is reached and all particles in a poly-disperse ensemble should reach a uniform heat-up temperature as long as no energy losses occur during heat-up. These losses, however, can be significant at high pressure. Recent studies [27,44] showed that the particle-size dependent energy loss during heat-up causes temperature differences among the different particle-size groups in the ensemble because small particles loose energy faster than larger particles. To quantify these deviations at 60 bar, simulations were performed for the evaporating and non-evaporating regime for particle diameters from 2 to 50 nm at conditions given in Tab. 1.

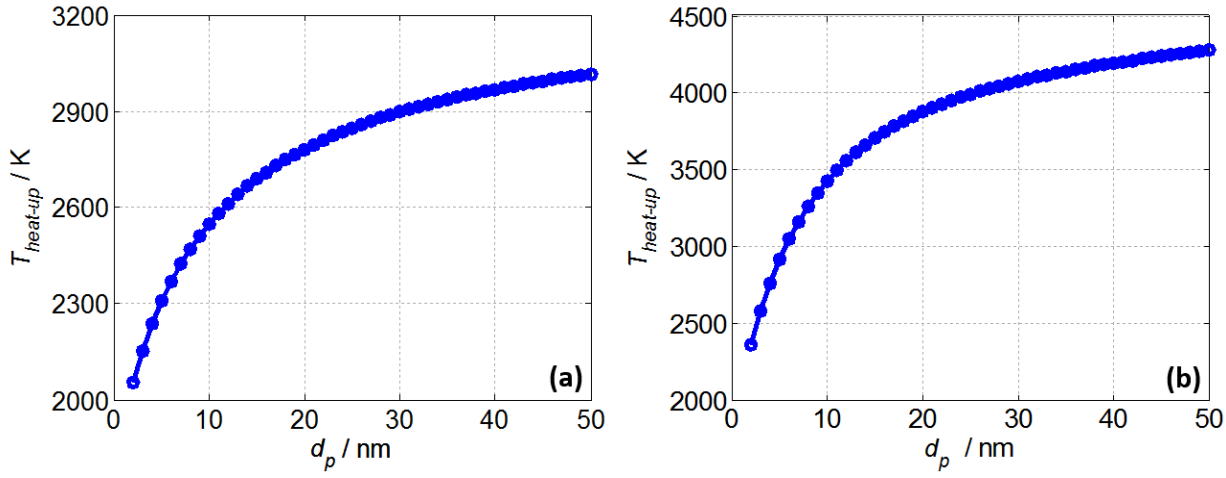

Fig. 53: Particle-size dependent peak temperatures, $T_{heat-up}$; (a) non-evaporating regime (0.08 J/cm^2), (b) evaporating regime (0.2 J/cm^2).

For low laser fluences (Fig. 53a) the peak temperature difference between the 10 and 40 nm particles is ~400 K while for the high-fluence regime (Fig. 53b) it is above 600 K. As shown in section 6.1.1, such deviations in heat-up temperature can have dramatic effects on particle sizing. This effect also limits the reliability of the pyrometric determination of heat-up temperatures that are used for two-color LII measurements where the modeling of the laser absorption is omitted and the measured temperature is used as an input for the simulation [29,44,56,97,135]. In particle-size measurements that include heat-up modeling, the variation in peak temperatures is automatically considered because a unique peak temperature, hence a peak LII signal, is calculated for each trace with the net energy gain. Nevertheless, uncertainty still remains for poly-disperse soot where the acquired experimental signal trace (or signal ratio in particle-size imaging) consists of radiation from various particle-size groups. Uncertainties related to poly-dispersion are discussed in section 6.1.6.

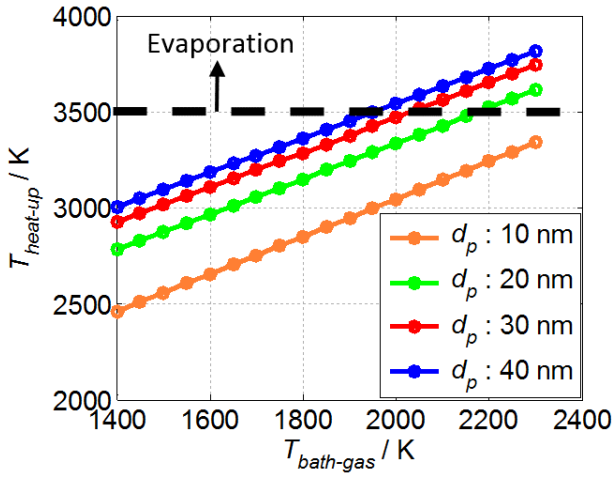

Fig. 54: Dependence of particle heat-up temperatures on bathgas temperatures for various particle sizes.

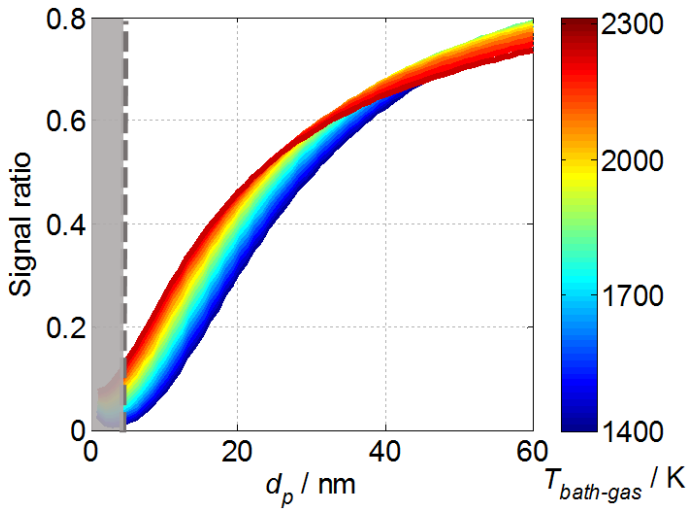

Fig. 55: Look-up table of d_p vs. signal ratio for gas temperatures, T_{bathgas}, between 1400 and 2300 K with a laser fluence of 0.15 J/cm^2.

The relation between particle size and peak temperature can also influence evaporation. For a given laser fluence, depending on the bathgas temperature, the peak temperature of small particles may remain below the evaporation threshold whereas larger particles may start to evaporate. The dependence of the peak temperature to the bathgas temperature for different diameters are presented in Fig. 54. The simulations are performed with the parameters shown in Tab. 1. 10 nm particles cannot reach evaporation regardless of the bathgas temperature in the investigated temperature range. On the other hand, 40 nm particles reach the evaporation threshold for gas temperatures above 2000 K eventually causing an accelerated heat loss for larger particles and affecting the LII signal trace after the peak, thus the sensitivity of the particle sizing on the various parameters changes for different size groups. This influence on the cooling phase can be seen in Fig. 55, where the look-up table of the particle size vs. signal ratio is given for gas temperatures between 1400 and 2300 K with 100 K increments and for particle sizes between 1 and 60 nm. The remaining parameters are those from Tab. 1. For the analysis, a delay of 5 ns between the two detection gates is considered. In the particle-size domain smaller than 35 nm, for a given signal ratio, larger particle sizes are determined at smaller gas temperatures. Nevertheless, low and high gas temperature curves show different characteristics: For large particles at high gas temperatures the ratio of the two time-gated signals falls below the simulations for lower gas temperature. This is related to a combined effect of the onset of evaporation and particle-size dependent peak temperatures. Results for particle sizes below 4 nm are shaded because they are beyond the limit of particle sizing with the conventional signal simulation provided by LIISim. To avoid the complications of the particle-size dependence on the peak temperature, Charwath et al. [44] proposed faster short-pulse laser heating to temporally separate from particle cooling. However, Michelsen [136] reported that rapid heating with conventional picosecond lasers brings

new complications to the particle sizing and requires new modeling approaches. Unconventional laser sources with pulse durations of ~1 ns would potentially be a good compromise, but they are not readily available and have not yet been explored for LII.

6.1.3 Effects of laser attenuation

Sooting high-pressure flames provide strongly absorbing environments that can affect laser-based diagnostics. Attenuation of the laser beam causes a spatial variation in laser fluence along the beam propagation direction. Strategies that rely on ratioing of two signals often reduce or avoid the dependence of the signal of interest on laser fluence. While this works with strategies where the signal linearly depends on the laser fluence, such as two-color laser-induced fluorescence methods [137], it is not applicable to LII because the fluence affects the signal and its decay characteristics in multiple ways. The magnitude of laser attenuation depends on the optical density of the soot cloud, KL, which is linearly proportional to the soot volume fraction along the laser path. A comprehensive explanation of laser attenuation in sooty environments is given in Refs. [47,138]. Laser attenuation eventually causes a spatial variation in the heat-up temperatures of the particles within the imaged area. Fig. 56 shows the dependence of the peak temperature on laser fluence. Simulations were performed for Tab. 1 conditions. The variation of $T_{\text{heat-up}}$ with particle size at the low-fluence limit and the slopes observed for the investigated particle sizes are due to the dependence of the energy-loss rates during the heat-up on the particle size (cf. section 6.1.2). The influence of laser fluence on the peak temperature is more significant in moderate or low-fluence LII. In the high-fluence regime (>0.25 J/cm^2) the sensitivity decreases due to the very strong heat loss through evaporation.

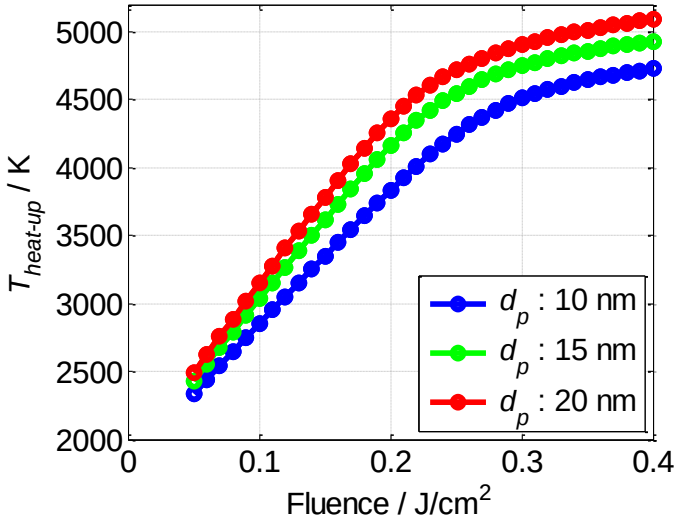

Fig. 56: Particle peak-temperature as a function of laser fluence for 10, 15, and 20 nm particle diameter.

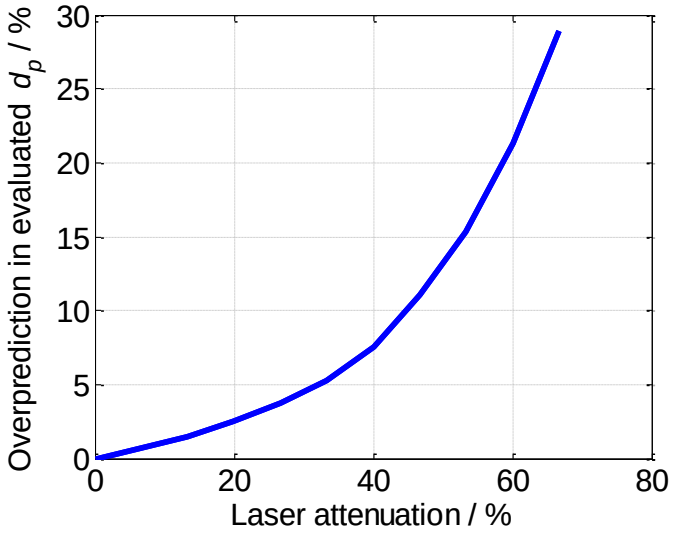

Fig. 57: Error in the evaluated particle size as a function of laser attenuation (conditions of Tab. 1).

Fig. 57 shows the effect of laser attenuation on the evaluated particle size for 30 nm particles for Tab. 1 conditions. When laser attenuation is not taken into account, the heat-up simulation calculates too high peak temperatures resulting in too fast signal decays. To compensate, the curve-fitting routine yields too large particles. To eliminate the attenuation-related uncertainty, the effective laser fluence at each pixel should be known. Although it is relatively easy to measure the total attenuation, it is not trivial to measure the fluence gradient along the soot environment. To achieve this, temperature gradients of heated soot particles can be measured via two-color pyrometry imaging and resulting temperature can be used to calculate the effective laser fluences. Nevertheless, the gas temperature and particle-size variations also affect the peak temperature as previously described which reduces the precision of the fluence measurements (For two-color pyrometry imaging of heated particles, cf. section 6.1.7).

6.1.4 Gating strategies

Optimizing timing and width of the two detector gates is crucial to optimize the sensitivity of the signal ratio to particle size and to maintain good signal-to-noise ratios. Both images must be acquired during the signal lifetime and record information at different points in time. Three gating strategies are investigated in this section:

Reference strategy

In order to understand the effect of the gate width on the determination of particle sizes, the signal-ratio method is investigated analytically. In an experiment where heat conduction is the dominant

heat transfer mechanism, the LII signal of a mono-disperse class of particles, either isolated or aggregated, decays nearly exponentially [31]. With this assumption, the approximated signals collected by two gates with identical width can be calculated as

$$I_1 = \int_0^{\Delta t} e^{-t/\tau} dt = -\frac{1}{\tau}\left(e^{-\Delta t/\tau} - 1\right) \quad (24)$$

$$I_2 = \int_{\delta}^{\delta+\Delta t} e^{-t/\tau} dt = -\frac{1}{\tau} e^{-\delta/\tau}\left(e^{-\Delta t/\tau} - 1\right) \quad (25)$$

Where Δt is the gate width, τ is the lifetime and δ is the delay for the beginning of the second gate with respect to the signal peak. The ratio *R* of the two signals,

$$R = \frac{I_2}{I_1} = e^{-\delta/\tau} \quad (26)$$

is independent on the gate width. Nevertheless, to minimize the detection of background signal (e.g., flame luminosity), the gates should be as short as possible. On the other hand, the camera gate should be long enough to collect sufficient signal to minimize the signal-to-noise ratio. In recent experiments, 15 ns were identified as the shortest gate that yields sufficiently strong signal at conditions comparable to Tab. 1, and therefore, this value is taken as the base gate width in this study. Nevertheless, depending on the camera, the optical setup, the laser fluence, the laser sheet thickness, and the soot volume fraction, optimum gate widths may change.

To optimize the delay δ between the detection gates for highest sensitivity to particle size, further calculations are performed. The best sensitivity is given in the case with the strongest variation of the signal ratio vs. particle size. Therefore, the dynamic range, *DR*, of a signal-ratio curve is evaluated over the entire range of particle sizes. Based on Eq. 26, *DR* can be calculated for a given δ as

$$DR = R(\tau_L) - R(\tau_S) = \exp{}^{-\delta}/_{\tau_L} - \exp{}^{-\delta}/_{\tau_S} \quad (27)$$

where the subscripts *L* and *S* represent the largest and smallest particles in the measurement domain, respectively. *DR* is 0 at $\delta = 0$ and it increases with increasing δ, since τ_L is larger than τ_S. However, as δ goes to infinity, *DR* converges to 0. Hence, *DR* reaches a maximum at a certain δ (δ^*, optimum delay) and this value can be calculated from the zero value of the derivative of *DR* with respect to δ:

$$\frac{dDR}{d\delta} = -\frac{1}{\tau_L}\exp{}^{-\delta^*}/_{\tau_L} + \frac{1}{\tau_S}\exp{}^{-\delta^*}/_{\tau_S} = 0 \quad (28)$$

From Eq. 28, the optimum delay for the second gate is

$$\delta^* = \left(\ln(\tau_L) - \ln(\tau_S)\right)/\left(\frac{1}{\tau_S} - \frac{1}{\tau_L}\right) \quad (29)$$

Eq. 29 indicates that the optimum delay yielding the highest sensitivity is solely related to the lifetime of the LII signal which depends on various parameters and needs to be simulated. Therefore, to determine δ^* for the conditions shown in Tab. 1, a model-based analysis was performed. For the first analysis the starting time of the first gate was fixed to the peak signal to confine the input data to the cooling part of the LII signal where the simple exponential approximation is valid (cf. Eq. 24 and 25). Delaying the first gate leads to a loss in signal and the signal contribution from the smallest particles will be reduced. Advancing of the first gate with respect to the peak signal will be considered later. This analysis is targeted to identify the optimum timing of the second gate that provides the highest sensitivity to particle sizing and that provides sufficient signal. Therefore, the second gate is swept along the modeled data library with a delay from 1 to 20 ns with respect to the first gate. A look-up curve that relates the signal ratio to particle size and thus indicates the sensitivity of the measurement strategy is created for each delay δ (cf. Fig. 58a).

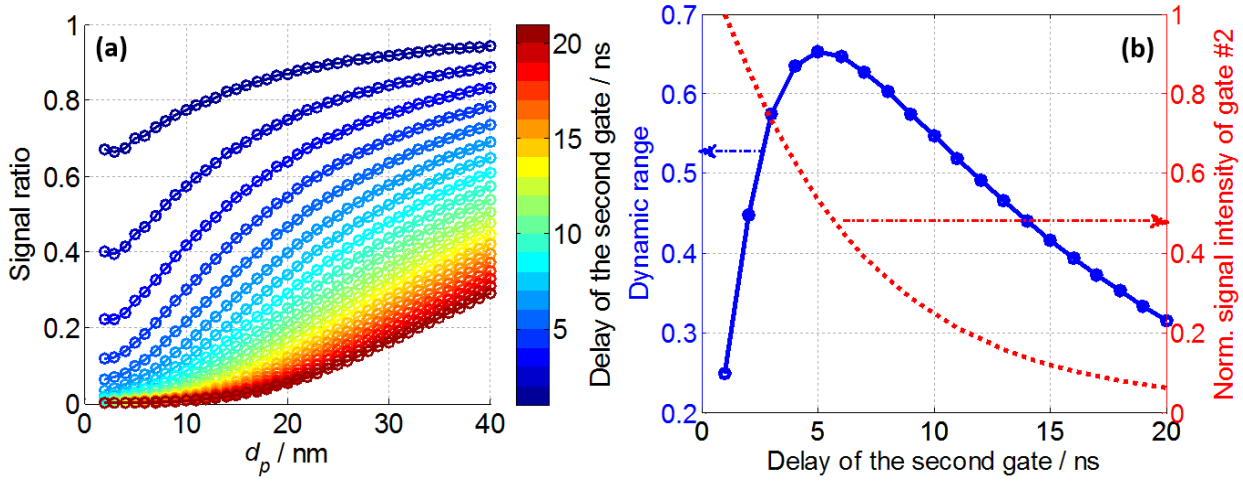

Fig. 58: (a) Look-up curves for various delays of the second gate δ with fixed 15 ns gate width and the first gate starting at the signal peak, (b) dynamic range of signal ratios for particles from 4 to 40 nm diameter for different delay scenarios (solid blue curve) and the integrated signal intensities with the second gate for an average expected particle diameter of 20 nm (dotted red curve). The signal-intensity curve is normalized to the signal at δ = 1 ns.

The dynamic range *DR* of each look-up curve is calculated for the particle-size range expected for engine-like combustion (4–40 nm). The solid blue curve in Fig. 58b shows that a delay of 5 ns yields the largest dynamic range, (signal ratio varies in the 0.06–0.73 range between 4–40 nm) hence the highest sensitivity is reached for Tab. 1 conditions. Remembering the 15 ns width for both gates, this results in a 10 ns overlap of both gates. The reason of the reduction in sensitivity at longer delays is that small particles cool down to the ambient temperature within the delay time and thus, the second gate cannot capture any signal from these particles anymore. This can be seen through the decreasing slopes of the look-up curves for increasing delay in the particle domain smaller than 10 nm diameter

in Fig. 58a. In contrast, when the delay is too short, both images capture too similar information. Therefore, the ratio of the images converges to 1 and the sensitivity is reduced.

While searching for the maximum dynamic range *DR*, it is also important to consider the signal intensity in the delayed gate. Depending on the experimental parameters (see above), too long delays lead to insufficiently weak signal and thus increased signal-to-noise ratios. The red dotted curve in Fig. 58b shows how the signal intensity declines relative to a 1 ns delay scenario for a particle diameter of 20 nm (expected average particle size). At a delay of 5 ns, which was calculated as the delay yielding the largest dynamic range, the theoretical signal intensity in the second gate is 53% compared to the case with the minimum delay (1 ns). Concerns, however, are related to the nominal signal intensity (photon counts) and the actual signal-to-noise ratio. The nominal signal changes from system to system, and it is therefore not easy to speculate a universal relative threshold that still provides acceptable signal. Ideally, the signal strength in both channels should be comparable. In this study it is decided that second-gate signals lower than 5% of first-gate signals are considered too low. The sections of the signal ratio curves (in Fig. 58a) that are below 0.05 are therefore not taken into account.

The influence of the ambient pressure on δ^* is investigated by evaluating the above-mentioned maximum points on dynamic range curves which are created with unique libraries for different pressures as shown in Fig. 59. Optimum delay δ^* is plotted on a log-scale. For each library the remaining conditions from Tab. 1 are used. When the pressure increases, the lifetime of the LII signal and therefore, δ^* decreases as shown in Eq. 29.

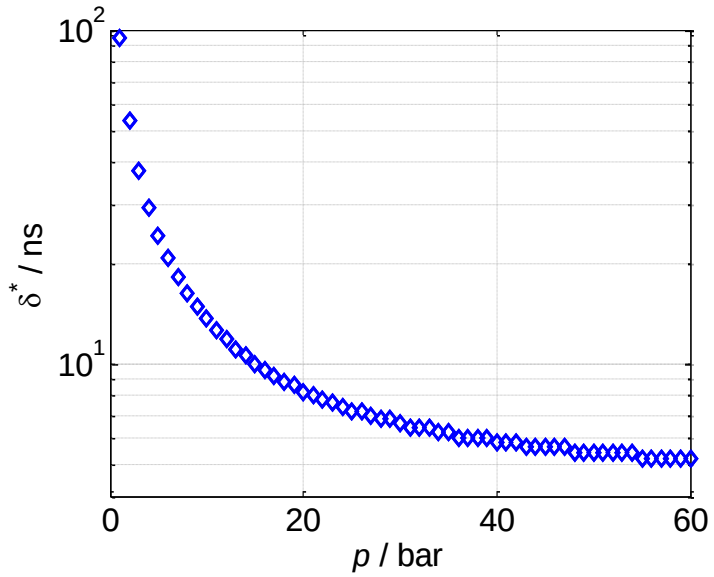

Fig. 59: Optimum delay δ^* for the second gate at various ambient pressures (The first gate starts at the signal peak)

It can be also seen that the rate of change in δ^* reduces with increasing pressure. In conduction cooling, the heat flux from particle to the bathgas is proportional to the pressure. Thus the lifetime is inversely proportional to the pressure. The relation between signal lifetime and pressure for soot aggregates with 30 nm diameter particles at Tab. 1 conditions is shown in Fig. 60. After the first few ten bar, the lifetime shows an asymptotic behavior and does not change significantly with increasing pressure. Therefore, from 20–60 bar, δ^* changes only by 3 ns.

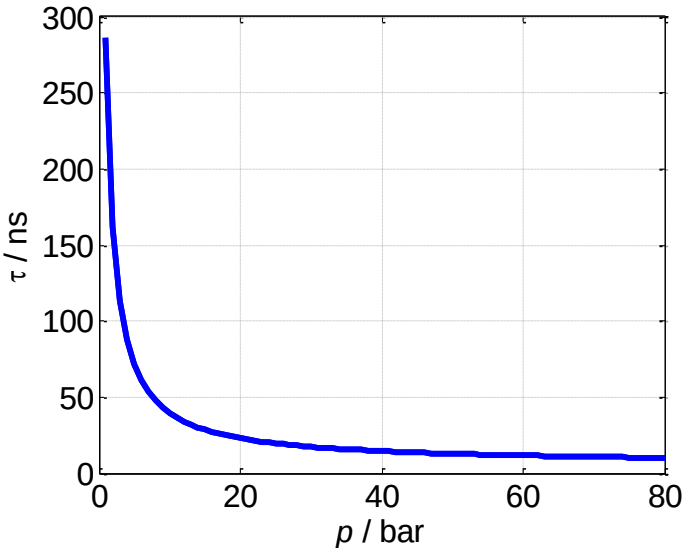

Fig. 60: LII-signal lifetime as a function of pressure.

Gate-advancing strategy

In the previous strategy the second gate always provides much weaker signal than the first gate. Shifting the second gate to early times in contrast reduces the sensitivity because of a large overlap of the detected signals. An alternative strategy is advancing the first gate to start before the signal peak is reached. This allows to increase the signal in both gates with a limited effect on the sensitivity. Up to a certain advancing time the sensitivity slightly reduces but with further increasing of advancing time, the sensitivity recovers and exceeds its initial value. Obviously, it does not make sense to advance the first gate to times before the onset of the laser pulse; therefore, the discussion is limited to advancing times between –7 and 0 ns before the signal peak.

The theoretical analysis of these cases requires model libraries that include the simulation of the heat-up phase (cf. section 6.1.2). In contrast to the LII-signal decay, the slope of the LII signal on the heat-up side is almost identical for all particle sizes. The relative contribution of signal from small particles therefore increases when advancing the gate. Fig. 61a shows the variations in signal intensity of the first gate (blue curves) and the second gate (red curves) at the respective δ^* as a function of advancing times for 4 nm (dashed curves) and 40 nm (solid curves) particles. Each curve is normalized to the

respective value without advancing the gate. Advancing the first gate increases the signal in the first gate (up to 70 and 21% for 4 and 40 nm particles, respectively). For each position of the first gate, the second gate is swept up to a delay δ of 20 ns relative to the first gate. For each position of the first gate, there is a unique "best" δ^* derived from the maximum of the dynamic-range curves in Fig. 61b. The relative signal increase in the second gate with respect to the original case is substantial (up to 1480% and 52% for 4 and 40 nm particles respectively). Advancing the first gate up to –4 ns slightly reduces the sensitivity of particle sizing (maximum dynamic range is reduced by 5%). However from –4 to –7 ns, the sensitivity starts to increase (maximum dynamic range reaches 8% more of the original case at –7 ns advancement).

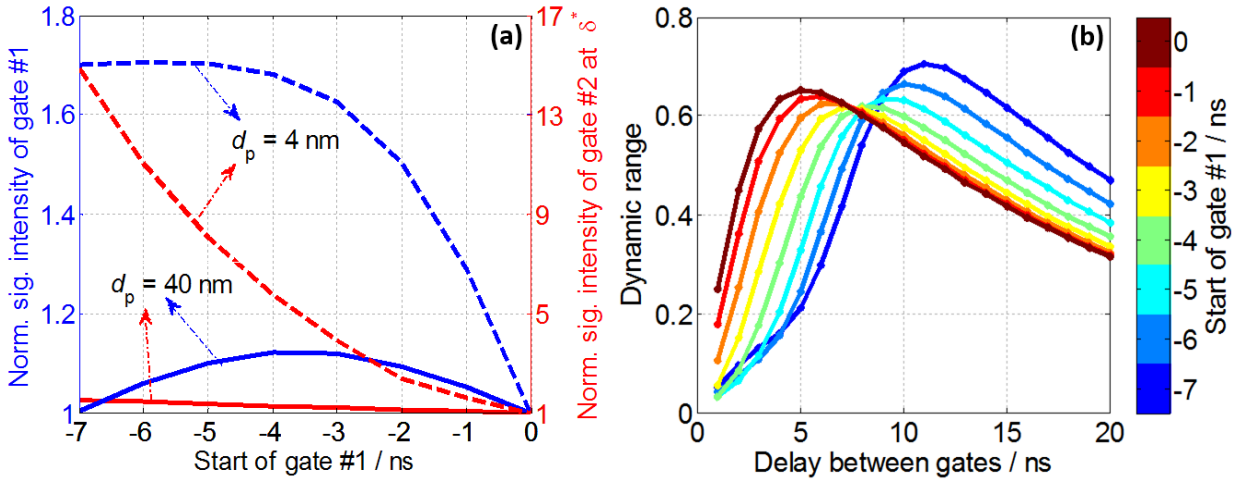

Fig. 61: (a) Integrated signal intensities with both gates at various advancing times for two different particle sizes. Each curve is normalized to the respective value without advancing the gate. (b) Dynamic range DR of the signal ratio R for particles from 4 to 40 nm diameter with advanced first gate.

With increasing time advancing of the first gate, the relative increase in signal intensity in the second gate (at δ^*) is substantially larger than in the first gate for small particles. Nevertheless for larger particles, the signal intensity increase in both gates is comparable. Therefore, the signal ratio increases more for small particles than for large ones and the look-up curves become flatter (the dynamic range decreases). This continues up to –4 ns. At an advancing time greater than –4 ns, the integrated signal intensity in the first gate starts to decrease for larger particles with increasing time advancing whereas it keeps rising in the second gate (cf. Fig. 61a) due to shifting towards the peak. This leads to a rapid increase in the signal ratio at the large particle classes. In this time range the increasing signal ratio at the small particle classes remains marginal relative to the increase in large classes. As a result, the dynamic range, and hence, the sensitivity of particle sizing, increases slightly from –4 to –7 ns (cf. Fig. 61b). The analysis shows that advancing of the first gate to the start of laser heating (–7 ns) and a delay of 11 ns between the two gates is the optimal gate strategy. This strategy enhances the signal-

to-noise ratio as the signal intensity in both channels increases. It also increases the sensitivity of particle sizing by 8% with respect to the original case without gate advancement.

Asymmetric gating strategy

A further enhancement of the signal-ratio based particle sizing is possible by using asymmetric gate widths. For the delayed gate, the original 15 ns may be too short to collect signal leading to poor signal-to-noise ratios. Starting with the optimum strategy mentioned above (first gate at –7 ns, 11 ns delay between both gates), the width of the second gate is extended from 15 to 55 ns with 1 ns increments. For each gate width, a look-up curve is created (Fig. 62). The extension of the second gate has no impact on the signal ratio of the small particle classes because the original 15 ns duration was sufficient to capture all the signal information of these small particles. For larger particles, however, the signal increases when increasing the gate width. This leads to an increase of the signal ratio for the large particle classes, hence an increase of the particle-size sensitivity. After a certain gate width, the second-gate signal becomes stronger than the first-gate signal and the ratio *R* exceeds unity.

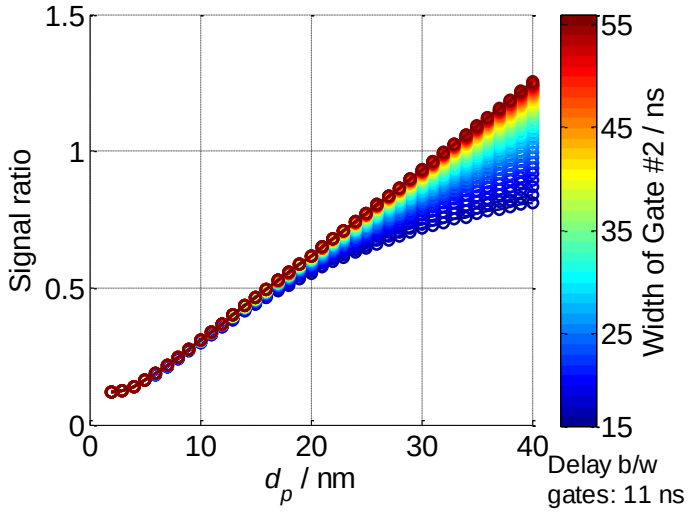

Fig. 62: Look-up curves for asymmetric gate widths. The width of the second gate is extended from 15 to 55 ns with 1 ns increments. The first gate is fixed to –7 ns and has a constant 15 ns width. The second gate is fixed to 11 ns after the first gate. The sensitivity increases with increasing gate width.

By extending the second gate from 15 to 35 ns, the dynamic range and hence the sensitivity increase by 50%. Fig. 62 shows that the further effects when extending the gate from 35 to 55 ns (from yellow to dark red) are marginal. In contrary, such long gates might negatively impact the accuracy because of the increasing contribution of background (e.g., flame luminosity).

After all, the ultimate strategy can be defined as: The first gate should be advanced to the start of particle heating (–7 ns in this study). The width of the second gate should be about twice as long as the first gate (here: first gate: 15 ns, second gate: 35 ns) and it should start 11 ns after the first one.

As previously explained, all these nominal timing values (given here for the conditions given in Tab. 1) depend on the experimental conditions.

6.1.5 Effects of timing jitter

In practical experiments jitter might occur between the laser pulse and the gated signal detection. Due to the short LII signal lifetime at high pressure, even a small jitter can cause considerable errors. For the analysis, the 5 ns delay between the two detection gates is considered fixed and it is assumed that the laser is the source of the jitter. The effect of shifting the laser pulse relative to the detection event by –4 ns up to +4 ns was simulated with 0.5 ns increments (positive values: Laser fires later than expected). For each time-shift a new look-up curve is created and for a given "true" particle size of 30 nm an "evaluated" particle size is determined by using the original look-up curve without jitter.

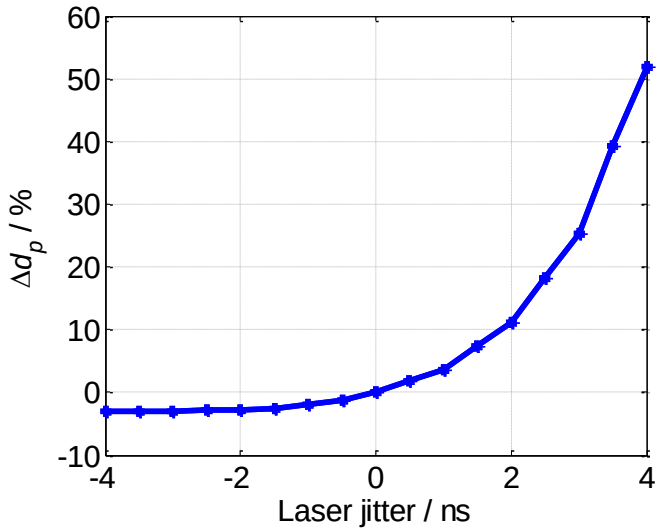

Fig. 63: Effect of laser timing jitter with respect to camera gates on the evaluated particle size; the delay between the two gates is fixed.

Fig. 63 shows the strongly asymmetric effect. With a positive jitter, the first camera gate starts before the signal peak leading to a signal loss relative to the second gate, thus increasing the gate #2/gate #1 ratio resulting in an overprediction of the particle size. A +2 ns jitter leads to an overprediction by 10%. With a negative jitter both detection gates are shifted into the range of decaying signal. In this case, smaller signal ratios and an underpredicted particle size are determined. Compared to the positive jitter, the discrepancies associated with the negative jitter are marginal. This is because the jitter has a similar effect on both gates and shifting along the nearly exponential decay; the gate ratio is better preserved. Nevertheless, this analysis does not consider the influence of the reduced signal-to-noise ratio when the jitter reduces the overall signal intensities. With negative laser jitter, the LII signal can decrease drastically in both channels.

If jitter cannot be fully avoided for any reason, to minimize jitter-related uncertainties a temporally-resolved acquisition working simultaneously with the imaging system can be implemented. By reading the actual laser and camera timings, identical delays can be taken into account when creating the look-up curves. By this means, measured and simulated signal ratios will be related to the same LII signal theoretically. Such evaluation algorithm will be effective only if the heat-up modeling is included in the signal library. When the absorption part of the LII signal is missing, the gate convolution on the model library with positive laser jitter encounters zero signal on the left side of the peak signal, whereas, on the experiment side, cameras still collect strong signal during the heat-up phase.

6.1.6 Influence of poly-dispersity

Heat conduction is the dominant cooling mechanism of soot particles at high pressure heated below the evaporation temperature. Along this cooling, the decay rate remains unchanged for a mono-disperse sample and therefore it can be approximated by a single-exponential decay. In a poly-disperse ensemble, each size group has a unique LII signal decay rate. During a measurement, the signals of these different groups superimpose resulting in a deviation of the acquired signal from the single-exponential decay. The relative contribution of each size group is linearly proportional to its relative soot volume fraction. In a particle-size evaluation with the conventional time-resolved entire signal fitting approach, additional information about the different size groups can be extracted by using a pre-assumed distribution [27]. However, it should be noted that it is generally challenging to fit poly-disperse distributions to LII signals due to the fitting problem being ill-posed [28,62]. Instead, the signals can be fitted with mono-disperse model signals and therefore the evaluated result for the signal acquired from the poly-disperse soot ensemble is an averaged mono-disperse equivalent mean particle size. Comparisons with TEM measurements showed that the mono-disperse equivalent size is always larger than the count median diameter of the poly-disperse TEM distribution, due to the fact that fitting with mono-disperse assumption biases the average results towards larger sizes [62]. The reason of this bias can be attributed to the dominance of the contribution of the large particles to the collected signal due to their longer and stronger incandescence as stated above. At high pressure, the particle-size dependent peak temperature (cf., section 6.1.2) causes additional bias towards the larger sizes since their contribution increases with temperature to the fourth power. The difference in the magnitude of the signal can be seen in Fig. 64 with LII curves modeled for the conditions in Tab. 1.

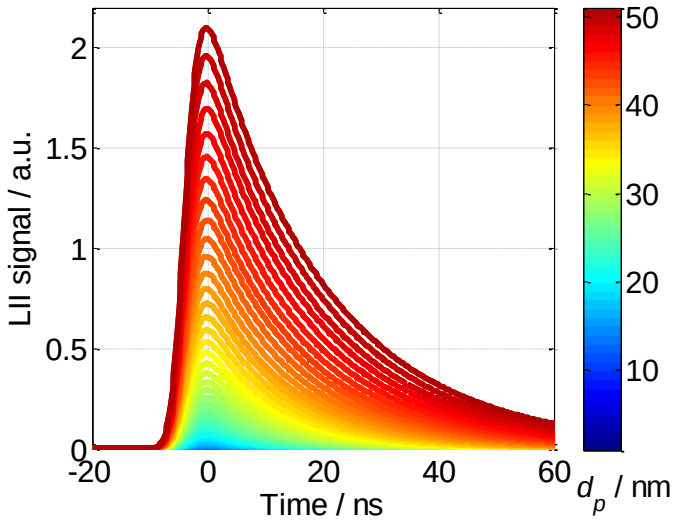

Fig. 64: LII signal traces for particles of different size. The magnitude of the signal is proportional to the third power of the particle diameter and fourth power of its temperature.

When sizing particles using the ratio of two gated signals, decay rates are not directly accessible and the signal interpretation results from the comparison with pre-calculated look-up tables. These are based on signal libraries that are created from simulations for the behavior of mono-disperse soot. The evaluation of the signal acquired from poly-disperse soot again yields averaged mono-disperse equivalent mean particle sizes. In this section, the magnitude of this bias towards larger sizes based on the signal-ratio method is investigated for the conditions shown in Tab. 1. Fig. 65a shows lognormal soot particle-size distribution functions (related to the respective particle volume) for three different counter mean diameters, d_{cmd} = 10, 20, and 30 nm, but with identical geometric width, $\sigma_{\mathrm{g}} = 1.4$, and each data point on the curve represents the probability density of a 1 nm-wide bin. Using these distribution functions and the particle-size-dependent signals from Fig. 64, LII signal traces for the respective poly-disperse ensembles were calculated. After applying the convolution with the gate timings shown in section 6.1.4, an averaged mono-disperse equivalent mean particle size was evaluated from the look-up tables in Fig. 2 and shown as vertical dash-dotted lines. By using the same methodology, in Fig. 65b, the bias towards larger sizes are shown for particle-size distribution functions with σ_{g} = 1.2, 1.4, and 1.6 with identical d_{cmd} at 20 nm.

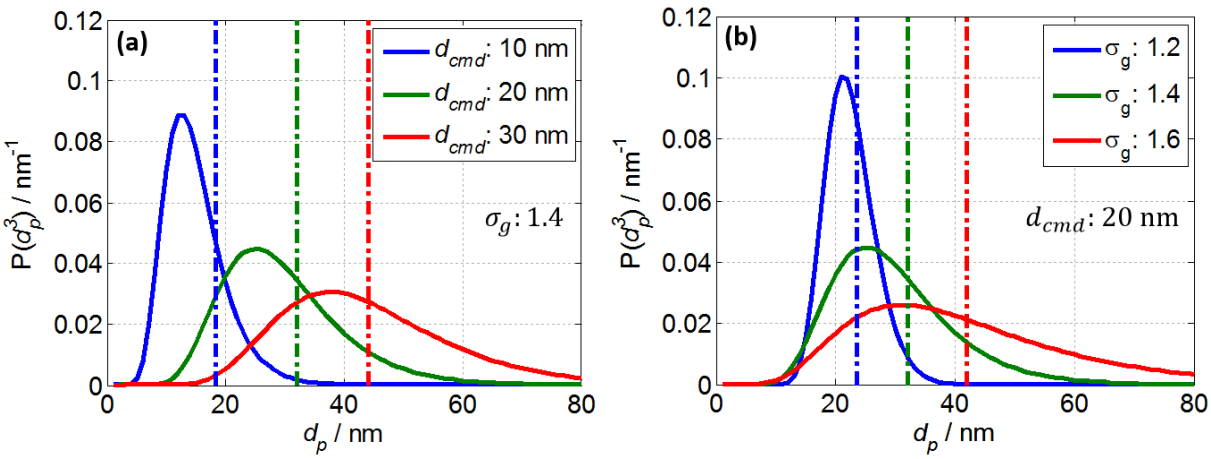

Fig. 65: (a) Lognormal distribution functions of particle sizes (related to soot particle volume) for three count mean diameters; fixed geometric width at 1.4, (b) lognormal distribution functions of soot particle sizes for three different geometric widths; with d_{cmd} = 20 nm. Vertical dash-dotted lines show the mono-disperse particle size evaluated by the signal ratio method for the LII signal input of soot ensembles having the distribution function with the respective color.

In all cases, the evaluated mono-disperse equivalent mean particle sizes are larger than the mean of the input distribution. In a lognormal distribution, the weight of larger particles in the probability density function increases with the increasing lognormal mean. This can be seen in Fig. 65a with the extending tail of the distribution for larger d_{cmd}. As a result, the bias in the evaluated particle size increases because the relative contribution of the small particles to the ensemble signal is lower than the larger ones. Fig. 65b shows that the bias is getting smaller for narrower distributions. Nevertheless, it should be noted that the magnitude of the bias in the signal-ratio method directly depends to the delay for the second gate as shown in section 6.1.4. As the delay increases, the contribution of smaller particles in the second gate further decreases and the bias increases.

To investigate the additional bias at high pressures due to the particle-size dependent peak temperature, seven different signal libraries were created with ambient pressures from 1 to 60 bar with Tab. 1 conditions. From each library, a poly-disperse signal was created by using the lognormal distribution with d_{cmd} = 15 nm and σ_g = 1.5. For each pressure the optimum delay for the second gate shown in Fig. 59was used and the mono-disperse equivalent mean particle size with the signal ratio were calculated, shown in Fig. 66. The temperature difference between small and large particles increases with increasing ambient pressure. Therefore, at higher pressure the relative contribution of the smaller particles in the ensemble poly-disperse signal reduces causing the bias of the mono-disperse equivalent mean particle size to increase.

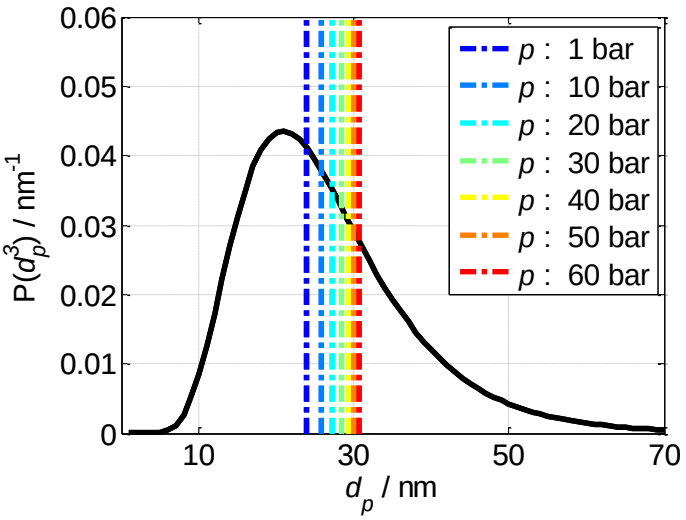

Fig. 66: Bias of the mono-disperse equivalent mean particle size (vertical dash-dotted lines) towards larger particles at different pressures. The distribution function of soot particle volume is a lognormal with d_{cmd} = 15 nm and $\sigma_g = 1.5$.

6.1.7 Gating effects on two-color pyrometry

In cases where the laser fluence changes locally, e.g., because of laser attenuation, it is advantageous to measure the spatial distribution of heat-up temperatures which allows to consider the local conditions during data evaluation. Two-color pyrometry imaging of the particle temperature during laser heating can provide the required information. At high pressure, however, a compromise must be found: The short lifetime of the incandescence signal requires an as short as possible detection exactly at the peak to avoid biasing of the measurement towards lower temperatures. On the other hand, sufficient signal must be detected for low-noise measurements, which prevents the use of short gates. Furthermore, jitter of the laser timing relative to the detector gates could strongly affect the measurement when the gates are very short. To analyze the influence of the gate lengths and the measured apparent peak temperature, time-resolved temperature information is extracted from the control LII signal with 30 nm particle size with the boundary conditions given in Tab. 1. The expected signal intensities within two detection bands centered at 425±15 and 676±14.5 nm are calculated using Planck's equation [60] (cf. Fig. 67a).

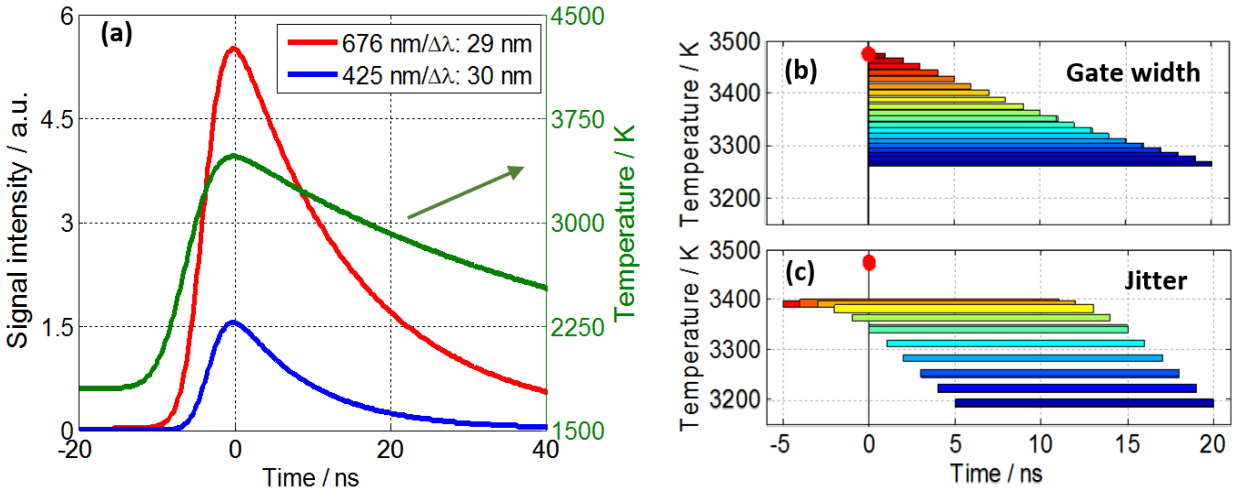

Fig. 67: (a) Time-dependent temperature and thermal emission at 425±15 and 676±14.5 nm calculated for the respective temperature, (b) evaluated apparent temperature for gate widths from 1 to 20 ns, the instantaneous peak temperature is shown with the red dot, (c) evaluated apparent temperature with a fixed 15 ns gate width for jitter from –5 to +5 ns.

To investigate the effect of the time-averaging within realistic camera gates, the calculated thermal emission for the two detection bands is convoluted with gate width from 1 to 20 ns (starting at the signal maximum). The resulting signal ratio is then evaluated based on Planck's law. Fig. 67b shows the evaluated apparent temperatures on the *y*-axis for each gate width. The red dot shows the instantaneous peak temperature. As the gate width increases, the apparent peak temperature reduces. For a 15 ns gate, the evaluated temperature is underpredicted by roughly 200 K. Fig. 67c shows the effect of laser jitter up to ±5 ns for a gate width of 15 ns. Each bar shows a different jitter scenario and the actual timings can be read on the *x*-axis. If the gates start at a point before the signal peak, the apparent temperature is closer to the actual temperature. In a case where detection starts after the peak, the particles may already have lost some part of their energy and therefore, the calculated temperature can be substantially lower. To minimize the jitter-related uncertainty in an experiment, the gating timing can be set to a couple of nanoseconds before the signal peak so that the temperature measurement will be less sensitive to timing. This will also reduce the bias of the method towards lower temperature.

6.1.8 Conclusions

The applicability of laser-induced incandescence particle size for high-pressure conditions (such as Diesel combustion) was studied based on a detailed numerical analysis. At high pressure the LII-signal lifetime is short because of efficient conductive cooling of the laser-heated particles. Various gating strategies were compared. To deduce the primary particle size from LII imaging, a look-up table

method based on the ratio of two pre-calculated time-gated signals was used. This method was evaluated by applying the data evaluation strategy to simulated signal traces where various parameters were modified systematically. This allows to assess quantitatively the sensitivity of the particle-size determination to the assumed boundary conditions, such as bathgas temperature, pressure, heat-up temperature, aggregate size, and thermal accommodation coefficients. By systematically changing a single boundary condition at a time, the LII signal trace was simulated via LIISim, convoluted with the characteristics of the detection gates and an apparent particle size was determined from the resulting simulated signal ratio from the look-up table. The evaluated differences between the resulting apparent sizes and the initial particle size provided information about the sensitivity of the method to the respective variable.

It was observed that at elevated pressures there is a substantial difference between the decay rate of isolated soot and aggregated soot. However once the aggregation is considered, the impact of the aggregate size is marginal. The bathgas temperature has a multifaceted effect on particle sizing through conductive cooling and the level of the resulting heat-up temperature. It was identified that the particle-size evaluation has the lowest sensitivity to the uncertainties of heat-up temperatures between 3400–3900 K. The sensitivity analysis for bathgas temperature and heat-up temperature were performed for 1–60 bar and it is observed that for elevated pressures the sensitivity of the LII evaluation to the boundary conditions is strongly reduced. This is attributed to the fact that at higher pressures the normalized LII signal traces of different particle sizes fall into a narrower envelope and curves with different conditions become more similar.

The dependence of the heat-up temperature on the particle size at high pressure is well known. The discrepancy between particles with 10 and 40 nm diameter at 60 bar was calculated as high as 400 K for a moderate laser fluence. To reduce the uncertainties in particle sizing arising from this effect, the heat-up phase should be included in the simulation rather than imposing a single peak temperature value (such as derived from two-color LII).

In soot clouds with significant optical density, laser attenuation may cause additional non-uniformity in the spatial distribution of the heat-up temperatures. In a measurement with moderate laser fluence, attenuation up to 20% causes an error on the particle size less than 3%. For stronger attenuation, however, the error increases. Spatial variation in laser fluence can be measured by soot pyrometry imaging and effective laser fluences can be evaluated from heat-up temperatures.

To find an optimum gating strategy, time-resolved model signals were convoluted with varying gate widths or at varying delays. In the first attempt both gates are confined to the cooling part of the LII signal, and to maximize the signal intensity, the first gate is fixed to the time of maximum signal. It is

analytically shown that for mono-disperse soot ensembles there is an optimum delay for the second detection gate. This optimum delay depends on the signal lifetime and therefore depends on pressure. In the second attempt the sensitivity of particle sizing is boosted up to 8% by advancing the first gate to the starting point of the laser-heating and by positioning the second gate to the respective optimum delay. This strategy also provides a significant enhancement to signal-to-noise ratio, yet it is possible only if heat-up modeling is included in the simulations. In the third attempt an extension of the second gate width is added. It is found that a second gate width as two times long as the first one yields an additional 50% increase in the sensitivity along with an additional increase in the signal-to-noise ratio. In a measurement where the signal lifetime and gate widths are short, timing jitter can influence the evaluated results strongly. The effects of timing jitter for particle sizing and heat-up temperature measurements were shown.

Particle-size imaging based on time-gated signal ratios is inherently a mono-disperse evaluation technique since the necessary information for a more detailed analysis is lost during the convolution and gate delay. The mono-disperse equivalent mean particle size is always biased towards larger sizes. The reason of this bias is due to the dominance of the large particles' contribution to the collected signal due to their longer and stronger incandescence. At high-pressure applications the particle-size dependent peak temperature may cause additional bias towards the larger sizes. These biases are evaluated for different pressures and distributions.

Similar optimum gating strategies were assessed for two-color pyrometry imaging. It is shown that measured heat-up temperatures with such method are biased to lower temperature. At 60 bar, a bias of 200 K was calculated for a particle with 30 nm diameter.

6.2 Measurements at Diesel engine conditions

LII particle-size imaging is conducted for the Diesel engine-relevant conditions and the applicability of the method is assessed in comparison to results of sampling measurements. At the time of measurements, the optimum gating strategy showed in section 6.1.4 was not fully developed and therefore concepts of gate-advancing and asymmetric-gating were unknown and were not employed in these experiments. To relate this research to other similar works in the literature, the experiments are again conducted for the standard ECN conditions.

6.2.1 Experiment setup

The LII measurements were performed in the same high-pressure high-temperature vessel introduced in section 5.1 several months after the soot volume fraction measurements. In the interim Malbec et

al. [123] provided a fine characterization of the vessel and the injector used in this particle-size imaging study. To achieve the ECN targets, the identical vessel settings shown in ref. [123] are used. A good match with ECN's database was confirmed from the lift-off length measurements via OH* chemiluminescence for Spray A [20,48,123].

Best conditions for LII measurements are present in cases with locally high soot volume fractions (f_v) in a restricted area in the measurement plane but an overall low soot mass (m_s) to minimize laser attenuation and signal trapping. Among the target conditions for Diesel sprays defined by the ECN (cf. Tab. 6), a variant of ECN's Spray A, where the fuel is injected into a gas mixture with 21% O_2, provided the best combination of high f_v in the center and limited soot mass m_s (cf. Fig. 47 and Fig. 49a). This is labeled as "reference condition" in this study. To investigate the effects of varying boundary conditions on the measured particle size, additional experiments were carried out where injection pressure, temperature, and O_2 concentration deviated from the reference spray case (Tab. 10). To make sure that sufficient soot are deposited on TEM grids during the sampling, in all experiments the fuel injection duration is fixed to 6 ms.

Tab. 10: Experimental conditions. Case 1 is the reference used in this paper, case 4 is ECN's Spray A.

Case	O_2 / %	T / K	Fuel injection *p* / bar	Fuel injection *t* / ms
1 (Reference)	21	900	1500	6
2	21	1000	1500	6
3	21	900	1000	6
4 (Spray A)	15	900	1500	6

Fig. 68 illustrates the arrangement of the experiment. The fuel is again injected horizontally into the vessel with the Bosch injector (no: 201.01) [123]. For particle heating, the fundamental of a Nd:YAG laser at 1064 nm is used with a pulse width of 7 ns. A set of cylindrical lenses forms a horizontal laser sheet, and a 1 mm slit aperture crops the laser sheet into a rectangular shape that is relay-imaged into the probe volume with a pair of spherical lenses creating a nearly top-hat intensity profile. The laser sheet intersects the spray axis between 28 and 62 mm downstream of the nozzle. The laser is fired 3.5 ms after the start of injection.

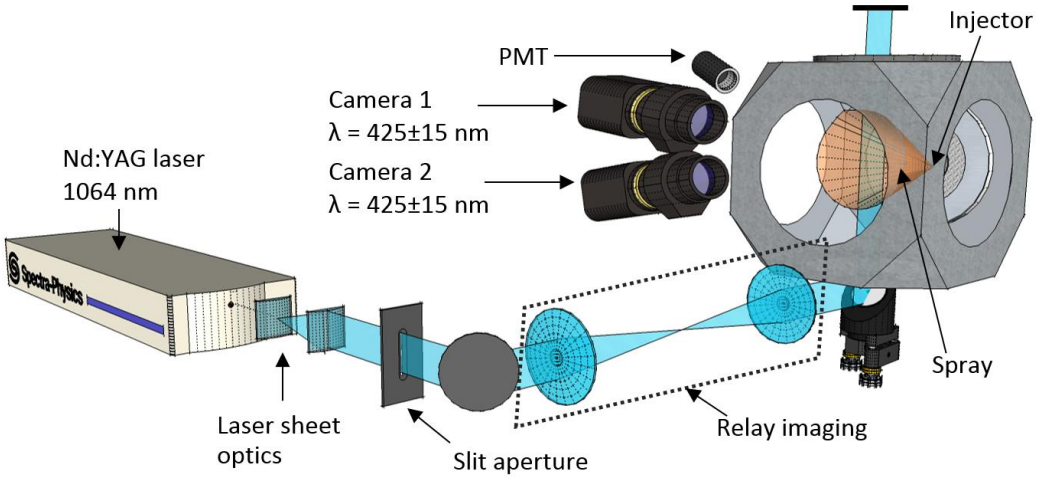

Fig. 68: Experimental arrangement.

For particle-size imaging the LII signal is selected via a bandpass filter (425±15 nm) and imaged at 90° by f = 50 mm, f/1.4 lenses onto the chips of an intensified CCD (camera 1, PI-MAX 2, 512×512 pixels after 2×2 binning) and an intensified EMCCD (camera 2, PI-MAX 4, 512×512 pixels). To measure the jitter between the laser pulse and signal detection that affects the data interpretation, the LII signal is additionally detected with a fast photomultiplier (Hamamatsu R7400U-04, rise time ~0.78 ns) and stored together with the camera gate signals on a 1 GHz oscilloscope.

To optimize image mapping for both cameras, three strategies were compared:

(1) Positioning the cameras at opposite sides of the vessel was discarded because signal trapping of the randomly-oriented soot cloud significantly affected both images individually and thus influence the signal ratio.

(2) Observing the probe volume with both cameras from one side via a 50% beam splitter provided a perfect geometric overlap that minimizes the influence of signal trapping on the intensity ratio but the 50% signal loss resulted in an unwanted deterioration of the signal-to-noise ratio.

(3) As the best compromise, both cameras were positioned next to each other detecting signal through the same window but at slightly different angles to the spray axis (Fig. 68). For mapping of the slightly distorted images a strategy developed by Tea et al. [139] was used.

Based on the numerical analysis described in section 6.1.4, a combination of detection gates was chosen, one starting at the signal peak and the other with a 5 ns delay (as mentioned above, additional benefits from gate-advancing and asymmetric-gating could not be utilized). For condition 1, 3, and 4 (cf. Tab. 10), the gate width of both cameras was set to 15 ns, whereas a 10 ns gate was sufficient for condition 2 with a larger f_v.

For two-color pyrometry, spectral bands were selected according to the recommendation of [65] and the bandpass filter of camera 1 was replaced with a 676±15 nm filter while the filter of camera 2 was kept. The relative sensitivity of both detectors was calibrated against the well-documented temperature of a non-premixed ethylene/air Santoro flame (cf. section 3.3.2) operated under standard conditions. Because this calibration is based on soot emission, the emissivity ratio in eq. 2 in section 3.1 is identical in calibration and the actual measurements (assuming that emissivity does not change with soot temperature and morphology). Pyrometry imaging was used to determine LII heat-up temperatures where both cameras were activated at the LII signal peak with 15 ns gate times.

Ex-situ soot analysis

Soot was sampled from various locations of the soot cloud by thermophoretic deposition on a carbon-coated copper grid that stays in a steel grid-holder probe that is attached to the side wall opposite to the injector at variable distance from the injector. Grids were purchased from Tedpella (Product No: 01813) [111]. The grid-holder probe and a direct imaging of sampling at three different axial distances are shown in Fig. 69 (injector is attached to left side wall).

The probe is placed slightly above the main jet flow axis (upper half of the jet impinges onto the probe but the lower half of the spray is undisturbed) to minimize flow disturbance. The particle-laden flow enters the probe through a 1-mm diameter hole and soot particles are deposited on the grid. The restricted flow passage ensures flame quenching and also protects the grid against excessive heating [79]. The sampling location was chosen as the position of maximum soot emission along the spray axis as determined for each condition from soot luminosity images. For the four cases of Tab. 10, these locations are 45, 42, 41, and 60 mm downstream of the injector orifice. For case 1, additional samples were extracted at 36 and 60 mm to probe zones of soot formation and burn-out. To prevent cross-contamination, the probe and the high precision tweezers were cleaned with ethanol in an ultrasonic bath in between experiments.

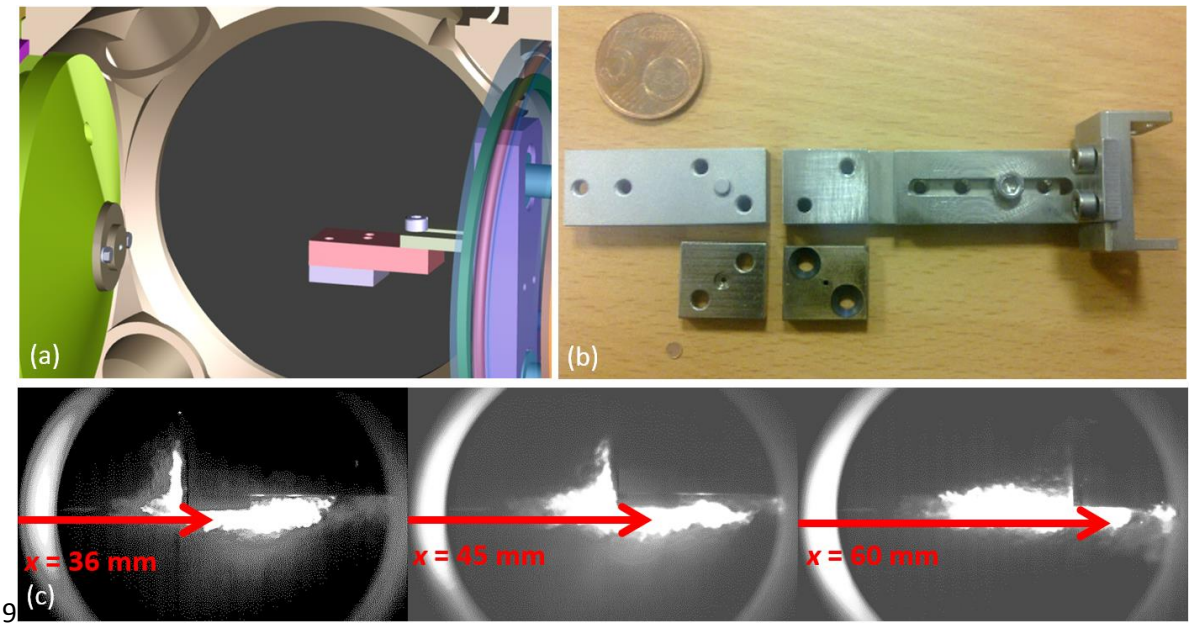

9

Fig. 69: (a) The steel grid-holder probe for soot sampling device attached to the side wall of the vessel opposite to the injector. (b) With a telescopic design, the grid can be positioned at variable distance from the injector. (c) Direct imaging of sampling at three different axial distances. Upper half of the jet impinges onto the probe but the lower half of the spray is undisturbed.

The samples were investigated by high-resolution transmission electron microscopy (HR-TEM: JEM-2100F, operating voltage: 200 keV, point resolution: 0.19 nm) equipped with a CCD camera, Gatan Ultrascan 1000/First Light (resolution: 2048×2048 pixels, physical pixel resolution: 14 µm) at the School of Science and Technology, Meiji University, Japan. The TEM grids were investigated without any thermal or chemical pre-treatment to maintain the properties of the soot particles sampled in Diesel flames as much as possible. Details of sample treatment and analysis are described in [79]. More than five TEM images were taken at five different locations on each TEM grid with clear distance with a magnification of ×20,000. The time between the sampling and the TEM investigation was slightly longer than one month. Aizawa et al. [79] reported that the delay has no impact on the measurements.

6.2.2 Results

6.2.2.1 Pyrometry imaging

The particle heat-up temperature depends on the local laser fluence, the optical properties of soot, the surrounding gas temperature, and heat transfer with the environment. It is on the other side the determining quantity in LII measurements that can be influenced through choosing laser fluences that provide strong signals while avoiding particle evaporation.

Across the measurement plane the local laser fluence can vary due to inhomogeneous laser profiles and laser attenuation. Additionally, the absorption properties of soot can change during aging of soot. The gas temperature is mostly related to the mixture fraction and thus typically varies within the measurement domain. The combined effects can lead to a non-uniform distribution in particle heat-up temperatures which was investigated by two-color pyrometry imaging. The temperature was derived for each pixel from the ratio of signal intensities within two spectral detection bands. As discussed in section 2, heat transfer during the laser pulse causes an inhomogeneous temperature distribution within the poly-disperse particle ensemble with pyrometry preferentially measuring the high-temperature end of the distribution. Furthermore, the lifetime of the LII signal is only marginally longer than the gate duration required for the collection of sufficiently strong signal. Therefore, an instantaneous measurement of the peak particle temperature cannot be achieved and the actual results are biased towards lower temperatures because significant cooling of the particles during the measurement interval. The model-based analysis in section 6.1.7 leads to an estimated bias for the near Spray A conditions of ~200 K. Therefore, temperatures obtained from pyrometry were increased by 200 K before using them for the evaluation of LII signals.

The best-suited laser fluence for the experiments was chosen based on the measured heat-up temperatures as a function of laser fluences (varied by changing the Q-switch delay of the Nd:YAG laser). At each laser fluence, 15 experiments were conducted and an ensemble average was calculated. Each data point in Fig. 70 represents a mean value determined in a 2×2-pixel square at the maximum value found in the ensemble-averaged images (increased by 200 K according to the discussion above). The error bars represent the spatially-averaged pixelwise-recorded standard deviation in temperature, based on shot-to-shot variations. To suppress the influence of background signal, i.e., line-of-sight integrated flame luminosity, 20 experiments without laser heating were taken under identical conditions and the ensemble-averaged signals were subtracted from the respective channels. The pixel-to-pixel variation in the measurement domain of the ensemble-averaged image was 6% of the mean showing that the temperature distribution was fairly homogeneous. The maximum laser fluence in the experiment was 0.2 J/cm^2 which is not sufficient at 60 bar to reach the maximum particle temperature limited by sublimation. For all particle sizing measurements, the laser fluence was set to ~0.15 J/cm^2 because this yielded sufficient signal with limited evaporation. Note that similar laser fluences cause noticeably higher peak temperatures at atmospheric pressure.

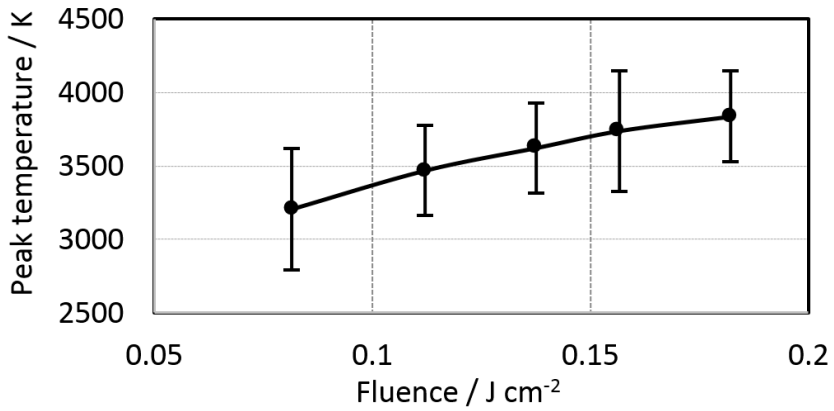

Fig. 70: Effect of the laser fluence on the peak temperature. Vertical bars represent the standard deviation of the ensemble average, based on variations between individual experiments.

To determine the bathgas temperature within the laser sheet in the center of the jet, mixture-dependent adiabatic flame temperatures are calculated using a simple fuel/air-entrainment model [47] and additionally the CFD results of a similar spray [140] are used. These models yield a temporally-averaged temperature distribution, and therefore do not reflect instantaneous variations. Both approaches showed that the gas temperature along the jet axis increases with increasing distance from the orifice.

6.2.2.2 Particle-size imaging

To correctly evaluate the measured LII signal ratios, information about local conditions (temperature, gas composition, pressure, optical properties of soot, morphology) are necessary for modeling the heating and cooling processes. Because these spatially and temporally varying conditions are not known, a phenomenological approach is used assuming homogeneous conditions for any measurement instant (cf. Tab. 11) where conditions are only modified in case reliable information about the expected variation exists. The pressure was measured for each experiment and the standard deviation from 950 experiments was less than 0.6% of the target value. Therefore, for all measurements in case 1, 3, and 4 (Tab. 1), an ambient pressure of 61 bar was used, whereas in case 2, this value was 68 bar. For temperatures, based on the simulations mentioned above, the measurement domain (x = 28–62 mm) was divided into nine equal segments with 50 K increments from 1600 to 2000 K while assuming invariant temperatures along the radial direction (cf. Fig. 71). For each segment a unique LII model-library was created.

Tab. 11: Boundary conditions for particle sizing in the reference case.

LII model input	
Ambient pressure	61 bar
Detection range	410–440 nm
Gas temperature	1600–2000 K
Laser fluence	0.15 J/cm^2
Laser pulse duration	7 ns
$E(m)$	0.4
Aggregate size	50
Thermal accommodation coefficient	0.25

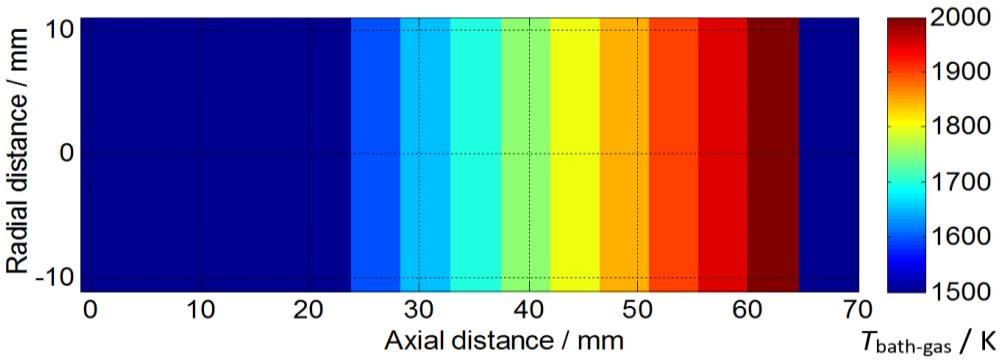

Fig. 71: Bathgas temperature used as input parameters for libraries. The measurement domain is divided into nine equal segments with 50 K increments from 1600 to 2000 K while assuming invariant temperatures along the radial direction.

Because the measurements of the heat-up temperatures did not show significant spatial variations, absorption-related parameters, i.e., laser fluence, laser-pulse duration and absorption properties ($E(m)$ = 0.4 [8]) were kept uniform for all the pixels in all the simulations. For the thermal accommodation coefficient, α_T, a constant value of 0.25 was used for all the simulations [15,133]. Based on a statistical analysis of previous TEM measurements of soot morphology for comparable conditions [79], an aggregate size of 50 is chosen for all simulations assuming the properties of graphite-like material [98]. For heat conduction, Fuchs' approach was chosen in LIISim and calculations were done for mono-disperse soot. The measured actual gate times relative to the laser pulse were used to create virtual gated signals in the modeling. The gate profiles were assumed to be rectangular.

Fig. 72 shows evaluated particle sizes for four conditions (cf. Tab. 10) as ensemble averages of 20 measurements. Areas with pixel values below 5% of the maximum intensity in each image were discarded when determining the ratio. Strong cyclic variations were observed in the particle-size images

at all conditions. In Fig. 73, the ratio of the standard deviation calculated from 20 experiments to the ensemble mean is shown for the reference condition. The spatially-averaged value of the relative standard deviation is 40%. These variations can be related to the turbulent nature of the Diesel combustion process. Furthermore, the actual deviations in the assumed boundary conditions for size evaluation can cause different results in each individual experiment.

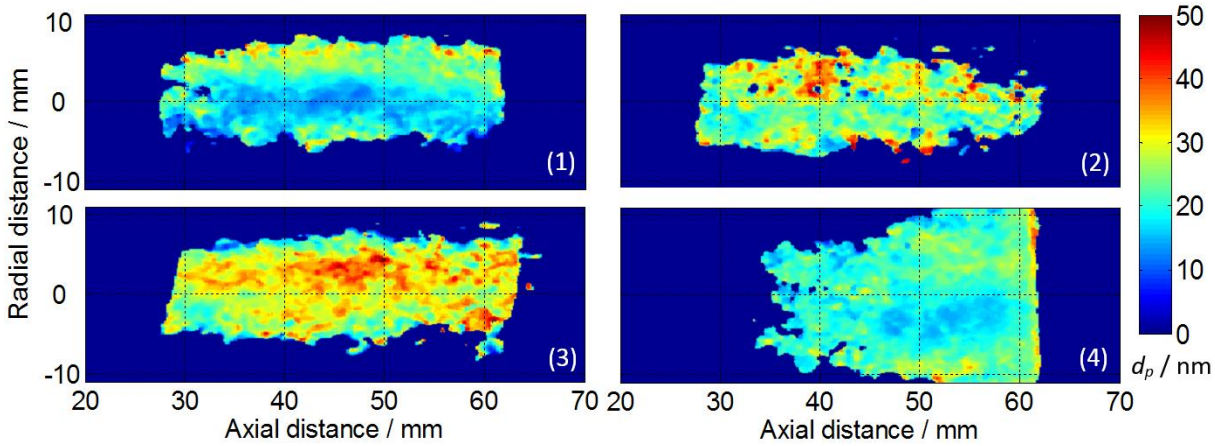

Fig. 72: Spatially-resolved particle-size distributions from LII for case 1-4 in Tab. 10.

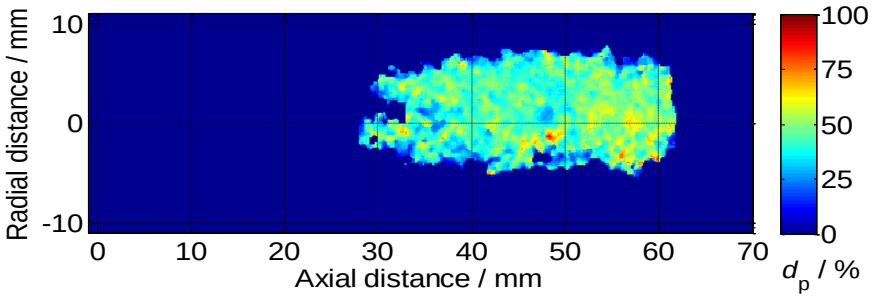

Fig. 73: Cyclic variations: Ratio of the standard deviation calculated during the ensemble averaging of 20 sprays to the ensemble-averaged image at reference spray conditions in percentage.

6.2.2.3 Electron microscopy results

Fig. 74 shows the normalized size distributions from a TEM analysis of soot sampled in the reference spray at three different axial locations. In the zone with increasing f_V (x = 36 and 45 mm), the size of 650 particles was evaluated. In the oxidation zone (x = 60 mm) only 272 particles could be measured due to the sparse soot deposition on the grid. Fitting a log-normal distribution to each of the curves revealed count median diameters (d_{cmd}) of 14.7, 9.9, and 7.3 nm at x = 36, 45, and 60 mm, respectively. In contrast, LII obtained arithmetic mean values of 13.7, 13.3, and 19.6 nm for the same areas, respectively, as determined from a 1-mm^2 field on the centerline of the ensemble-averaged images. These results derived by LII are shown as vertical bars in Fig. 74. Fig. 75 shows the TEM-derived nor-

malized size distributions for soot sampled at each experimental conditions given in Tab. 1. The measured count median diameters are 9.9, 13.1, 9.1, and 9.1 nm for case 1 to 4, respectively. The particle sizes derived from LII imaging are shown as vertical lines in Fig. 75 with arithmetic mean values of 13.3, 24.2, 32.1, and 20.2 nm, respectively.

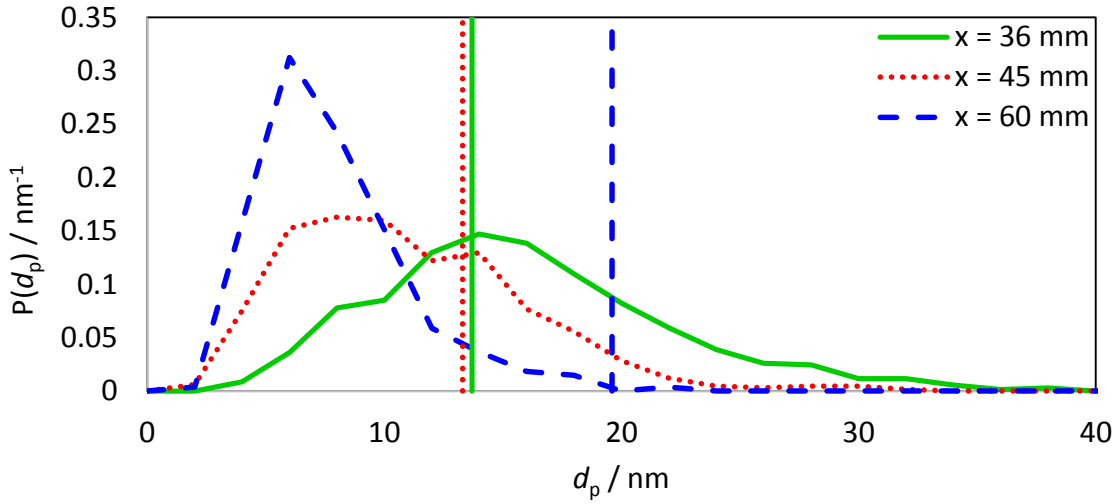

Fig. 74: Particle-size histograms from TEM analysis of soot sampled at three locations along the spray axis for case 1 (Tab. 10). The size distributions are normalized and the integral of distribution curve is equal to unity. Vertical lines represent the spatially-averaged particle-sizes from LII for the respective axial positions.

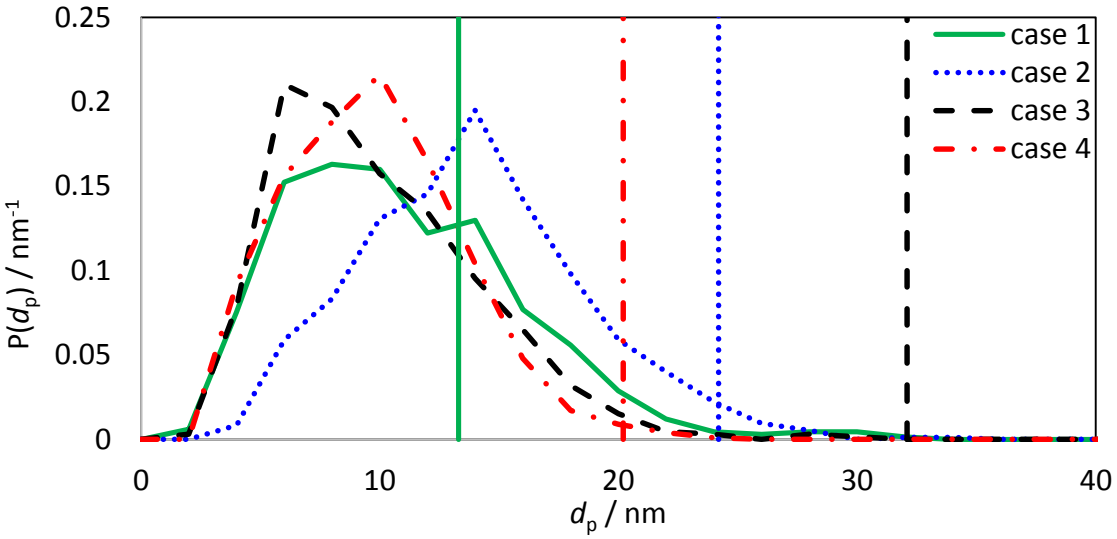

Fig. 75: Particle-size histograms from TEM analysis of soot sampled at the position of maximum soot emission along the spray axis for case 1-4 in Tab. 10. The size distributions are normalized and the integral of distribution curve is equal to unity. Vertical lines represent the spatially-averaged particle-sizes from LII for the respective location and conditions.

6.2.3 Discussion

Particle sizes determined from LII and TEM show substantial differences. Both measurements contain several sources of uncertainty. One major problem of LII particle sizing is related to the fact that small particles are underrepresented in the measured signal intensity at the high pressures relevant for Diesel combustion. TEM measurements from the present study and comparable situations [12,110] show that the mean primary particle size is ~15 nm. With such small particles the LII-signal lifetime is too short for capturing signal contributions from those particles by the delayed-gate technique applied here. Furthermore, the poly-disperse nature of the soot and the strong dependence of the LII signal on particle size cause a strong bias towards the larger particles in the ensemble (cf., section 6.1.6). Due to the size-dependent cooling of particles, larger particles are hotter than the smaller particles at any instant within the LII signal lifetime.

To demonstrate this, the analysis performed in section 4.6.3 is repeated here with the Diesel jet measurement results: A phantom LII signal of a poly-disperse soot cloud is simulated using the actual particle-size distribution derived by the TEM analysis of the reference spray at x = 45 mm, and the particle size is evaluated by forming a signal ratio on this simulated LII trace. The gated LII-signal ratio method yields a mono-disperse equivalent mean size of 21.5 nm, whereas the d_{cmd} of the size distribution evaluated from the TEM measurements was 9.9 nm. This result shows that the LII bias towards larger particles more than doubles the measured particle-size compared to the mean size in the distribution determined from TEM for the present conditions (as shown in Fig. 66, the bias towards larger particle sizes at high pressure is greater than the atmospheric conditions). In the ensemble-averaged particle-size distribution images (cf., Fig. 72), a systematic variation of the particle size along the jet axis related to soot formation and oxidation could not be seen. This result is in contrast to previous f_v measurements in the same spray (cf., section 5.6.4) and to the TEM results. The reason of such uniformity across the imaged spatial spray domain can be again attributed to the bias towards larger particles in the LII method. At each local zone only the largest particles contribute to the measurement and information from the smaller particles is lost. The slight variation in particle size in radial direction is believed to be caused mainly by errors due to imperfect image mapping.

Additional uncertainty in LII particle sizing is caused by the assumptions made for the local bathgas conditions because detailed knowledge of the instantaneous and local conditions is not available. For soot morphology related properties, i.e., $E(m)$, α_{T}, and aggregate size, the input parameters can spatially vary. Small variations in all these parameters may have substantial effects on the evaluated particle-sizes. When changing the assumed bathgas temperature from 1600 to 2000 K at a given location in the reference case, the evaluated mean particle-size is reduced by 25%. Additional uncertainties

should be considered in imaging applications due to shot noise, deviation of the gate profiles from the assumed top-hat shape, and imperfect image mapping.

One important aspect in the present study is the correction for timing jitter. To quantify the error when neglecting jitter, the size evaluation is performed with a first gate fixed to the peak signal and a second gate with a fixed 5 ns delay in the model library. This changed the evaluated spatially-averaged particle size by more than 20%, whereas the deviation at some local pixels was up to 50%. The ensemble-averaged distribution of the particle-size variation due to the timing jitter is shown in Fig. 76. The jitter correction is effective only if heat-up modeling is included in the signal library.

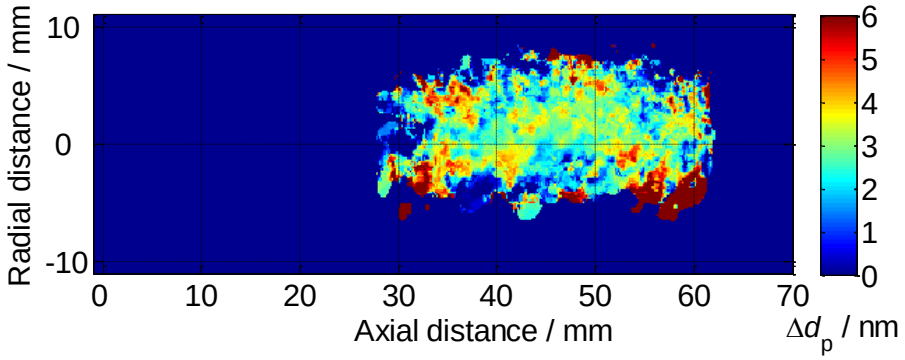

Fig. 76: Variation of particle sizes evaluated without consideration of the actual timing jitter in the system.

It must, however, be considered that uncertainties also exist in TEM measurements where the probe can interfere with the dynamics and the combustion of the Diesel jet and the deposited soot on the grids can further oxidize leading to smaller-than-expected sizes. Additional operator-biased errors can occur in the analysis of the micrographs [101]. In this study the amount of soot deposited on the TEM grid was very limited leading to a small number of analyzed particles. A quantitative analysis of these uncertainties was not possible in these measurements. However, the evaluation of the bias towards larger particles for LII shows that in engine conditions, due to the small size of the particles and the high pressure, the application of LII is very uncertain, and – besides all limitations – TEM analysis of soot samples should be preferred. However, because TEM sampling does not provide spatial information and can strongly interact with the Diesel jet, the LII imaging technique was specifically chosen because of its imaging capabilities (rather than TiRe-LII that would provide a more detailed analysis of fast processes), it is difficult to directly compare pros and cons.

6.2.4 Conclusions

Two-dimensional particle-size imaging with laser-induced incandescence was attempted in a high-pressure Diesel combustion vessel. The main purpose of the study was to investigate the accuracy of

the method experimentally for the high-pressure conditions, and to optimize its performance. An additional purpose was to investigate effects of varying spray conditions on the evaluated soot particle-size and its spatial distribution. The experiments were conducted under the well-defined conditions of ECN's Spray A and its parametric variants to benefit from accumulated previous information and to further contribute to the database. The method in this work was based on simulations of the signal ratio from two gated portions of the LII signal trace acquired at different timings and using LII modeling to deduce the local particle size from the measured signal ratio. As an important input for modeling the LII signal trace, soot heat-up temperatures were determined via two-color pyrometry imaging. To correct for timing jitter in the experimental gate timing, a fast photodiode and oscilloscope recorded the LII signal event and camera gates simultaneously with the imaging system and necessary time corrections were made in the modeling. For *ex situ* characterization, soot particles were sampled at multiple axial locations. Particle-size distributions were derived from TEM measurements and compared to the LII results. Substantial discrepancies were observed between results from both methods.

The strong non-linear dependence of the LII intensity on particle size and temperature causes a strong bias towards information from larger particles in the acquired signal. In this study, it can be seen that this bias is more severe for high-pressure conditions because the small particles quickly loose energy already during the laser heat-up leading to lower peak temperatures and also cool down quickly afterwards. The combined effect makes them almost invisible during the LII decay. An additional source of uncertainty arises from that fact that spatially- and temporally-resolved information about bathgas conditions and materials properties is not available. Due to the combined effects, a quantitative particle-size analysis with LII imaging could not be accomplished at the >60 bar conditions of the present experiments.

7 Outlook

This work was intended to contribute to the soot and spray diagnostics communities. It focused on theoretical and experimental work on particle-size dispersion, soot volume fraction and particle-size imaging in a flame at atmospheric pressure, and in Diesel spray combustion at engine-relevant conditions. Some open questions in each of these topics could be answered, and the original conclusions were presented in this thesis. Nevertheless, in each field, open questions still exist.

LII model and particle-size dispersion

The LII model used in this thesis, LIISim, allows the simulation of signal traces also for high-pressure conditions. Nevertheless, in this work it was realized that the aggregate sub-model embedded in LIISim performs an incorrect treatment of shielding effects in soot aggregates, and further investigation is necessary. Even though LIISim includes an evaporation sub-model, it should be noted that the current understanding of evaporation is not accurate, especially at elevated pressures. This routine should be further improved.

For the analysis of particle-size dispersion, a simplified signal-processing method, two-exponential reverse fitting (TERF), is proposed in this thesis. The analysis performed on the simulated phantom signals showed that information about the size distribution can be evaluated accurately. Nevertheless, the accuracy of the method could not be tested with the experimental data acquired from the non-premixed flame successfully because the TEM measurements of the sampled soot were found unreliable. To verify the validity of TERF, LII experiments should be performed with particles with known size distributions.

Soot volume fraction

The soot volume fraction was assumed to be linearly proportional to the time-gated LII signal acquired with the camera. Such assumption can be valid only if the heat-up temperature, the primary particle-size, and the aggregate-size distributions are homogenous. At high laser fluences, the uniform heat-up temperature distribution condition can be fulfilled. However, TEM analysis indicated that the particle and the aggregate size can change from one location to another. For higher accuracy in soot volume fraction measurements, the linear proportionality assumption between the soot volume fraction and the time-gated LII signal intensity should be replaced with a relation in which particle and aggregate size changes are also accounted for.

Likewise, the non-dimensional optical absorption coefficient k_e was assumed to be uniform across the Diesel jet in this work. This value depends on the morphology of the soot and a spatial variation of this value should be expected as well. A further analysis of the spatial variation of k_e is necessary.

Particle-size imaging with LII

The sensitivity of the evaluated particle size to the model input parameters imposed in LIISim was shown for different ambient pressures. For accurate spatially-resolved particle-size information, it is imperative to perform the evaluation at each local point with the actual respective conditions. In the analysis of Diesel jet combustion, the bathgas temperature was determined with computational models which yield a temporally-averaged temperature distribution. To take the spatially-resolved instantaneous temperature variations into account, an advanced temperature characterization at the LII plane should be performed concurrently. Nevertheless, such temperature characterization in a sooting set is a non-trivial task. Two-dimensional Coherent anti-Stokes Raman spectroscopy (2D-CARS) [141] can be a suitable method for this kind of temperature measurements.

The convolution of the time-resolved model signals with the virtual detector gates is an essential step in particle-size imaging. In this work, the actual time profiles of the camera were unknown and they were assumed to be in a top hat (rectangular) shape. Likewise, the temporal profile of the laser was also not known and a Gaussian profile was assumed. In the next attempt, the time profiles of the cameras and the laser used should be measured, and these profiles should be used in convolution and simulation of the library signals.

The sampling of the soot in the high-pressure high-temperature vessel was a non-trivial task. A best effort was given during the design stage of the grid holder probe for a least amount of perturbation of the jet combustion. The design has also considered the quenching of reactions after the deposition of the soot on the grids. However, the steel probe was attached to the vessel body which was constantly at 473 K. After each spray event, a minimum of 5 to 10 minutes was necessary to disassemble the probe and to take out the grid. One can expect a further mass loss of soot within this time period at elevated temperature. The sampling operation can be enhanced with a probe design that includes a cooling system.

8 Summary

Soot formation is a result of incomplete combustion of carbon-based fuels. Soot particles have serious adverse effects on human health and the climate. To control particulate matter emissions, limits on vehicle exhaust emissions have been imposed. Meeting these regulations requires an insight into soot formation and oxidation. Measuring soot volume fractions, primary particle sizes, and their spatial distribution with *in situ* techniques during Diesel combustion is of high interest for understanding the underlying mechanisms and for developing combustion strategies that reduce pollutant formation. A combination of laser-induced incandescence (LII), line-of-sight laser extinction, multi-color pyrometry, and transmission electron microscopy measurements of thermophoretically sampled soot (TEM) is used for soot diagnostics in this study.

The principal aim of this work is to optimize two-dimensional particle sizing via LII imaging for Diesel engine conditions and to assess its applicability. Two major preliminary studies were performed: The first study was a point-wise particle-size distribution analysis in a non-premixed flame at atmospheric pressure, and the second study was two-dimensional soot volume fraction measurements in a Diesel jet and the analysis of the effects of boundary conditions on the soot volume fraction. Both studies formed the basis for the strategy of particle-size imaging for Diesel engine conditions.

Particle-size dispersion

Flame soot is usually poly-disperse and its characterization with a single average particle size is often insufficient. Information about the size distribution is important for a better understanding of soot formation and oxidation. In this study a signal-processing method, called two-exponential reverse fitting (TERF), was developed for time-resolved LII signals (TiRe-LII) in poly-disperse soot that provides information about the size range and the relative weight of the small and the large fraction of the particle ensemble. The method separates the signal contribution of small and large particles from the overall signal by approximating the LII signal from size classes with narrow size distributions with mono-exponential decays. A mono-disperse equivalent mean particle size is then evaluated for both size classes, and the relative ratio of the number densities of both groups is determined. The method does not require an assumption of the shape of the distribution and its fast evaluation makes TERF suitable for real-time analysis.

The accuracy of the method is verified by analyzing phantom LII signals that are simulated using assumed particle-size distributions. Suitable application ranges for the TERF method were determined.

The TERF method was then applied to analyze TiRe-LII signal traces that were acquired at multiple locations in a non-premixed atmospheric laminar ethylene/air Santoro burner flame. The LII measurements were supported by two-color pyrometry of particle heat-up temperatures. In addition to average small and large particle sizes, at each location a mono-disperse equivalent mean particle size was determined.

In the same flame, particle-size distributions were derived from TEM measurements of thermophoretically sampled soot and compared to the LII-derived results. It was observed that the TERF method provides sizes for the large particle class that are in good agreement with the TEM measurements. Substantial discrepancies were observed, however, between LII and TEM results for the small mode. The discrepancies were mainly associated to the biased sampling and TEM operations that omits the analysis of small size classes. The effect of varying exposure times of the TEM grid to the flame was analyzed.

Soot volume fraction

Line-of-sight laser extinction coupled LII imaging was performed to derive the soot volume fraction in a high-temperature high-pressure constant-volume pre-combustion vessel under the Engine Combustion Network's (ECN) "Spray A" conditions with parametric variations of gas temperature and composition.

At the initial step, ambient gas temperature at the spray zone at the time of injection, liquid fuel penetration, vapor fuel penetration and lift-off lengths were measured by thin thermocouples, diffuse back-illumination (DBI), schlieren imaging, and OH* chemiluminescence imaging, respectively. Results were compared to the ECN benchmark, and the validity of Spray A conditions was verified. A precise setting of operating conditions to the standard Spray A conditions in this part of this study could not be achieved. For all soot measurements, the ambient density was about 1 kg/cm^3 lower and the ambient temperatures were about 30 K higher than the target values. For future references, it is therefore recommended to take these variations into account. Nevertheless, the difficulties in setting the operating conditions to the standard Spray A conditions have been overcome after this experiment, and in the succeeding steps the operating conditions were matched precisely with the standard. It was also found that the random timing jitter between the laser and the camera was another major error source for the LII measurements. Remedies were taken to mitigate jitter-related problems after this experiment but minimizing the jitter in future experiments is important.

Soot volume fraction measurements showed that Spray A is a moderately sooting spray. Maximum soot volume fractions around 2–3 ppm are obtained at near Spray A temperature (930 K) and 12 ppm at elevated temperature (1030 K). As a result, significant signal trapping of LII radiation does not occur

and planar soot volume fraction measurements based on the LII method can be done without any signal trapping or laser-attenuation correction. Soot formation begins after autoignition during the premixed burn phase at a finite distance to the lift-off length. Soot formation initially starts close to the spray periphery, whereas the core region has no soot at early formation timings and locations. The expansion of soot formation process into core region happens only a finite time after the first soot formation. The relation between lift-off length and soot processes was also examined. The effect of ambient temperature and oxygen concentration variations were found to be consistent with previous studies. The ideal conditions of injection duration, ambient temperature and oxygen concentration for low laser fluence particle-size imaging with LII were found.

Particle-size imaging with LII

The preliminary studies of particle-size imaging with LII were conducted in the non-premixed atmospheric laminar flame from a Santoro burner with time-gate sweeping technique. The accuracy of the measurements was verified by comparing the constructed decay curve with a PMT acquired high-temporal resolution LII signal. To deduce the primary particle size from the image sequence, a look-up table method based on the ratio of two pre-calculated time-gated signals was used. The measurements provided a quantitative analysis of effects of imposed modeling inputs parameters and gate timing on the evaluated particle sizes. This study formed a basis for the measurements at Diesel engine conditions.

Particle-size imaging for Diesel engine conditions was performed in two-stages. First, the applicability of the technique for high-pressure conditions was studied based on a detailed numerical analysis. By applying the data evaluation strategy to simulated signal traces with known parameters, the sensitivity of the particle-size determination to the assumed boundary conditions was assessed quantitatively. The sensitivity analysis for bathgas temperature and heat-up temperature that were performed for 1–60 bar showed that for elevated pressures the sensitivity of the LII evaluation to the boundary conditions is strongly reduced. This is attributed to the fact that at higher pressures the normalized LII signal traces of different particle sizes fall into a narrower envelope and curves with different conditions become more similar.

The well-known dependence of the heat-up temperature on the particle size at high pressure was evaluated and possible remedies were discussed to reduce the uncertainty related to this phenomenon. In soot clouds with significant optical density, laser attenuation may cause additional non-uniformity in the spatial distribution of the heat-up temperatures. In a measurement with moderate laser fluence, attenuation up to 20% causes an error on the particle size less than 3%. For stronger attenuation, however, the error increases.

Based on an analytical and a numerical approach, various gating strategies have been assessed quantitatively for two-time step LII imaging. The optimum gating strategy has been identified as the case where the first gate starts together with particle heating, and the second gate starts at an experiment setup-dependent delay time with almost twice as long gate width than the first gate. The effects of timing jitter were investigated. Pre-calculated look-up tables are based on signal libraries that are created from simulations for the behavior of mono-disperse soot. The evaluation of the signal acquired from poly-disperse soot again yields averaged mono-disperse equivalent mean particle sizes. The mono-disperse equivalent mean particle size is always biased towards larger sizes. The magnitude of these biases were evaluated for different pressures and distributions. Systematic errors in pyrometry imaging at high pressure were evaluated.

In the second stage, following the outcomes of numerical analysis and the soot volume fraction measurements, 2D particle sizing measurements with LII were performed in near Spray A conditions in the high-temperature high-pressure vessel to investigate the accuracy of the method experimentally, and to optimize its performance. By two-color pyrometry imaging the effects of laser fluence on LII signal and the heat-up temperature was analyzed. With a concurrent acquisition of the temporally-resolved LII signal, a timing-jitter correction was implemented to the particle-size evaluation algorithm. It is calculated that in a measurement where the jitter is neglected, the error in the evaluated particle-size can be as high as 50%. For *ex situ* characterization, soot particles were sampled at multiple axial locations. Particle-size distributions were derived from TEM measurements and compared to the LII results. Substantial discrepancies were observed between results from both method, and they were discussed to analyze uncertainties and related error sources of the two diagnostics.

In the ensemble-averaged particle-size distribution images, a systematic variation of the particle size along the jet axis related to soot formation and oxidation could not be seen. This result is in contrast to previous f_v measurements in the same spray and to the TEM results. The reason of this uniformity across the imaged soot domain can be attributed to the bias towards larger particles in the LII method. At each local zone only the largest particles contribute to the measurement and information from the smaller particles is lost. TEM measurements show that the mean primary particle size is ~15 nm. With such small particles and the high pressure, the lifetime of LII signal was less than 20 ns from soot particles that were heated with moderate laser fluence under the Spray A conditions. This signal lifetime is too short for capturing signal contributions from small particles by the delayed-gate technique. Experiments were conducted with parametric variations of injection pressure, gas temperature, and composition to investigate effects of varying spray conditions on the spatial distribution of particle

size. However a systematic variation of the particle size among different spray conditions could also not be observed.

Particle-size imaging based on time-gated signal ratios is inherently a mono-disperse evaluation technique since the necessary information for a more detailed analysis is lost during the convolution and gate delay. The strong non-linear dependence of the LII intensity on particle size and temperature causes a strong bias towards information from larger particles in the acquired signal. At high-pressure applications, the particle-size dependent peak temperature may cause additional bias towards the larger sizes. An additional source of uncertainty arises from that fact that spatially- and temporally-resolved information about bathgas conditions and materials properties is not available. Due to the combined effects, a quantitative particle-size analysis with LII imaging could not be accomplished at the >60 bar conditions.

9 References

[1] M.Z. Jacobson, “Testimony for the hearing on black carbon and global warming,” House Committee on Oversight and Government Reform, United States House of Representatives, Stanford University (2007).

[2] A. Leipertz, and J. Kiefer, *Handbook of combustion: Combustion diagnostics and pollutants*, Vol. 2, (*Wiley-VCH Verlag GmbH & Co. KGaA* (Weinheim, 2010)).

[3] A. Leipertz, and R. Sommer, *Advances in chemical engineering*, Vol. 37, (*Academic Press* 2009)).

[4] A. Anda, and B. Illes, “Impact of simulated airborne soot on maize growth and development,” J. Environ. Prot. **3**, 773–781 (2012).

[5] R. Stewart, *Robin Stewart’s chemical free pest control*, (*Black Inc.* (Collingwood, 2002)).

[6] B. Hu, B. Yang, and U.O. Koylu, “Soot measurements at the axis of an ethylene/air non-premixed turbulent jet flame,” Combust. Flame **134**, 93–106 (2003).

[7] I.S. McLintock, “Soot production by diffusion flames,” Fire Reseatch Notes **570**, 1–12 (1964).

[8] D.R. Snelling, G.J. Smallwood, F. Liu, Ö.L. Gülder, and W.D. Bachalo, “A calibration-independent laser-induced incandescence technique for soot measurement by detecting absolute aight intensity,” Appl. Opt. **44**, 6773–6785 (2005).

[9] J.C. Chow, J.G. Watson, J.L. Mauderly, D.L. Costa, R.E. Wyzga, S. Vedal, G.M. Hidy, S.L. Altshuler, D. Marrack, J.M. Heuss, G.T. Wolff, C. Arden Pope III, and D.W. Dockery, “Health effects of fine particulate air pollution: Lines that connect,” J. Air Waste Manage. Assoc. **56**, 1368–1380 (2006).

[10] World Health Organization, “IARC : Outdoor air pollution a leading environmental cause of cancer deaths,” Press Release N° 221 (2013).

[11] International council on clean transportation, *Pocketbook: European vehicle market statistics*, ((Berlin, 2013)).

[12] S. Kook, R. Zhang, K. Szeto, L.M. Pickett, and T. Aizawa, “In-Flame soot sampling and particle analysis in a Diesel engine,” SAE Int. J. Fuels Lubr. **6**, 80–97 (2013).

[13] L.A. Melton, “Soot diagnostics based on laser heating,” Appl. Opt. **23**, 2201–2208 (1984).

[14] C. Schulz, B.F. Kock, M. Hofmann, H.A. Michelsen, S. Will, B. Bougie, R. Suntz, and G.J. Smallwood, “Laser-induced incandescence: recent trends and current questions,” Appl. Phys. B **83**, 333–354 (2006).

[15] H.A. Michelsen, F. Liu, B.F. Kock, H. Bladh, A. Boiarciuc, M. Charwath, T. Dreier, R. Hadef, M. Hofmann, J. Reimann, S. Will, P.-E. Bengtsson, H. Bockhorn, F. Foucher, K.-P. Geigle, C. Mounaïm-Rousselle, C. Schulz, R. Stirn, B. Tribalet, and R. Suntz, “Modeling laser-induced incandescence of soot: a summary and comparison of LII models,” Appl. Phys. B **87**, 503–521 (2007).

[16] S. Will, S. Schraml, and A. Leipertz, “Two-dimensional soot-particle sizing by time-resolved laser-induced incandescence.,” Opt. Lett. **20**, 2342–2344 (1995).

[17] S. Will, S. Schraml, and A. Leipertz, “Comprehensive two-dimensional soot diagnostics based on laser-induced incandescence,” Proc. Combust. Inst. **26**, 2277–2284 (1996).

[18] S. Will, S. Schraml, K. Bader, and A. Leipertz, “Performance characteristics of soot primary particle size measurements by time-resolved laser-induced incandescence,” Appl. Opt. **37**, 5647–5658 (1998).

[19] L.M. Pickett, C.L. Genzale, G. Bruneaux, L.M. Malbec, L. Hermant, C. Christiansen, and J. Schramm, “Comparison of Diesel spray combustion in different high-temperature , high-pressure facilities,” SAE Int. **3**, 156–181 (2010).

[20] L.M. Pickett, ECN Website, available at <http://www.sandia.gov/ecn/index.php>.

[21] L. Francqueville, G. Bruneaux, and B. Thirouard, “Soot volume fraction measurements in a gasoline direct injection engine by combined laser induced incandescence and Laser extinction method,” SAE Int. J. Fuels **3**, 163–182 (2010).

[22] M. Hofmann, B.F. Kock, and C. Schulz, “A web-based interface for modeling laser-induced incandescence (LIISim),” *in*: *European Combustion Meeting 2007 (Chania, 2007)*.

[23] G.J. Smallwood, *A Critique of Laser-Induced Incandescence for the Measurement of Soot*, PhD thesis, Cranfield University, 2008.

[24] P. Roth, and A.V. Filippov, “In situ ultrafine particle sizing by combination of pulsed laser heatup and particle thermal emission,” J. Aerosol Sci. **27**, 95–104 (1996).

[25] T. Lehre, H. Bockhorn, B. Jungfleisch, and R. Suntz, “Development of a measuring technique for simultaneous in situ detection of nanoscaled particle size distributions and gas temperatures,” Chemosphere **51**, 1055–61 (2003).

[26] H. Bladh, J. Johnsson, J. Rissler, H. Abdulhamid, N.-E. Olofsson, M. Sanati, J. Pagels, and P.-E. Bengtsson, “Influence of soot particle aggregation on time-resolved laser-induced incandescence signals,” Appl. Phys. B **104**, 331–341 (2011).

[27] F. Liu, B.J. Stagg, D.R. Snelling, and G.J. Smallwood, "Effects of primary soot particle size distribution on the temperature of soot particles heated by a nanosecond pulsed laser in an atmospheric laminar diffusion flame," Int. J. Heat Mass Transf. **49**, 777–788 (2006).

[28] K.J. Daun, B.J. Stagg, F. Liu, G.J. Smallwood, and D.R. Snelling, "Determining aerosol particle size distributions using time-resolved laser-induced incandescence," Appl. Phys. B **87**, 363–372 (2007).

[29] M. Hofmann, B.F. Kock, T. Dreier, H. Jander, and C. Schulz, "Laser-induced incandescence for soot-particle sizing at elevated pressure," Appl. Phys. B **90**, 629–639 (2007).

[30] S. Banerjee, B. Menkiel, and L.C. Ganippa, "Multi-lognormal soot particle size distribution for time-resolved laser induced incandescence in diesel engines," Appl. Phys. B **96**, 571–579 (2009).

[31] S. Dankers, and A. Leipertz, "Determination of primary particle size distributions from time-resolved laser-induced incandescence measurements," Appl. Opt. **43**, 3726–3731 (2004).

[32] H. Bockhorn, *Soot formation in combustion, mechanisms and models; Springer series in chemical physics*, (*Springer-Verlag* (Berlin, 1994)).

[33] M. Frenklach, and H. Wang, "Detailed modeling of soot particle nucleation and growth," *in*: *1990)*.

[34] I. Glassman, *Combustion*, (*Academic Press* (San Diego, 1996)).

[35] C.A. Idicheria, and L.M. Pickett, "Ignition, soot formation, and end-of-combustion transients in Diesel combustion under high-EGR conditions," Int. J. Engine Res. **12**, 376–392 (2011).

[36] L.M. Pickett, and C.A. Idicheria, "Effects of ambient temperature and density on soot formation under high-EGR conditions," *in*: *THIESEL 2006 Conference on Thermo- and Fluid Dynamic Processes in Diesel Engines Effects (Valencia, 2006)*.

[37] C.A. Idicheria, and L.M. Pickett, "Soot formation in Diesel combustion under high-EGR conditions," SAE Tech. Pap. 2005–01–3834 (2005).

[38] S. Kook, and L.M. Pickett, "Soot volume fraction and morphology of conventional , Fischer-tropsch , coal-derived , and surrogate fuel at Diesel conditions," SAE Int. J. Fuels Lubr. **5**, 647–664 (2012).

[39] L.M. Pickett, and D.L. Siebers, "Soot in Diesel fuel jets: effects of ambient temperature, ambient density, and injection pressure," Combust. Flame **138**, 114–135 (2004).

[40] M.P.B. Musculus, and L.M. Pickett, "Diagnostic considerations for optical laser-extinction measurements of soot in high-pressure transient combustion environments," Combust. Flame **141**, 371–391 (2005).

[41] L.M. Pickett, D.L. Siebers, and C.A. Idicheria, “Relationship between ignition processes and the lift-off length of Diesel fuel jets,” SAE Tech. Pap. **114**, 1714–1731 (2005).

[42] K. Akihama, Y. Takatori, K. Inagaki, A.M. Dean, and S. Sasaki, “Mechanism of the smokeless Rich Diesel combustion by reducing temperature,” SAE Tech. Pap. 2001–01–0655 (2001).

[43] W. Hentschel, and J.-U. Richter, “Time-resolved analysis of soot formation and oxidation in a direct-injection Diesel engine for different EGR-rates by an extinction method,” (1995).

[44] M. Charwath, R. Suntz, and H. Bockhorn, “Constraints of two-colour TiRe-LII at elevated pressures,” Appl. Phys. B **104**, 427–438 (2011).

[45] M. Meijer, B. Somers, J. Johnson, J. Naber, S.-Y. Lee, L.-M. Malbec, G. Bruneaux, L.M. Pickett, M. Bardi, R. Payri, and T. Bazyn, “Engine combustion network (ECN): Characterization and comparison ofboundary conditions for different combustion vessels,” Atom. Spray. **22**, 777–806 (2012).

[46] B.C. Connelly, *Quantitative characterization of steady and time-varying, sooting, laminar diffusion flames using optical techniques*, PhD thesis, Yale University, 2009.

[47] L.M. Pickett, and D.L. Siebers, “Soot formation in Diesel fuel jets near the lift-off length,” Int. J. Engine Res. **7**, 103–130 (2006).

[48] E. Cenker, G. Bruneaux, L.M. Pickett, and C. Schulz, “Study of soot formation and oxidation in the engine combustion network (ECN), Spray A: Effects of ambient temperature and oxygen concentration,” SAE Int. J. Engines **6**, 352–365 (2013).

[49] C. Brackmann, J. Bood, P.-E. Bengtsson, T. Seeger, M. Schenk, and A. Leipertz, “Simultaneous vibrational and pure rotational coherent anti-stokes Raman spectroscopy for temperature and multispecies concentration measurements demonstrated in sooting flames.,” Appl. Opt. **41**, 564–72 (2002).

[50] J. Nygren, J. Engström, J. Walewski, C.F. Kaminski, and M. Aldén, “Applications and evaluation of two-line atomic LIF thermometry in sooting combustion environments,” Meas. Sci. Technol. **12**, 1294–1303 (2001).

[51] W.G. Bessler, and C. Schulz, “Quantitative multi-line NO-LIF temperature imaging,” Appl. Phys. B Lasers Opt. **78**, 519–533 (2004).

[52] B. Williams, M. Edwards, R. Stone, J. Williams, and P. Ewart, “High precision in-cylinder gas thermometry using laser induced gratings: Quantitative measurement of evaporative cooling with gasoline/alcohol blends in a GDI optical engine,” Combust. Flame **161**, 270–279 (2014).

[53] H.C. Hottel, and F.P. Broughton, “Determination of true temperature and total radiation from luminous gas flames,” Ind. Eng. Chem. **4**, 166–174 (1932).

[54] Y.A. Levendis, K.R. Estrada, and H.C. Hottel, “Development of multicolor pyrometers of burning carbonaceous particles,” Rev. Sci. Instrum. **63**, 3608–3621 (1992).

[55] H. Zhao, and N. Ladommatos, “Optical diagnostics for soot and temperature measurement in Diesel engines,” Prog. Energy Combust. Sci. **24**, 221–255 (1998).

[56] B. Menkiel, A. Donkerbroek, R. Uitz, R. Cracknell, and L. Ganippa, “Measurement of in-cylinder soot particles and their distribution in an optical HSDI Diesel engine using time resolved laser induced incandescence,” Combust. Flame **159**, 2985–2998 (2012).

[57] S.S. Krishnan, K. Lin, and G.M. Faeth, “Optical properties in the visible of overfire soot in large buoyant turbulent diffusion flames,” J. Heat Transfer **122**, 517–524 (2000).

[58] S.S. Krishnan, K.-C. Lin, and G.M. Faeth, “Extinction and scattering properties of soot emitted from buoyant turbulent diffusion flames,” J. Heat Transfer **123**, 331–339 (2001).

[59] T.C. Williams, C.R. Shaddix, K.A. Jensen, and J.M. Suo-anttila, “Measurement of the dimensionless extinction coefficient of soot within laminar diffusion flames,” Int. J. Heat Mass Transf. **50**, 1616–1630 (2007).

[60] D.R. Snelling, F. Liu, G.J. Smallwood, and O. Gulder, “Determination of the soot absorption function and thermal accommodation coefficient using low-fluence LII in a laminar coflow ethylene diffusion flame,” Combust. Flame **136**, 180–190 (2004).

[61] G. Cléon, T. Amodeo, A. Faccinetto, and P. Desgroux, “Laser induced incandescence determination of the ratio of the soot absorption functions at 532 nm and 1064 nm in the nucleation zone of a low pressure premixed sooting flame,” Appl. Phys. B **104**, 297–305 (2011).

[62] H. Bladh, J. Johnsson, N.-E. Olofsson, A. Bohlin, and P.-E. Bengtsson, “Optical soot characterization using two-color laser-induced incandescence (2C-LII) in the soot growth region of a premixed flat flame,” Proc. Combust. Inst. **33**, 641–648 (2011).

[63] E. Therssen, Y. Bouvier, C. Schoemaecker-Moreau, X. Mercier, P. Desgroux, M. Ziskind, and C. Focsa, “Determination of the ratio of soot refractive index function E(m) at the two wavelengths 532 and 1064 nm by laser induced incandescence,” Appl. Phys. B **89**, 417–427 (2007).

[64] P.B. Kuhn, B. Ma, B.C. Connelly, M.D. Smooke, and M.B. Long, “Soot and thin-filament pyrometry using a color digital camera,” Proc. Combust. Inst. **33**, 743–750 (2011).

[65] F. Liu, D.R. Snelling, K.A. Thomson, and G.J. Smallwood, “Sensitivity and relative error analyses of soot temperature and volume fraction determined by two-color LII,” Appl. Phys. B **96**, 623–636 (2009).

[66] S. Schraml, S. Dankers, K. Bader, S. Will, and A. Leipertz, “Soot temperature measurements and implications for time-resolved laser-induced incandescence (TIRE-LII),” Combust. Flame **120**, 439–450 (2000).

[67] R.L. Vander Wal, T.M. Ticich, and A.B. Stephens, “Can soot primary particle size be determined using laser-induced incandescence ?,” Combust. Flame **116**, 291–296 (1999).

[68] M. Hofmann, *Laser-induced incandescence for soot diagnostics at high pressure*, PhD thesis, Heidelberg University, 2006.

[69] M.P.B. Musculus, S. Singh, and R.D. Reitz, “Gradient effects on two-color soot optical pyrometry in a heavy-duty DI Diesel engine,” Combust. Flame **153**, 216–227 (2008).

[70] C.J. Dasch, “One-dimensional tomography: A comparison of Abel, onion-peeling, and filtered backprojection methods,” Appl. Opt. **31**, 1146–52 (1992).

[71] E.O. Akesson, and K.J. Daun, “Parameter selection methods for axisymmetric flame tomography through Tikhonov regularization.,” Appl. Opt. **47**, 407–16 (2008).

[72] K.J. Daun, K.A. Thomson, F. Liu, and G.J. Smallwood, “Deconvolution of axisymmetric flame properties using Tikhonov regularization.,” Appl. Opt. **45**, 4638–46 (2006).

[73] B.M. Crosland, M.R. Johnson, and K.A. Thomson, “Analysis of uncertainties in instantaneous soot volume fraction measurements using two-dimensional, auto-compensating, laser-induced incandescence (2D-AC-LII),” Appl. Phys. B **102**, 173–183 (2011).

[74] B. Axelsson, R. Collin, and P.-E. Bengtsson, “Laser-induced incandescence for soot particle size and volume fraction measurements using on-line extinction calibration,” Appl. Phys. B **72**, 367–372 (2001).

[75] S. Skeen, J. Manin, K. Dalen, and L.M. Pickett, “Extinction-based imaging of soot processes over a range of Diesel operating conditions,” *in*: *8th U. S. National Combustion Meeting (Utah, 2013)*.

[76] J. Manin, S. Skeen, and L.M. Pickett, “Two-color diffused back-illumination imaging as a diagnostic for time-resolved soot measurements in reacting sprays,” SAE Int. J. Engines **6**, 1908–1921 (2013).

[77] M.P.B. Musculus, and K. Kattke, “Entrainment Waves in Diesel jets,” SAE Int. J. Engines **2**, 1170–1193 (2009).

[78] M. Sakai, H. Iguma, K. Kondo, and T. Aizawa, “Nanostructure analysis of primary soot particles directly sampled in Diesel spray flame via HR-TEM,” SAE Int. 2012–01–1722 (2012).

[79] T. Aizawa, H. Nishigai, K. Kondo, T. Yamaguchi, J.-G. Nerva, C. Genzale, S. Kook, and L.M. Pickett, “Transmission electron microscopy of soot particles directly sampled in Diesel spray

flame - A comparison between US#2 and biodiesel soot," SAE Int. J. Fuels Lubr. **5**, 665–673 (2012).

[80] K. Kondo, T. Yamaguchi, H. Nishigai, S. Takano, and T. Aizawa, "High-Resolution Transmission Electron Microscopy of Soot Directly Sampled at Different Axial Locations in Diesel Spray Flame," SAE Tech. Pap. 2011–24–0068 (2011).

[81] R.A.A. Dobbins, R.J. Santoro, and H.G. Semerjian, "Analysis of light scattering from soot using optical cross sections for aggregates," Symp. Combust. **23**, 1525–1532 (1990).

[82] B. Mewes, and J.M. Seitzman, "Soot volume fraction and particle size measurements with laser-induced incandescence," Appl. Opt. **36**, 709–717 (1997).

[83] H.A. Michelsen, P.O. Witze, D. Kayes, and S. Hochgreb, "Time-resolved laser-induced incandescence of soot: the influence of experimental factors and microphysical mechanisms," Appl. Opt. **42**, 557–5590 (2003).

[84] M. Thierley, H.-H. Grotheer, M. Aigner, Z. Yang, a. Abid, B. Zhao, and H. Wang, "On existence of nanoparticles below the sooting threshold," Proc. Combust. Inst. **31**, 639–647 (2007).

[85] J.P. Hessler, S. Seifert, and R.E. Winans, "Spatially resolved small-angle x-ray scattering studies of soot inception and growth," Proc. Combust. Inst. **29**, 2743–2748 (2002).

[86] B. Zhao, Z. Yang, M.V. Johnston, H. Wang, A.S. Wexler, M. Balthasar, and M. Kraft, "Measurement and numerical simulation of soot particle size distribution functions in a laminar premixed ethylene-oxygen-argon flame," Combust. Flame **133**, 173–188 (2003).

[87] R.W. Weeks, and W.W. Duley, "Aerosol-particle sizes from light emission during excitation by TEA CO2 laser pulses," J. Appl. Phys. **45**, 4661–4662 (1974).

[88] A.C. Eckbreth, "Effects of laser-modulated particulate incandescence on Raman scattering diagnostics," J. Appl. Phys. **48**, 4473–4479 (1977).

[89] H.A. Michelsen, "Understanding and predicting the temporal response of laser-induced incandescence from carbonaceous particles," J. Chem. Phys. **118**, 7012–7045 (2003).

[90] F. Liu, Smallwood, and D.R. Snelling, "Effects of primary particle diameter and aggregate size distribution on the temperature of soot particles heated by pulsed lasers," J. Quant. Spectrosc. Radiat. Transf. **93**, 301–312 (2005).

[91] F. Liu, M. Yang, F. a. Hill, D.R. Snelling, and G.J. Smallwood, "Influence of polydisperse distributions of both primary particle and aggregate size on soot temperature in low-fluence LII," Appl. Phys. B **83**, 383–395 (2006).

[92] B.F. Kock, C. Kayan, J. Knipping, H.R. Orthner, and P. Roth, "Comparison of LII and TEM sizing during synthesis of iron particle chains," Proc. Combust. Inst. **30**, 1689–1697 (2005).

[93] T.A. Sipkens, R. Mansmann, K.J. Daun, N. Petermann, J.T. Titantah, M. Karttunen, H. Wiggers, T. Dreier, and C. Schulz, “In situ nanoparticle size measurements of gas-borne silicon nanoparticles by time-resolved laser-induced incandescence,” Appl. Phys. B DOI: 10.1007/s00340–013–5745–2 (2014).

[94] R.L. Vander Wal, T.M. Ticich, and J.R. West, “Laser-induced incandescence applied to metal nanostructures.,” Appl. Opt. **38**, 5867–79 (1999).

[95] T. Yamaguchi, K. Kondo, H. Nishigai, S. Takano, and T. Aizawa, “Direct sampling, TEM analysis and optical measurement of soot particles at different axial locations in a transient spray flame,” SAE Int. J. Fuels Lubr. **5**, 316–328 (2012).

[96] D. Witkowski, K. Kondo, G. Vishwanathan, and D. Rothamer, “Evaluation of the sooting properties of real fuels and their commonly used surrogates in a laminar co-flow diffusion flame,” Combust. Flame **160**, 1129–1141 (2013).

[97] M. Hofmann, W.G. Bessler, C. Schulz, and H. Jander, “Laser-induced incandescence for soot diagnostics at high pressures,” Appl. Opt. **42**, 2052–2062 (2003).

[98] J. Johnsson, H. Bladh, and P.-E. Bengtsson, “On the influence of bimodal size distributions in particle sizing using laser-induced incandescence,” Appl. Phys. B **99**, 817–823 (2010).

[99] N.A. Fuchs, “On the stationary charge distribution on aerosol particles in a bipolar ionic atmosphere,” Geofis. Pura E Appl. **56**, 185–193 (1963).

[100] F. Liu, K.J. Daun, D.R. Snelling, and G.J. Smallwood, “Heat conduction from a spherical nano-particle: status of modeling heat conduction in laser-induced incandescence,” Appl. Phys. B **83**, 355–382 (2006).

[101] K. Kondo, T. Aizawa, S. Kook, and L.M. Pickett, “Uncertainty in sampling and TEM analysis of soot particles in Diesel spray flame,” SAE Tech. Pap. 2013–01–0908 (2013).

[102] R.J. Santoro, H.G. Semerjian, and R.A. Dobbins, “Soot particle measurements in diffusion flames,” Combust. Flame **51**, 203–218 (1983).

[103] R.J. Santoro, T.T. Yeh, J.J. Horvath, and H.G. Semerjian, “The transport and growth of soot particles in laminar diffusion flames,” Combust. Sci. Technol. **53**, 89–115 (1987).

[104] T. Ni, J.A. Pinson, S. Gupta, and R.J. Santoro, “Two-dimensional imaging of soot volume fraction by the use of laser-induced incandescence,” Appl. Opt. **34**, 7083–7091 (1995).

[105] B.B. Collier, and M.J. McShane, “Dynamic windowing algorithm for the fast and accurate determination of luminescence lifetimes,” Anal. Chem. **84**, 4725–31 (2012).

[106] A. Ehn, O. Johansson, A. Arvidsson, M. Aldén, and J. Bood, “Single-laser shot fluorescence lifetime imaging on the nanosecond timescale using a dual image and modeling evaluation algorithm,” Opt. Express **20**, 3043–56 (2012).

[107] R.J. Santoro, and J.H. Millers, “Soot particle formation in laminar diffusion flames,” Am. Chem. Soc. **3**, 244–254 (1987).

[108] B. Galmiche, *Development and exploitation of optical diagnostic techniques for soot particles measurements*, IFPEN Report, Rueil-Malmaison, 2010.

[109] R.A. Dobbins, and C.M. Megaridis, “Morphology of flame-generated soot as determined by Thermophoretic sampling,” Langmuir **3**, 254–259 (1987).

[110] S. Kook, and L.M. Pickett, “Soot volume fraction and morphology of conventional and surrogate jet fuel sprays at 1000-K and 6.7-MPa ambient conditions,” Proc. Combust. Inst. **33**, 2911–2918 (2011).

[111] Tedpella - TEM grid supplier, available at <https://www.tedpella.com/grids_html/grids.htm>.

[112] A.D. Abid, N. Heinz, E.D. Tolmachoff, D.J. Phares, C.S. Campbell, and H. Wang, “On evolution of particle size distribution functions of incipient soot in premixed ethylene–oxygen–argon flames,” Combust. Flame **154**, 775–788 (2008).

[113] J. Johnsson, H. Bladh, N.-E. Olofsson, and P.-E. Bengtsson, “Influence of soot aggregate structure on particle sizing using laser-induced incandescence: importance of bridging between primary particles,” Appl. Phys. B **112**, 321–332 (2013).

[114] K. Tian, K.A. Thomson, F. Liu, D.R. Snelling, G.J. Smallwood, and D. Wang, “Determination of the morphology of soot aggregates using the relative optical density method for the analysis of TEM images,” Combust. Flame **144**, 782–791 (2006).

[115] J.E. Dec, “Soot distribution in a DI Diesel engine using 2-D imaging of laser-induced incandescence, elastic scattering, and flame luminosity,” SAE Tech. Pap. 920115 (1992).

[116] J.E. Dec, and C. Espey, “Soot and fuel distributions in a DI Diesel engine via 2-D imaging,” SAE Tech. Pap. 922307 (1992).

[117] J.E. Dec, and C. Espey, “Ignition and early soot formation in a DI Diesel engine using multiple 2-D imaging diagnostics,” SAE Tech. Pap. 950456 (1995).

[118] J.E. Dec, “A conceptual model of DI Diesel combustion based on laser-sheet imaging,” SAE Tech. Pap. 970873 (1997).

[119] G. Bruneaux, “Combustion structure of free and wall impinging Diesel jets by simultaneous laser induced fluorescence of formaldehyde, poly-aromatic hydrocarbons, and hydroxides,” Int. J. Engine Res. **9**, 249–265 (2008).

[120] M. Bardi, R. Payri, L.M. Malbec, G. Bruneaux, L.M. Pickett, J. Manin, C. Genzale, and T. Bazyn, “Engine combustion network (ECN): comparison of spray development, vaporization and combustion in different combustion vessels,” Atom. Spray. **22**, 807–842 (2012).

[121] A.L. Kastengren, F.Z. Tilocco, C.F. Powell, J. Manin, L.M. Pickett, R. Payri, and T. Bazyn, "Engine combustion network (ECN): Measurements of nozzle geometry and hydraulic behavior," Atom. Spray. **22**, 1011–1052 (2012).

[122] L.M. Malbec, *Étude expérimentale des mécanismes d'entrainement d'air et de formation du mélange dans les jets Diesel, et impact sur la combustion et la formation des suies*, PhD thesis, Université d'Orléans, 2013.

[123] L.M. Malbec, J. Egúsquiza, G. Bruneaux, and M. Meijer, "Characterization of a set of ECN Spray A injectors: Nozzle to nozzle variations and effect on spray characteristics," SAE Int. J. Engines **6**, 1642–1660 (2013).

[124] L.M. Pickett, C.L. Genzale, J. Manin, L.M. Malbec, and L. Hermant, "Measurement uncertainty of liquid penetration in evaporating Diesel sprays," *in*: *ILASS Americas, 23rd Annual Conference on Liquid Atomization and Spray Systems (Ventura, 2011)*.

[125] M. Meijer, L.-M. Malbec, G. Bruneaux, and L.M.T. Somers, "Engine Combustion Network: 'Spray A' basic measurements and advanced diagnostics"," *in*: *12th International Conference on Liquid Atomization and Spray Systems, ICLASS 2012 (Heidelberg, 2012)*.

[126] J.E. Dec, and E.B. Coy, "OH radical imaging in a DI Diesel engine and the structure of the early diffusion flame," SAE Tech. Pap. 960831 (1996).

[127] B. Higgins, D.L. Siebers, and A. Aradi, "Diesel-Spray Ignition and Premixed-Burn Behavior," SAE Tech. Pap. 2000–01–0940 (2000).

[128] N. Peters, *Turbulent combustion*, (*Cambridge Univ. Press* (Cambridge, 2000)).

[129] D.L. Siebers, "Scaling liquid-phase fuel penetration in Diesel sprays based on mixing-limited vaporization," SAE Tech. Pap. 1999–01–0528 (1999).

[130] L.M. Pickett, J. Manin, C.L. Genzale, D. Siebers, M.P.B. Musculus, and C.A. Idicheria, "Relationship between Diesel fuel spray vapor penetration / dispersion and local fuel mixture fraction," SAE Int. 2011–01–0686 (2011).

[131] S. Bejaoui, X. Mercier, P. Desgroux, and E. Therssen, "Laser induced fluorescence spectroscopy of aromatic species produced in atmospheric sooting flames using UV and visible excitation wavelengths," Combust. Flame **161**, 2479–2491 (2014).

[132] G. Bruneaux, "A study of soot cloud structure In high pressure single hole common rail Diesel injection Using multi-layered laser-induced incandescence," *in*: *Comodia (Nagoya, 2001)*.

[133] B.F. Kock, B. Tribalet, C. Schulz, and P. Roth, "Two-color time-resolved LII applied to soot particle sizing in the cylinder of a Diesel engine," Combust. Flame **147**, 79–92 (2006).

[134] S. Maffi, S.D. Iuliis, F. Cignoli, and G. Zizak, “Investigation on thermal accommodation coefficient and soot absorption function with two-color TiRe-LII technique in rich premixed flames,” Appl. Phys. B **104**, 357–366 (2011).

[135] R. Ryser, T. Gerber, and T. Dreier, “Soot particle sizing during high-pressure Diesel spray combustion via time-resolved laser-induced incandescence,” Combust. Flame **156**, 120–129 (2009).

[136] H.A. Michelsen, “Laser-induced incandescence of flame-generated soot on a picosecond time scale,” Appl. Phys. B **83**, 443–448 (2006).

[137] S. Faust, G. Tea, T. Dreier, and C. Schulz, “Temperature, pressure, and bath gas composition dependence of fluorescence spectra and fluorescence lifetimes of toluene and naphthalene,” Appl. Phys. B **110**, 81–93 (2012).

[138] M.Y. Choi, and K.A. Jensen, “Calibration and correction of laser-induced incandescence for for soot volume fraction measurements,” Combust. Flame **112**, 485–491 (1998).

[139] G. Tea, G. Bruneaux, J.T. Kashdan, and C. Schulz, “Unburned gas temperature measurements in a surrogate Diesel jet via two-color toluene-LIF imaging,” Proc. Combust. Inst. **33**, 783–790 (2011).

[140] M. Bolla, Y.M. Wright, K. Boulouchos, G. Borghesi, and E. Mastorakos, “Soot formation modeling of n-Heptane sprays under Diesel engine conditions using the conditional moment closure approach,” Combust. Sci. Technol. **185**, 766–793 (2013).

[141] A. Bohlin, and C.J. Kliewer, “Communication: two-dimensional gas-phase coherent anti-Stokes Raman spectroscopy (2D-CARS): simultaneous planar imaging and multiplex spectroscopy in a single laser shot.,” J. Chem. Phys. **138**, 221101 (2013).

10 Acknowledgements

I would like to express my gratefulness and appreciation to Prof. Christof Schulz for his guidance in supervising the research, his invaluable help, and kindness. His knowledge, patience and understanding made possible the successful completion of the thesis. Christof, working with you has been a great fortune, thank you for broadening my horizons.

I would like to express my deepest and most affectionate gratitude and appreciation to Dr. Gilles Bruneaux, who has been my advisor and friend throughout my PhD studies. He inspired, encouraged and supported me for this research. His active participation at every stage of my study and mentoring have shaped my overall research outlook. I cherish the time I have spent under his guidance. Gilles, from the first day of this PhD, your guidance has been my greatest motivation. At every scientific challenge, you always pointed the solution. Beyond everything, you helped me enjoy this study so much that it became my favorite activity. Apart from the scientific work, you also helped me change my perspective towards life. I am very lucky to have a friend like you, thank you for everything.

I want to thank Dr. Thomas Dreier for his help and mentoring during the time I have spent in Duisburg. He has willingly shared his knowledge and ideas with me. I also want to thank Martin Leschowski who has shared his high-pressure burner experiment setup and time with me. I am truly thankful for his friendship and cooperation.

I am particularly grateful to Prof. Tetsuya Aizawa for his support to my research and for letting me have an incredible experience in Japan. Sensei Aizawa allowed me to use his lab for my research and helped me improve my knowledge in soot significantly. I also want to thank Katsufumi Kondo who has been a great friend and helped me enjoy Tokyo. Kats, I will always be watching for the next conferences to meet you.

Many thanks to the members of Optical Diagnostics Group at IFPEN, especially Gabrielle Tea, Dr. Hubert Baya Toda, Haifa Belaid, Dr. Louis-Marie Malbec, Lama Itani and Laurent Hermant, for their great support and friendship. I would also like to thank all my friends at IFPEN, University of Duisburg-Essen and Meiji University who have made these PhD years considerably more enjoyable. Special thanks to Clement Bramoulle from IFPEN for his unique friendship and assistance in the performed experiments. Without Clement, this work would not be completed on time. I especially wish to thank Elodie Toutain for the great support.

Finally, I would like to take this opportunity to thank my family for their constant love and self-sacrifice that kept me altogether throughout my education lifetime.